Mark Ebel

# Current-Phase Relationship of Nb/InAs(2DES)/Nb Josephson Junctions

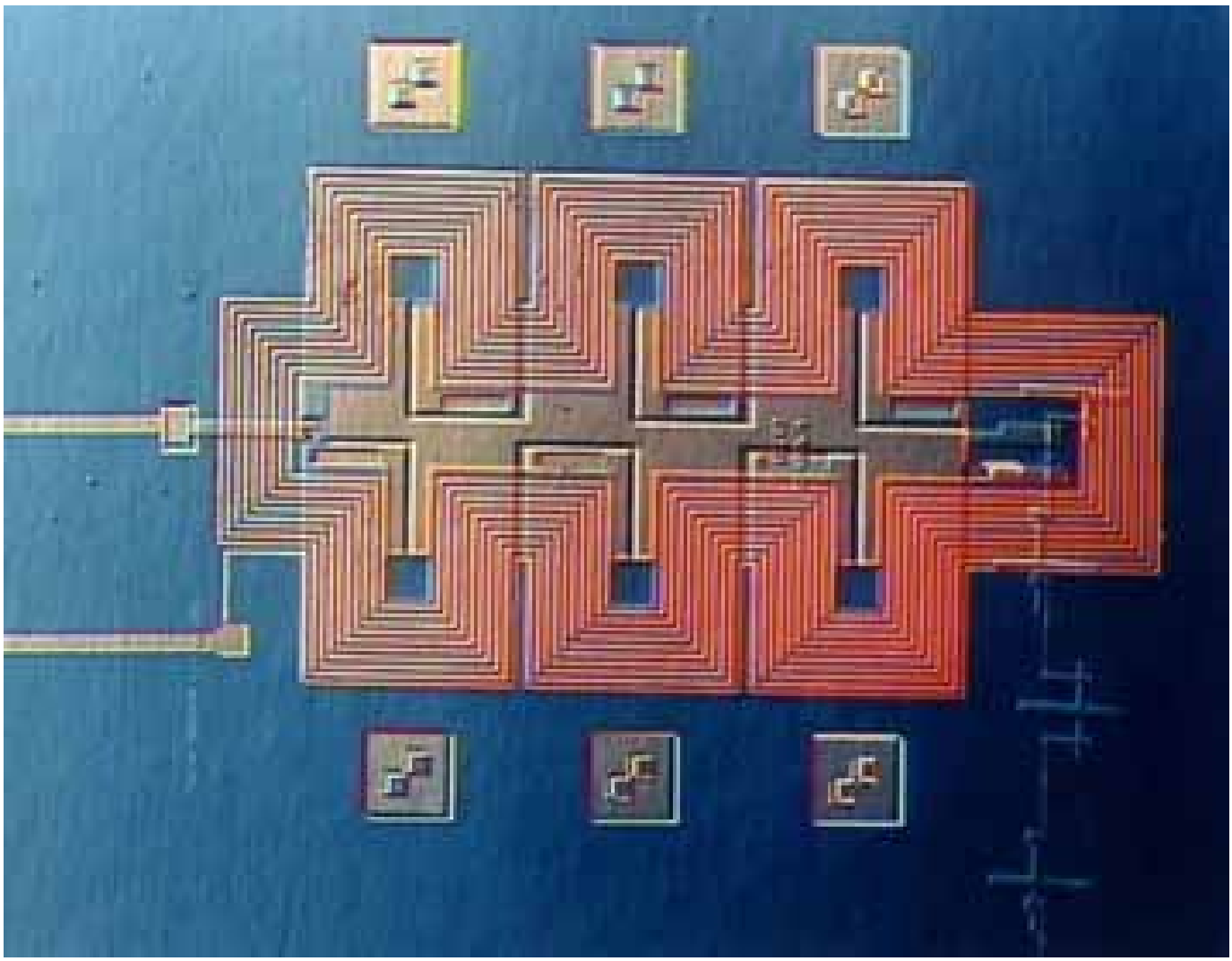

Cuvillier Verlag Göttingen

# Current-Phase Relationship of Nb/InAs(2DES)/Nb Josephson Junctions

Dissertation
zur Erlangung des Doktorgrades
des Fachbereichs Physik
der Universität Hamburg

vorgelegt von
**Mark Ebel**
aus Celle

Hamburg
2004

**Bibliografische Information Der Deutschen Bibliothek**
Die Deutsche Bibliothek verzeichnet diese Publikation in der Deutschen Nationalbibliografie; detaillierte bibliografische Daten sind im Internet über http://dnb.ddb.de abrufbar.
1. Aufl. - Göttingen : Cuvillier, 2004
Zugl.: Hamburg, Univ., Diss., 2004
ISBN 3-86537-253-8

| | |
|---|---|
| Gutachter der Dissertation: | Prof. Dr. Ulrich Merkt<br>Dr. Evgeni Il'ichev |
| Gutachter der Disputation: | Prof. Dr. Ulrich Merkt<br>Prof. Dr. Rainer Anton |
| Datum der Disputation: | 8. Oktober 2004 |
| Vorsitzender des Prüfungsauschusses: | Dr. Michael Martins |
| Vorsitzender des Promotionsausschusses: | Prof. Dr. Günter Huber |
| Dekan des Fachbereichs Physik: | Prof. Dr. Günter Huber |

⊕ CUVILLIER VERLAG, Göttingen 2004
Nonnenstieg 8, 37075 Göttingen
Telefon: 0551-54724-0
Telefax: 0551-54724-21
www.cuvillier.de


1. Auflage, 2004
Gedruckt auf säurefreiem Papier

ISBN 3-86537-253-8

## Abstract

This work reports on the preparation and measurement of microstructured superconductor/normal conductor/superconductor (SNS) Josephson junctions, using Nb as superconductor and the two-dimensional electron system (2DES) in either bulk InAs or in high-mobility InAs heterostructures as normal conductor. Two Josephson junction designs, namely overlap junctions and Josephson field-effect transistors (JoFET), are realized and optimized for mesoscopic applications. Transport measurements at low temperatures explore the electric properties of these systems. Their current-phase relationship (CPR) is investigated in dependence of temperature and gate voltage. The junctions are measured using a phase-sensitive inductive method by incorporating them into a superconducting loop, forming a single-junction interferometer that is coupled to a high quality tank circuit. The CPR is obtained by measuring the impedance of the phase-biased junction. At low temperatures and for highly transparent interfaces the CPR deviates substantially from the sinusoidal tunnel-junction behavior. This is the first time these deviations of the CPR have been observed in Nb/InAs(2DES)/Nb Josephson junctions. The measured CPR is in agreement with predictions of established theories for highly transparent SNS junctions. A scattering-matrix model is presented and used to fit the experimental data with good quantitative agreement.


## Inhaltsangabe


Diese Arbeit beschreibt die Herstellung und Messung von mikrostrukturierten Supraleiter/Normalleiter/Supraleiter Josephson-Kontakten mit Nb als Supraleiter und dem zweidimensionalen Elektronensystem eines InAs-Einkristalls oder einer InAs-Heterostruktur als Normalleiter. Zwei Josephson-Kontaktarten, Überlappkontakte und Josephson-Feldeffekttransistoren, werden hergestellt und für mesoskopische Anwendungen optimiert. Transportmessungen bei tiefen Temperaturen erkunden die elektronischen Eigenschaften dieser Systeme. Die Strom-Phasen-Beziehung (CPR) wird experimentell in Abhängigkeit von der Temperatur und der Gate-Spannung untersucht. Die Kontakte werden mit einer phasenempfindlcihem Methode gemessen, bei der die Kontakte in einen supraleitenden Ring eingebracht werden. Das so entstandene Einzelkontakt-Interferometer wird mit einem Schwingkreis hoher Güte gekoppelt. Man erlangt die CPR durch die Messung der Impedanz des Kontaktes bei festgelegter Phase. Bei tiefen Temperaturen und hochtransmissiven Grenzflächen weicht die CPR deutlich vom gewöhnlichen, sinusförmigen Tunnelkontaktverhalten ab. Dies ist der erste Nachweis derartiger Abweichungen in Nb/InAs(2DES)/Nb Josephson-Kontakten. Die gemessene CPR stimmt gut überein mit den Vorhersagen etablierter Modelle für hochtransmissive Kontakte. Ein Streumatrizenmodell wird vorgestellt und mit guter quantitativer Übereinstimmung an die gemessenen Daten angepasst.

# Contents

# 1. Introduction

Superconductivity, i.e. the complete disappearance of electrical resistance in various solids when cooled below a characteristic temperature $T_C$, was discovered by the Dutch physicist Kamerlingh Onnes (1911), who was awarded the Nobel prize in physics in 1913. A microscopic explanation became available with the BCS theory developed by Bardeen, Cooper, and Schrieffer (1957), earning them the Nobel prize in physics in 1972. Cooper discovered that electrons in superconductors are grouped in Cooper pairs, and that all of the Cooper pairs within a superconductor are correlated by a single macroscopic wave function. As a certain minimal amount of energy is needed to break up a Cooper pair, there is a gap $\Delta$ in the distribution of energy levels available to the electrons. $\Delta$ is temperature-dependent and vanishes at $T_C$.

Some of the most fascinating aspects of superconductivity are shown by Josephson junctions. Josephson (1962) predicted that a supercurrent could flow even between superconductors separated by a short area of non-superconducting material. He was shortly validated experimentally by Anderson and Rowell (1963) and was awarded the Nobel prize in physics in 1973. This Josephson current exhibits curious properties, for which many applications have been found since. The devices showing the effect are known as Josephson junctions. While Josephson initially focussed on tunneling junctions, where the superconductors are separated by an insulator, Josephson junctions exist for all small areas of weakened superconductivity between bulk superconductors, e.g. a constriction or a normal conducting layer. The family of Josephson junctions with finite normal conductivity is known as weak links, in contrast to tunneling junctions. Andreev (1964) proposed a microscopic model to explain the superconductivity in superconductor/normal conductor/superconductor (SNS) junctions, illustrated in Fig. 1.1, by a special Andreev reflection of quasiparticles[1] at the interfaces, in which Cooper pairs can cross the barrier in a coherent process. Competing with Andreev reflection are the familiar processes of normal reflection and quasiparticle transmission into the superconductor. The respective probabilities depend on energy and the interface properties and can be calculated using the Blonder, Tinkham, and Klapwijk (1982) (BTK) model. This model was extended into the OTBK model of Octavio, Tinkham, Blonder, and Klapwijk (1983) to deal with the complex phenomena in a SNS junction. However, as incoherent ballistic models, their range of applicability is restricted, as the quasi-classical assumptions are not satisfied in most junctions. Therefore these models, which are relatively easy to understand, are useful to explain the basic effects, but for

[1] When a Cooper pair breaks apart, the unpaired electrons are called quasiparticles.

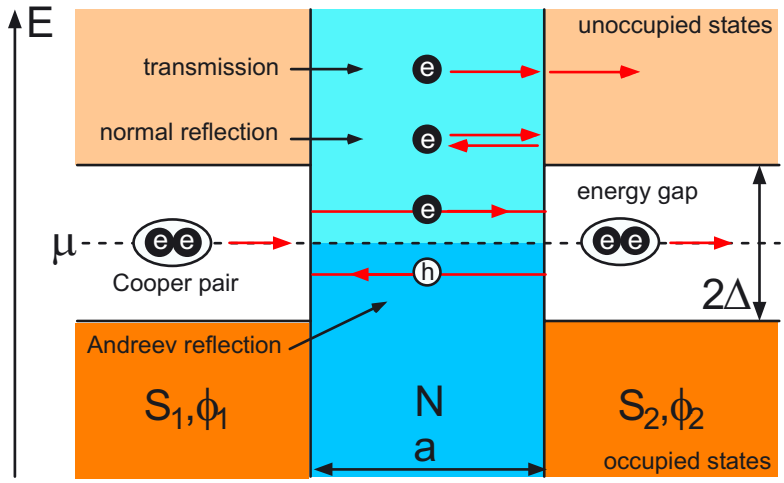


**Figure 1.1:** An electron $e$ approaching the NS interface cannot enter the superconductor S if its energy $E$ is less than the energy gap $\Delta$, because there are no available single-particle states. However, together with a matching electron from the Fermi sea, carrying opposite momentum and energy relative to the chemical potential $\mu$, a Cooper pair can be formed in a process called Andreev reflection. A hole $h$ remains, which traces the path of the incident electron and is reflected at the other SN interface as an electron, absorbing a Cooper pair in the process. Thus, a round trip provides a coherent mechanism for transporting Cooper pairs from one electrode to the other, forming an Andreev bound state. Interference of wave functions allows only certain numbers and positions of bound states, depending on the phase difference across the junction $\varphi = \Phi_1 - \Phi_2$ and the junction length. Also pictured are the alternative processes of transmission, if the electron energy is sufficient to reach an unoccupied state; and normal reflection, which occurs at imperfect interfaces.

the quantitative evaluation advanced mesoscopic scattering-matrix models should be used (see Bratus et al., 1995; Samuelsson et al., 2003, and references therein).

This work reports on highly transparent weak links, i.e. such with a high probability of Andreev reflection, in the Nb/InAs(2DES)/Nb system. These devices offer many exciting possibilities for basic research and applications. One example is a tunable superconductor/normal conductor/superconductor (SNS) Josephson junction, where the properties of the coupling two-dimensional electron system (2DES) can be influenced via a gate electrode. This device is known as Josephson field-effect transistor (JoFET), and was developed by Takayanagi and Kawakami (1985). It is also possible to construct a transistor by influencing the 2DES via current injection (Richter et al., 2002). The exact conduction mechanisms in these devices are still not fully understood. Although there are several theoretical models for certain aspects of junction behavior, none of them explains all aspects and is acknowledged universally.

For theoretical modeling of a Josephson junction, the dependency of the supercurrent $I_S$ flowing through it on the phase difference $\varphi$ across the junction is fundamental. $I_S(\varphi)$ is known as current-phase relationship (CPR). Josephson (1962) predicted a sinu-

soidal CPR $I_S(\varphi) = I_C \sin\varphi$ for tunnel junctions. SNS junctions with highly transparent interfaces are predicted to show significant deviations from a simple sinusoidal CPR at low temperatures. Direct experimental access to it could lead to further insights into the complex conduction mechanisms in these devices. Conversely, with a knowledge of the mechanism, evaluation of the CPR can yield information on the junction characteristics. Additionally, precise knowledge of the CPR is important for using these junctions as sensors or components in superconducting electronics. Standard methods in circuit design like the RCSJ[2] model (Stewart, 1968) implicitly assume a sinusoidal CPR, so these will either have to be modified or restricted in their range of validity for junctions with non-standard CPRs.

The continuing interest in superconductivity is exemplified in the awarding of the 2003 Nobel prize in physics to Ginzburg and Abrikosov for pioneering contributions to the theory of superconductors. Superconductors are slowly finding economic applications besides their use in research. The main advantages of devices made from superconductors are low power dissipation, high-speed operation, and high sensitivity. Because of their high costs of operation, they are initially introduced in areas where quality takes precedence over price, e.g. for medical, scientific or military applications. Current uses for superconducting materials include magnets, medical devices, power distribution equipment, magnetically levitated trains, motors, generators, transformers, computer parts, and the devices known as superconducting quantum interference devices (SQUID), which provide the most sensitive way of measuring magnetic fields, voltages, or currents. One exciting possible application of superconductivity is the field of quantum computing, where much research activity has been focussed in recent years. This rapidly developing field promises breakthroughs in computing power and could solve mathematical problems not accessible with conventional digital electronics. Although a commercially useful quantum computer is not expected in the next decades and is by no means certain at all, the interest of the international business press is exemplified by an article of the Economist (2001). The basic component of quantum computing is the quantum bit or qubit, a quantum mechanical system with two basic states. Many physical realizations of qubits have been proposed and built. Because of the inherent coherence of the macroscopic wave function in superconductors, they represent obvious candidates for solid state qubits. Research has focussed on two candidates, the flux and the charge qubit (see Makhlin et al. (2001) for a review). Although most projects up to now have used tunnel junctions, there is no fundamental reason against SNS weak links. The use of tunable junctions, e.g. JoFETs, in building qubits would allow fine-tuning of the devices after fabrication, thus eliminating the inevitable variance of device characteristics, which is feared to impede quantum computation in solid state devices (Keyes, 2002). Additionally, the application of JoFETs as switches for qubits has been proposed by Storcz and Wilhelm (2003).

[2] The resistively and capacitively shunted junction model offers an equivalent circuit to calculate Josephson device characteristics.

This work is organized as follows: Chapter 2 gives details on the design and fabrication of the Josephson junctions used in this project. Transport measurements of these devices, employed to determine their electrical properties, are presented in Chap. 3. The current-phase relationship is investigated in Chap. 4, before concluding in Chap. 5. Appendix A describes the Niobium sputter deposition system, the most important tool for the fabrication of the samples. The publications derived from this work are listed in Appendix B, detailed preparation parameters and a list of abbreviations are given in the Appendices C and D, respectively.

# 2. Design and Preparation of Nb/InAs(2DES)/Nb Josephson Junctions

The basic component of superconducting electronics is the Josephson junction. In our samples, two superconducting electrodes S are weakly coupled by a normal conducting layer N, defining a superconductor/normal conductor/superconductor (SNS) Josephson junction. The normal conducting layer is a two-dimensional electron system (2DES). Because of its direct (i.e. non-tunnel) conductivity, this type of junction is known as weak link as opposed to the much more common tunneling SIS junctions with insulating barriers I. We use two distinct junction designs on two substrates for a total of three junction types. Although they share some common properties, there are several important distinctions. At first, the different junction types and their working principles are introduced. Afterwards, their fabrication is described in detail.

## 2.1. Junction Types

Niobium (Nb) is the sole superconductor used in this project. As pure polycrystalline bulk metal, Nb becomes superconducting at $T_C = 9.25\,\mathrm{K}$ (Gmelin, 1969). This is the highest value of all elements. Nb is an attractive material for our purposes because of its relatively straightforward preparation and handling as thin film. By using Nb instead of alloys or ceramic high $T_C$ superconductors, we do not have to worry unduly about stoichiometry, crystal orientation or effects of unconventional superconductivity.

Figure 2.1(a) shows an overlap junction as developed by Chrestin and Merkt (1997). Two Nb electrodes on a substrate of p-type InAs single crystals are separated by an insulating oxide layer of some 10 nm thickness. Bulk p-type InAs is chosen for the naturally forming 2DES on its surface and its lack of a Schottky barrier (Mead and Spitzer, 1964), which facilitates contact to metals. The overlap layout is similar to a tunneling junction, but the thickness of the oxide barrier prevents significant tunneling, so all current flows through the 2DES. In the vicinity of the superconductors, the electronic properties of the 2DES in the inversion layer at the surface of the InAs are influenced by the proximity effect, resulting in an area of induced superconductivity (de Gennes, 1964; Chrestin et al., 1997). The main advantage of this design is the short channel length $a$ of $10-40\,\mathrm{nm}$, which can be controlled with nanometer precision. At a typical

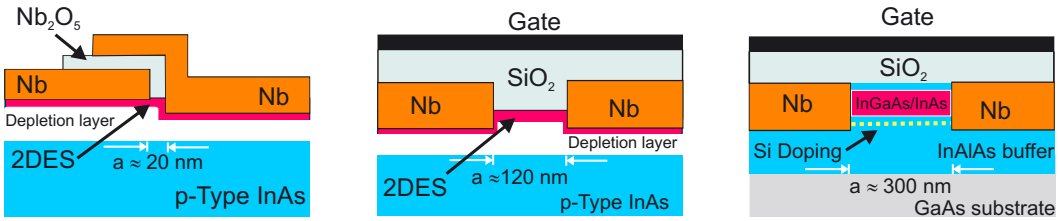


**Figure 2.1:** Schematic cross sections of SNS Josephson junctions: **(a)** overlap junction on bulk InAs, **(b)** JoFET on bulk InAs, **(c)** JoFET on a InAs HEMT heterostructure.

electron density of $n_S = 1.2 \cdot 10^{12}\,\mathrm{cm}^{-2}$ and mobility of $\mu \approx 10^4\,\mathrm{cm}^2/\mathrm{Vs}$, the mean free path of $l \approx 240\,\mathrm{nm}$ is much longer than the channel length. This limit $a \ll l$ is called ballistic. The mean free path is also longer than the coherence length $\xi_N \approx 100\,\mathrm{nm}$, approaching the clean limit $l \gg \xi_N$. The short limit $a \ll \xi_N$ is reached for the shortest channel lengths. These ratios are important for comparisons to theory, which is mostly concerned with the limiting cases.

The electrode separation of the Josephson field-effect transistor (JoFET) sketched in Fig. 2.1(b) is determined by lithography. The areas of the future electrodes are exposed, after development a narrow line of resist remains to separate the electrodes after Nb deposition and lift-off. Figure 2.2(a) shows an exemplary photograph of the electrodes after deposition, Fig. 2.2(b) a micrograph of the separated electrodes, Fig. 2.3(a) is a micrograph of the dividing resist line. The width of this line determines the electrode separation and thus the channel length $a$. With our present lithography process, there is a lower limit of about 100 nm for this channel length, so it is much longer than in overlap junctions and of comparable length to the coherence length $\xi_N$. This means the JoFET junction is not in the short limit and near, but not in, the ballistic limit. As the channel is not covered by an overlapping electrode, it is possible to control the carrier density and Fermi velocity of the 2DES by a gate electrode and to tune the junction from tunnel-like to high transparency behavior in this way.

A JoFET can be built not only on bulk InAs as substrate, but also on an customized semiconductor heterostructure known as high electron mobility transistor (HEMT). This alternative substrate offers optimized 2DES properties. Albrecht (2003) determined the electron density of $n_S = 6.9 \cdot 10^{11}\,\mathrm{cm}^{-2}$, mobility of $\mu \approx 134000\,\mathrm{cm}^2/\mathrm{Vs}$, and coherence length $\xi_N \approx 290\,\mathrm{nm}$ in the wafer 1147 used in this work. The resulting mean free path of the carriers is an order of magnitude larger than on bulk substrates and much longer than the coherence length. Thus these junctions are definitely in the clean limit $l \gg \xi_N$, whereas in the bulk junctions the two values are still of comparable magnitude. In HEMTs the 2DES is confined to a thin horizontal layer below the surface of the heterostructure (Fig. 2.4). Further lateral confinement (e.g. to avoid bypass currents or to insulate certain parts of the sample electrically) is possible by removing unwanted areas of this layer by dry etching.

## 2.2. Sample Preparation

The sample preparation will be introduced by means of the simplest case of a JoFET on bulk InAs as example, and subsequently describing the differences for HEMT substrates and for overlap junctions. Details of the parameters and equipment used can be found in Appendix C.

### 2.2.1. Josephson Field-Effect Transistors on Bulk InAs

A commercial p-type InAs wafer[1], doped with Zn in the nominal concentration of $n_D = 8 \times 10^{16}$ cm$^{-3}$, is divided into $5 \times 6$ mm$^2$ chips. These are polished mechanically and chemically in order to remove a possibly contaminated layer, yielding a clean surface with a roughness[2] of about 1 nm. The samples are spin-coated with about 800 nm PMMA[3] as standard resist for electron-beam lithography and baked at 160°C. The fine structures requiring the highest precision are exposed in a scanning electron microscope (SEM) with an integrated writing unit. Exposure parameters are determined by testing dose arrays. The SEM exhibits some drift, so the parameters either need to be verified immediately before exposure, or several structures with slightly varied parameters are written on the sample and the best one is selected afterwards for further processing. After developing the resist, the samples are inspected using a phase-contrast optical microscope. Satisfactory samples are mounted on a copper plate and transferred via load lock into a custom-built Nb magnetron sputter deposition system. At the beginning of the three-step deposition process, the Nb target is etched by moderate-power direct-current (dc) magnetron sputtering to expose a fresh, uncontaminated surface. The ejected Nb atoms coat the surfaces of the sputter chamber and improve the process atmosphere by gettering unwanted reactive residual gases such as oxygen. The sample is protected by a baffle system. In the second step, the sample is uncovered and its areas not covered by the resist are cleaned using low-power radio-frequency (rf) plasma etching to remove oxidized material and other possible contaminants and so to assure clean interfaces and good adhesion. This preparation step is critical for the junction transparency, because contaminants as well as damage to the crystal degrade the interface and the 2DES. The challenge is to remove the surface layer without increasing the interface roughness or introducing other problems. The best results have been achieved with 8 min of low-energy rf plasma (5 W, 180 V) at 1.0 Pa[4] Ar pressure, etching about 30 nm. It is also possible to prolong this step to achieve arbitrary etch depths. Without any delay, a dc plasma is started at 150 W and 280 V to etch the previously cleaned Nb target. The Nb ejected by this process coats the sample with a Nb film of desired thickness (a typical duration of 150 s yields a 100 nm film). These three steps are performed in sequence

[1] supplied by Crystec, Berlin
[2] measured with an atomic force microscope (AFM) evaluating the roughness over a 10x10 µm$^2$ area
[3] polymethylmethacrylate
[4] 1 Pa corresponds to 0.01 mbar

without moving the sample or changing the process gas. Further details of the system and the influences of the sputtering process on junction quality are given in Ebel (2000) and in Appendix A.

To remove the surplus Nb deposited on top of the resist-covered parts of the substrate, the samples are put into a bath of remover solvent and soaked overnight. The actual lift-off, i.e. the removal of the surplus metal, is done either by spraying a jet of hot acetone on the sample immediately after removing it from the remover solvent, or by putting it into an ultrasonic bath. The latter method is more thorough, but needs to be applied cautiously, as bulk InAs is very brittle and shatters easily. It is crucial to remove all the metal from the narrow channel between the electrodes by the lift-off to avoid a short-circuit[5]. Most of the time, such shorts can be detected via optical microscopy. The afflicted sample is discarded. The established way to facilitate lift-off is to use undercut edge profiles in the resist, realized either by optimized resists or multi-resist layer structures. Unfortunately, this is hardly applicable for the long, narrow resist lines required to separate our electrodes, as the typical undercut of several hundred nm exceeds the line width. A little undercut is possible even using PMMA by optimizing the exposure parameters, as documented by Kürsten (see Fig. 2.3(a)), but an excessive undercut can destroy the structure, because the separating resist line will detach (Fig. 2.3(b)). We tried to improve the lift-off by using different removers or pure acetone, a remover with an added relaxant, by varying the soak times or by heating the remover. No significant and reproducible improvements have been found over the established process of a 12 h bath in Allresist remover AR300-70. A reduced thickness of the Nb film eases the lift-off, but as the thickness is usually determined by the junction design we cannot consider it a free parameter. Decreasing the thickness of the resist by spinning at 6000 rpm considerably worsens the lift-off, while the required lithography precision excludes increased resist thicknesses. After lift-off, the electrode separation is measured by SEM[6](Fig. 2.2(b)) or atomic force microscope (AFM), where it is also possible to verify the junction geometry and to detect microshorts not visible optically.

Only the structures requiring the highest precision are written by electron-beam lithography, while other parts are processed by optical lithography. Again, the sample is cleaned, resist is spun on and baked, the areas of the samples to be covered with Nb are exposed, the sample is developed, Nb is deposited and lifted off. Here, the lift-off is not as delicate as the structures are large.

At this point, the actual SNS junction is complete. A JoFET additionally needs a gate electrode. As it has to be insulated from the junction, the sample is covered with 300 nm $SiO_2$ in a plasma-enhanced chemical-vapor deposition system (PECVD). For our combination of materials and equipment, thinner oxides cannot guarantee insulation

[5] A microshort can constitute a constriction-type ScS Josephson junction, which is interesting to compare to SNS junctions. A measurement of such a ScS junction was performed by Baars (2004).

[6] There are sporadic reports of damage to the 2DES by the high-energy electrons of the SEM beam. We have found no evidence of any impairment by the SEM in our junctions.

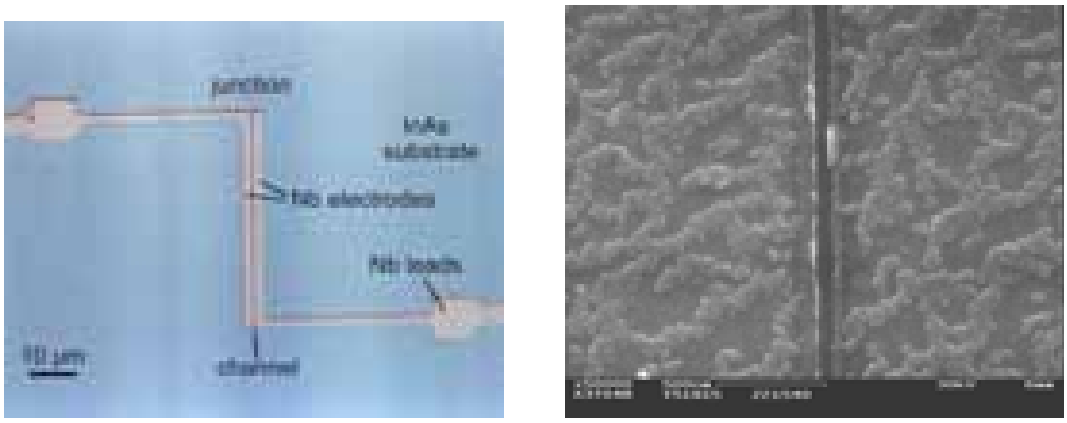


(a) (b)

**Figure 2.2:** **(a)** Two separated Nb electrodes (vertical) for a JoFET on bulk InAs. The electrodes are 50 µm long and 2 µm wide. Also visible are the leads (horizontal) for transport measurements. **(b)** SEM micrograph of the channel between JoFET electrodes. The electrode separation in this picture is 90 nm and is constant along the channel.

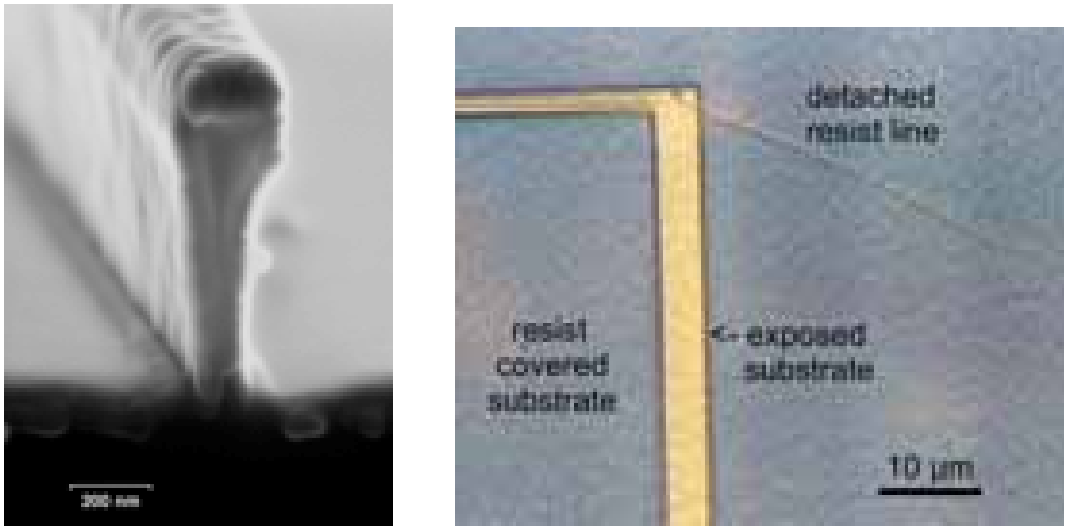


(a) (b)

**Figure 2.3:** **(a)** Micrograph of a 200 nm wide PMMA resist line designed to separate Nb electrodes in a JoFET. Its width decreases closer to the InAs substrate, this undercut facilitates the lift-off of the Nb film to be deposited. Taken from Kürsten (2002). **(b)** Too much undercut can detach a resist line as in this picture of exposed and developed PMMA resist. This picture corresponds to the upper central part of Fig. 2.2(a).

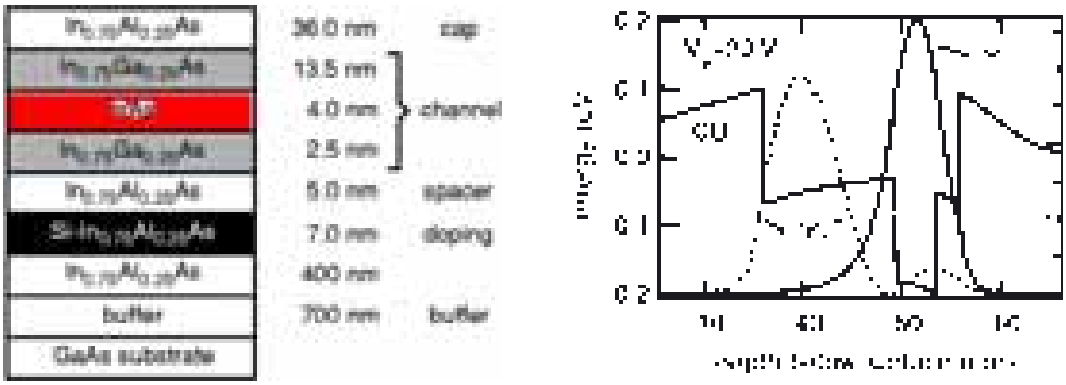


(a) (b)

**Figure 2.4:** **(a)** Layer sequence of the HEMT heterostructure used in this work. The conducting 2DES forms in the channel. **(b)** Conduction band CB and probability densities $|\Psi|^2$ for the first two subbands at a gate voltage of $V_G = 20$ V. Taken from Richter (2001).

of the gate electrode, as shown by Kürsten (2002). This is a consequence of the relatively low deposition temperatures (150°C) necessitated by the InAs substrate, which decomposes at much higher temperatures. The PECVD-deposited oxide shows better insulating properties if grown at higher substrate temperatures (Meißner, 1998). HEMT substrates are stable at higher temperatures, but here problems by oxidizing at temperatures above 200°C were reported by Albrecht (2003). Different thermal expansions between Nb and the substrate are the suspected causes.

To contact the Nb layer underneath the oxide, the Nb contact pads are uncovered by wet chemical etching in hydrofluoric acid HF. In the last preparation step, the area of the gate electrode is defined by optical lithography. In a thermal evaporator 10 nm Al as adhesion enhancer and 40 nm Au to prevent corrosion are deposited as gate electrode.

### 2.2.2. Josephson Field-Effect Transistors on HEMT Heterostructure Substrates

The InAs HEMT heterostructures in this work were fabricated by molecular-beam epitaxy in the group of Wolfgang Hansen at our institute. Details of their properties are given in Richter (2001). The 2DES in the HEMT used is confined in a narrow layer 50 nm below the surface (Fig. 2.4). The basic preparation process delineated in the previous section can be employed on HEMT substrates with two modifications: first, there is no need for polishing, as the quality of the 2DES is not determined by the surface properties, but by the molecular-beam epitaxy process. Secondly, we have to assure that the electrodes reach the 2DES buried in the structure. To do this, one could remove the insulating cap layers on top of the 2DES by selective etching (if chemically suitable), deposit metal and achieve planar contact. This is the established method, utilized by

Takayanagi et al. (1995) in the first realization of a JoFET on a HEMT substrate and still used by most other groups[7]. We use an alternative approach, dry etching unselectively into the heterostructure perpendicular to the surface for a sufficient depth, thereby cutting through the 2DES, and later contacting its sides with deposited metal. Because of the low thickness of the 2DES ($\approx 4\,\mathrm{nm}$), the superconductor is in contact with the 2DES only at a small area, in contrast to the planar contact of the junctions on bulk InAs with the 2DES everywhere underneath the electrodes. This has the advantage of a clearly defined junction length, as no parts besides the front of the electrodes are in contact with the 2DES, but makes for a difficult contact. Selective etching, as necessary for the first approach, is not available for our HEMTs because of their chemical composition.

The dry etching can be done either in situ by extending the rf plasma etching step in the Nb sputter deposition system or ex situ in an dedicated reactive ion etching (RIE) system using gaseous $SiCl_4$ as etchant (even in this case we use a short (4 min) rf etch step in the sputter chamber to clean the surface of any contaminations immediately before Nb deposition). Both methods etch anisotropically, yielding the desired perpendicular edge profiles. An important distinction is what happens to the substrate atoms once they leave the substrate. In a RIE process, they react with the etchant to form gaseous molecules and are carried away, leaving behind a clean surface. In contrast, a sputter system works by accelerating Ar ions towards the target surface, which eject target matter on impact. This is a mechanical process, so no chemical reactions occur. Thus the ejected debris could possibly redeposit on the side walls not subjected to the directed etching, thus contaminating the channel and harming interface transparency. To minimize this effect, the etching should stop as soon as the channel is reached. In practice, it is difficult to adjust the etching with the desired accuracy. Also, if the etching stops before the active layer has been cut completely, there is uncontrolled planar contact between channel and electrodes. AFM measurements of test samples were used to determine the etching rates and to investigate the surface structure of etched areas. No significant difference in surface roughnesses between areas etched by the two techniques and the unmodified substrate were found. Both etching methods have been used to fabricate JoFETs on HEMTs, with the RIE process yielding the better results. A detailed evaluation of the resulting device properties is given in Chap. 3.3.

The lift-off process required to define the Nb electrodes is even more demanding on HEMT substrates than on bulk InAs. The adhesion between the deposited Nb and the substrate surface is weaker than on bulk samples, so parts of the electrodes can break away from the sample (see Fig. 2.5 for some examples). In contrast, the Nb between the electrodes is much harder to remove. This contradicts naïve expectations, as both the larger electrode separation possible on HEMTs and the bigger differences in heights (due to the etching process) should ease lift-off. It is not clear what is responsible for these difficulties. The different attempts to improve lift-off mentioned in Chap. 2.2.1

[7] see e.g. Bagwell (1999); Bastian et al. (1998); Heida et al. (1999); Schäpers et al. (1997)

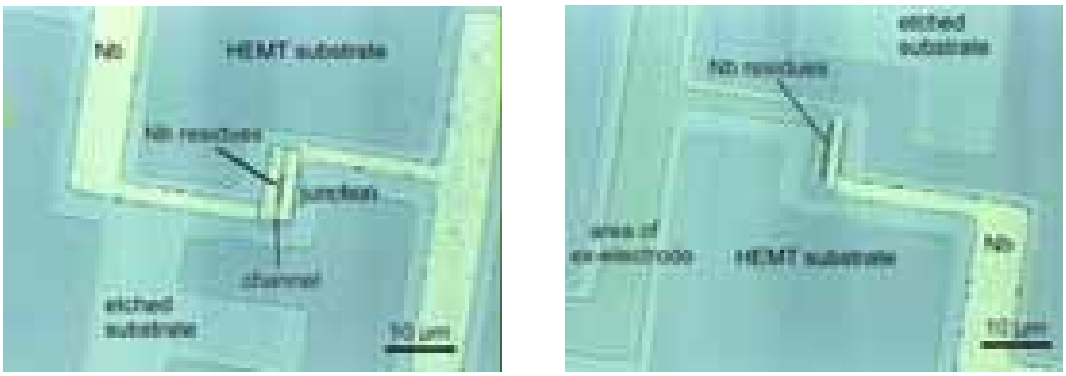


(a) (b)

**Figure 2.5:** Typical lift-off problems on HEMT JoFET samples: **(a)** Some Nb remains between the electrodes. **(b)** Nb is sticking in the channel, even after one electrode detached from the substrate after ultrasonic treatment.

have been tried on HEMTs as well as on bulk crystals. Less deep etching improves the success chances, but a certain etch depth is required to reach the 2DES in HEMTs. The problematic lift-off is the main cause for the low yield of working HEMT samples.

### 2.2.3. Overlap Junctions on Bulk InAs

Whereas in JoFET structures both electrodes are deposited at the same time, in overlapping structures at first only one is deposited. The junction area is insulated by dipping the sample into an oxidizing electrolyte, creating a homogenous layer of insulating $Nb_2O_5$ covering the electrode. The oxide thickness (and thus the electrode separation *a*) can be set with nanometer precision by controlling the voltage during the anodic oxidation (Scharnweber, 1993). Areas not to be oxidized are protected by resist. Unprotected InAs gets oxidized as well. We remove this unwanted byproduct by selective chemical etching in sulphuric acid $H_2SO_4$. Subsequently, the second electrode is patterned and deposited overlapping only the oxide-covered parts of the first one (Fig. 2.6). Overlap junctions are not fitted with a gate.


(a) (b)

**Figure 2.6:** **(a)** Optical micrograph of an overlap junction. The oxide-covered part of the Nb electrode is marked by its dark color. The step in the substrate is the edge of the trough created by removing oxidized InAs. **(b)** Close-up of the junction area.

# 3. Transport Measurements of Nb/InAs(2DES)/Nb Josephson Junctions

The samples are constantly monitored during the preparation using optical microscopy and, if necessary, SEM and AFM. But the decisive characterizations of their electrical properties are done by transport measurements at low temperatures.

## 3.1. Measurement Procedures

Standard measurements are performed in four-point geometry (Fig. 3.2(a)), using two voltage and two current probes to avoid complications by contact voltages. In case of JoFETs, there is an additional electrode to the gate. The sample is mounted on a chip carrier, Al wires are connected to the contact pads either by wedge bonding or by soldering with In lot. The sample is installed into a custom built sample stick (see Adolph, 1998, for a description) that intermediates between sample and electronics and insulates the sample against stray electromagnetic fields. The assembly is lowered into a pumped liquid He cryostat (minimum temperature $T = 1.5$ K). A dedicated computer program starts the measurement, takes control of all parameters and records the data.

All measurements are done with current biasing, i.e. by driving a current through the junction and measuring the voltage. Most theories are based on voltage bias, which can complicate comparisons. During cool-down, we monitor the temperature-dependent resistance $R(T)$ by biassing the sample with a small ac modulation current $I_{\mathrm{mod}}$ of typically 0.5 µA and 300 Hz frequency, but no dc current, and measure the ac voltage $V_{\mathrm{ac}}$ and phase angle by Stanford Research SR830 lock-in amplifiers. The $R(T)$ measurement serves to determine the critical temperature of the electrodes and the 2DES. When the sample has reached a stable low temperature, the direct and differential $I$-$V$-curves are recorded. The junction is biased with a minimal modulation current $I_{\mathrm{mod}}$ and a slowly ramping quasi-dc current $I$, whose amplitude is chosen to result in a maximum voltage drop of 5 mV (to exceed the energy gap $2\Delta/e$) across the junction. The dc voltage over the junction is measured with Keithley 2000 multimeters, the ac components by lock-in amplifiers. We use the dc voltage-current characteristic $V(I)$ to determine the critical current $I_C$, return current $I_{\mathrm{return}}$, excess current $I_{\mathrm{Ex}}$, and normal resistance $R_N$ as exemplified in Fig. 3.2(b). Note that because of the conducting substrate we do not measure

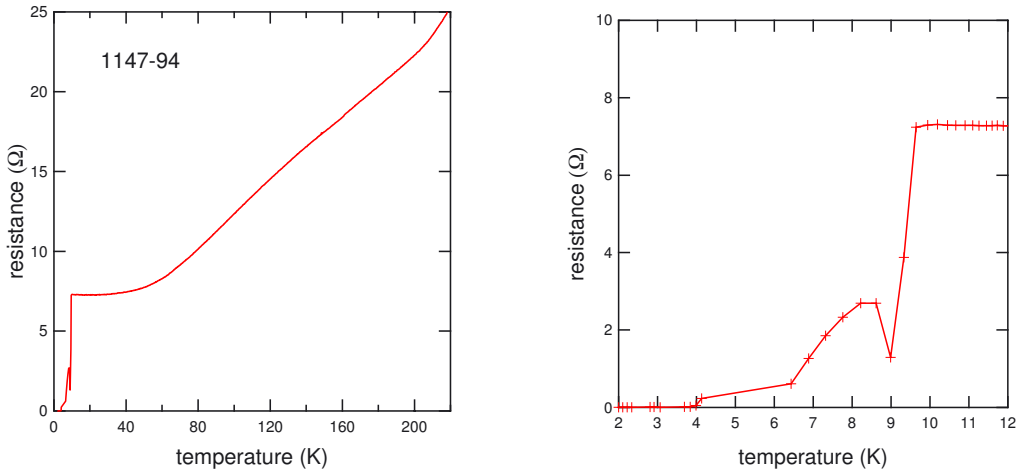


**Figure 3.1:** **(a)** Exemplary temperature-dependant resistance measurement $R(T)$ of RIE etched HEMT JoFET 1147-94. **(b)** Close-up of the transition range. The Nb electrodes become superconducting at 9 K, but the resistance of the junction remains finite down to 4 K.

pure junction characteristics, but a parallel connection of the junction and the 2DES surrounding it. This effect manifests itself most significantly in a normal resistance $R_N$ measured systematically too low, especially if the junction resistance is comparable to the substrate resistance. The product of critical current and normal resistance $I_C R_N$ is known as characteristic voltage and is a standard measure of junction quality. An ideal ballistic junction at zero temperature would have $I_C R_N = \pi\Delta/e \approx 4.5\,\mathrm{meV}$ (for Nb) according to Kulik and Omel'yanchuk (1977). Similarly, $I_{\mathrm{Ex}} R_N$ is an indicator of junction transparency, according to the OTBK model.

The junction transparency can be evaluated by comparing the normal resistance $R_N$ with the Sharvin (1963) resistance

$$R_{\mathrm{Sh}} = \frac{h}{2e^2}\frac{\lambda_F}{2w} = \frac{R_0}{N} \quad \text{with} \quad \lambda_F = \sqrt{\frac{2\pi}{n_S}}, \tag{3.1}$$

with junction width $w$, elementary charge $e$, Planck's constant $h$, and Fermi wavelength $\lambda_F$. The Sharvin resistance depends only on geometry and carrier density $n_S$. It originates in mesoscopic physics, where $R_0 = h/e^2$ is known as resistance quantum and $N = 2w/\lambda_F$ is the number of transmission channels. $R_{\mathrm{Sh}}$ is the resistance of an ideal ballistic junction, thus it constitutes a lower barrier for the normal resistance, and can serve to define the junction transparency (through both interfaces) $D = R_{\mathrm{Sh}}/R_N$.

We measure the differential resistance $dR = dV/dI$ to investigate a series of dips and peaks known as the subharmonic gap structure and the resistance drop from $R_N$ to $R_{\mathrm{min}}$, as depicted in Fig. 3.3. These effects depend on details of the Andreev reflection

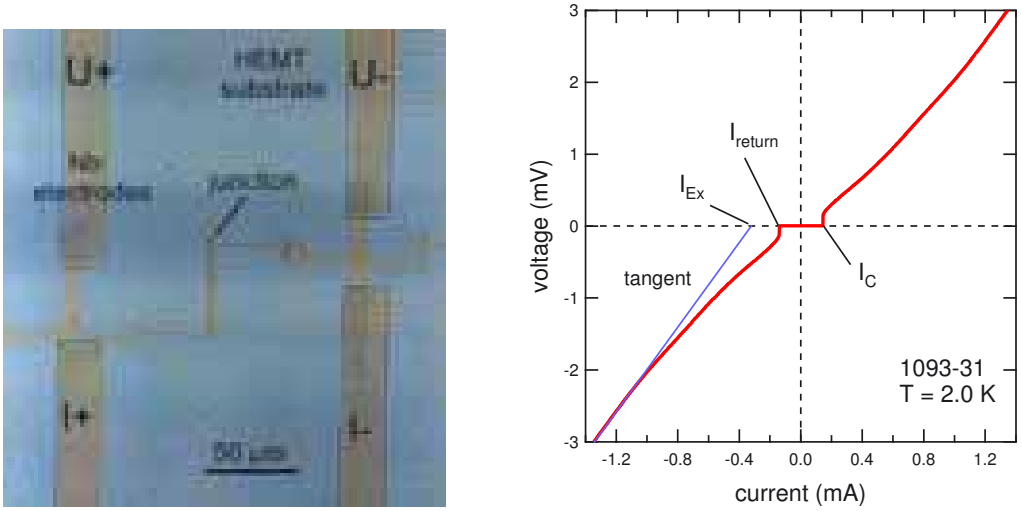


(a) (b)

**Figure 3.2:** **(a)** Four-point-probe configuration, exemplified by HEMT junction 1147-6 with Nb transport electrodes. **(b)** Exemplary dc voltage-current characteristic $V(I)$ of the overlap junction 1093-31 with $w = 20\,\mu\text{m}$ and $a = 30\,\text{nm}$. The current is ramped from high negative to high positive values. The value designated as return current $I_{\text{return}}$ is reached when the voltage drop across the junction vanishes for decreasing negative currents. The value where a voltage drop first occurs for rising currents is designated as critical current $I_C$. The junction is hysteretic if $I_C > I_{\text{return}}$. For high voltages $V \gg \Delta/e$ (to avoid an influence of the subharmonic gap structure), the $V(I)$-curve is linear, with the normal resistance $R_N$ as gradient. If a tangent to the curve in this part is extrapolated, it crosses the zero voltage line (dashed) at a finite value, designated as excess current $I_{\text{Ex}} = I(V \gg \Delta/e) - V/R_N$. This current is a consequence of Andreev reflections, as one quasiparticle can result in transport of more than one charge across the junction. Thus $I_{\text{Ex}}$ can be interpreted as an indicator of interface transparency using the OTBK model.

probability, and so are potentially helpful to find out more about it and the junction transparency. Blonder, Tinkham, and Klapwijk (1982) explained the subharmonic gap structure as a consequence of multiple Andreev reflections (exemplified in Fig. 1.1) in the presence of a voltage between the electrodes. A multiple Andreev reflection process in which a quasiparticle crosses the junction $n$ times becomes possible at voltages of $eV = 2\Delta/n$, thus leading to current anomalies at this voltages. These manifest themselves as dips and peaks in the differential resistance, i.e. the subharmonic gap structure. The basic BTK model was expanded to the OTBK theory (Octavio et al., 1983; Flensberg et al., 1988) and adapted to our junction geometry by Aminov et al. (1996) and Chrestin et al. (1997). It should be noted that OTBK and its derivatives are incoherent and ballistic models, whereas in our junctions coherent effects are pronounced despite some scattering in the 2DES. Nevertheless, the OTBK theory can be used as a

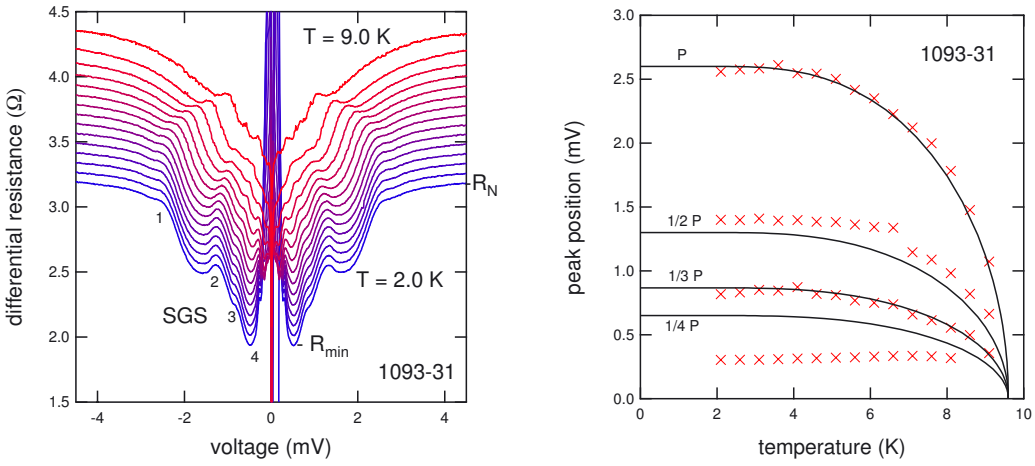


(a) (b)

**Figure 3.3:** **(a)** Differential resistance $dR = dV/dI$ of the overlap junction 1093-31. Besides a smooth decrease of the differential resistance from $R_N$ to $R_{\min}$ for low voltages, a series of dips and peaks known as the subharmonic gap structure is visible for voltages at $2\Delta_N/ne$. Marked are the first four peaks of the structure, the normal resistance $R_N$, and the minimal resistance $R_{\min}$. The spikes near zero voltage are artifacts of the transition into the zero-resistance state. **(b)** Positions of the first four peaks in the subharmonic gap structure in dependence on temperature. Peak positions shift proportional to the induced energy gap $\Delta_N$, as predicted by BCS theory. Drawn as solid lines are the predictions for the first four peak positions $2\Delta_N(T)/ne$ according to the OTBK model. Fitting the position of the first peak delivers $\Delta_N(0) = 2.6\,\text{meV}$ and $T_C = 9.4\,\text{K}$.

first guide. Advanced mesoscopic models (see Samuelsson et al., 2003, and references therein) are also available to calculate the subharmonic gap structure. Unfortunately, the calculations do not match our experimental data too well, as our junctions do not confirm exactly to the requirements of the models.

Quantitative evaluation of the subharmonic gap structure is used to determine the induced energy gap $\Delta_N$, as the subharmonic gap features are predicted to occur as a series at positions $eV = 2\Delta_N/n$ (with n as integer), thus allowing us to deduce $\Delta_N$ from the measurement of the differential resistance. As $\Delta_N$ is a function of temperature and vanishes for $T_C$, the evaluation of the temperature-dependence of the subharmonic gap structure as in Fig. 3.3(b) is also a very sensitive way to determine the critical temperature, whereas in dc measurements is is hard to assess exactly at which temperature the superconductivity vanishes (see the inset of Fig. 3.7 for an example). Unfortunately, it is often difficult to identify the exact positions of subharmonic gap features, especially at higher temperatures, as they are not clearly distinguished from the background. Additionally, there are numerous other interference effects causing sub-gap structures besides multiple Andreev reflections (Bastian et al., 1998). Some, e.g. the

Fiske (1964) resonances, can be distinguished from subharmonic gap structures by their temperature-independent positions.

In HEMTs, the carrier density in the 2DES can be increased significantly by the persistent photo effect. We illuminate the sample with a light-emitting diode (LED), as the channel can be depopulated. The effects of illumination are junction specific and can vary drastically even for junctions from the same wafer, as exemplified in Fig. 3.4. If the channel is not depleted at the beginning of the measurements, an enhanced carrier density does not significantly increase the junction quality (as measured by the $I_C R_N$ product, Fig. 3.4(b)). The increased carrier density declines exponentially with a half life of several hours, therefore longer measurements are performed under constant illumination.

All standard transport measurements are performed for varying temperatures $T$ and, in case of JoFETs, for several gate voltages $V_G$. Besides these routine applied to nearly every sample prepared, there are nonstandard measurements such as the magnetic field dependency $I_C(B)$ (see Fig. 3.12 for an example) to evaluate the spatial distribution of the current. For a current density homogeneous over the width of the junction, the $I_C(B)$ graph is a Fraunhofer pattern:

$$I_C(\Phi) = I_C(0) \left| \frac{\sin(\pi\Phi/\Phi_0)}{\pi\Phi/\Phi_0} \right|, \tag{3.2}$$

where $\Phi$ is the magnetic flux through the junction and $\Phi_0$ is the flux quantum. In practice, as flux is difficult to measure and the applied magnetic field $B$ is proportional to $\Phi$, the positions of the minima in the $I_C(B)$-curve are used to calibrate $B$ to $\Phi/\Phi_0$. Inhomogeneous current distributions, e.g. caused by imperfect interfaces or varying junction lengths, result in deviations from the regular pattern. While it is not possible to directly deduce the distribution from the measurement, patterns of assumed model distributions can be calculated and compared to the experiment.

## 3.2. Miniaturization of Nb/InAs(2DES)/Nb Josephson Junctions

There is considerable experience at our institute in fabricating high quality Josephson junctions in overlapping (Chrestin, 1996) or JoFET geometry (Kürsten, 2002). However, as these samples were optimized for transport measurements, they exhibit large critical currents. In this work, junctions with reduced critical current for CPR measurements and other mesoscopic applications are produced by reducing the junction width, while maintaining high quality.

Sample 1093-J5 is a bulk JoFET of $w = 1.0\,\mu\text{m}$ width and $a = 170\,\text{nm}$ electrode separation. It was prepared from the same wafer and in the same batch as sample 1093-J9 presented later in Chap. 4.4.2 to serve as comparison sample for transport

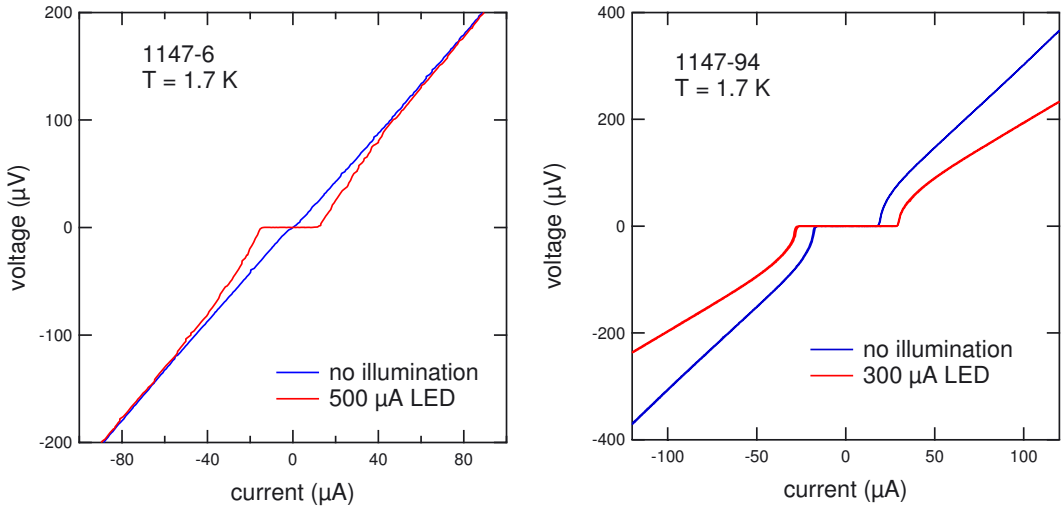


**Figure 3.4:** **(a)** The rf etched HEMT junction 1147-6 has a critical current of only $I_C = 0.5\,\mu A$ after cooling down, but subsequent illumination with a LED increases $I_C$ to $13\,\mu A$. The normal resistance (the gradient of the curve) remains constant at $R_N = 2.3\,\Omega$, yielding a $I_C R_N$ product of $32\,\mu V$. **(b)** In RIE etched HEMT JoFET 1147-94, illumination increased $I_C$ from 16 to $28\,\mu A$, while $R_N$ dropped from 3.1 to $2.0\,\Omega$, so $I_C R_N$ is increased by just 10%.

measurements. At $T = 1.9\,K$, we measured (Fig. 3.5) $I_C = 7.0\,\mu A$, $I_{Ex} = 15\,\mu A$, and normal resistance $R_N = 43\,\Omega$, resulting in $I_C R_N = 294\,\mu V$, which compares favorably with the results on wide JoFETs presented by Kürsten (2002).

Overlapping sample 1093-14 of $w = 1.0\,\mu m$ width and $a = 40\,nm$ electrode separation was prepared and measured by Christian Busch as part of his diploma thesis (Busch, 2002). At $T = 1.7\,K$, we measured (Fig. 3.6) $I_C = 20\,\mu A$, $I_{Ex} = 42\,\mu A$, and normal resistance $R_N = 26\,\Omega$, resulting in $I_C R_N = 520\,\mu V$, which compares very favorably with the results on wide overlap junctions presented by Chrestin (1996) and of other junction geometries in this work. Further miniaturization to junction widths of less than $1\,\mu m$ is difficult, as the parallel bypass currents through the 2DES around the junction become relatively stronger. The junction still carries more than a tenth of the current of a comparable junction 20 times its width (e.g. 1093-31 pictured in Fig. 3.2(b)). The impact of bypass currents is also evidenced by the normal resistance $R_N = 26\,\Omega$ of the junction, which is far below the Sharvin resistance $R_{Sh} \approx 150\,\Omega$ calculated for an ideal junction of $w = 1.0\,\mu m$ width and typical carrier density $n_S = 1.2 \times 10^{12}\,cm^{-2}$ with Eq. 3.1. The situation is similar for the $1\,\mu m$ JoFET. This discrepancy is the result of an increased effective junction width due to bypass currents in the 2DES in combination with highly transparent interfaces. Additionally, a locally increased carrier density in the junction area could contribute to the magnitude of the discrepancy. Similar effects

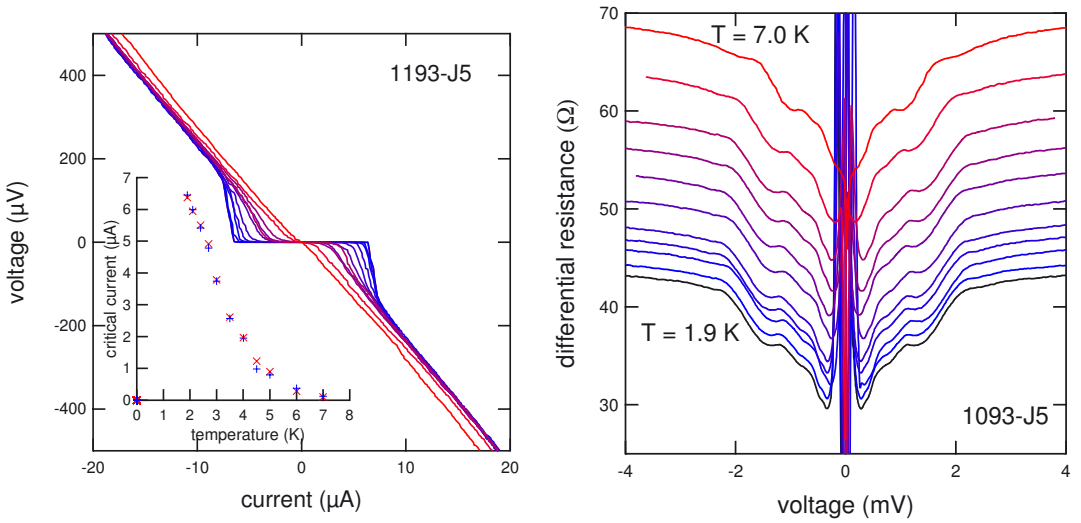


(a) (b)

**Figure 3.5:** Transport measurements on a 1.0 µm wide bulk JoFET 1093-J5. **(a)** Direct $I$-$V$-curves for temperatures from 1.9 to 7.0 K. The inset shows $I_C(T)$ extracted from the data. **(b)** Corresponding differential resistances, from the same measurements as in (a). Curves for temperatures above 1.9 K were offset for clarity.

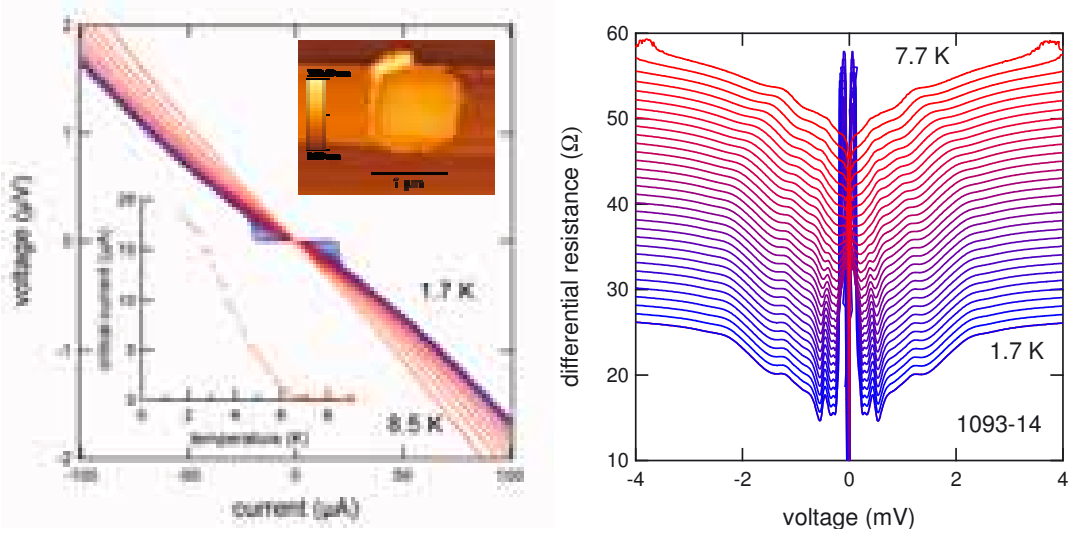


(a) (b)

**Figure 3.6:** Transport measurements on a 1.0 µm wide overlap junction 1093-14. **(a)** Direct $I$-$V$-curves for temperatures from 1.7 to 8.5 K. The insets show $I_C(T)$ extracted from the data and an AFM picture of the overlapping area. **(b)** Corresponding differential resistances, from the same measurements as in (a). Curves for temperatures above 1.7 K were offset for clarity.

| sample | 1146-91 | 1147-94 | 1147-6 |
|---|---|---|---|
| MBE wafer | 1146 | 1147 | 1147 |
| etching | 40 min rf | 55 s RIE + 4 min rf | 40 min rf |
| $w$ (µm) | 50 | 50 | 50 |
| $a$ (nm) | 250 | 250 | 250 |
| $I_C$ (µA) at 1.6 K | 6.8 | 28 | 14 |
| $R_N$ (Ω) at 1.6 K | 8.6 | 2.0 | 2.3 |
| $I_C R_N$ (µV) at 1.6 K | 58 | 56 | 32 |
| $I_{\mathrm{Ex}}$ (µA) at 1.6 K | 1.5 | 98 | <1 |
| $T_{10\%}$ (K) | 3.0 | 3.9 | 3.2 |

**Table 3.1:** Properties of HEMT JoFETs prepared with different etching techniques. The $T_{10\%}$ given is the temperature where $I_C(T_{10\%}) \leq 0.1 I_C(1.5\,\mathrm{K})$. This value is easier to compare than the true critical temperature $T_C$.

were noticed in numerous samples used to optimize the sputter system. The carrier density was determined by Shubnikov-de Haas measurements on comparable samples from the same wafer by Milde (2000). Bypass currents are unavoidable on bulk InAs, as a 2DES forms on the entire surface. In HEMT substrates, the conducting layer can be cut by etching techniques, thus it is possible to confine the 2DES and to avoid bypass currents. If further miniaturization to widths below 1 µm is desired, it should therefore be performed on HEMT substrates.

## 3.3. Comparison of Reactive Ion and Radio-Frequency Etching of InAs Heterostructures

As explained in Chap. 2.2.2, in HEMT structures it is necessary to etch through the cap layers to contact the 2DES buried 50 nm below the surface, as pictured in Fig. 2.4(a). To evaluate the two alternative etching techniques, two 50 µm wide JoFET samples with 250 nm electrode separation were processed identically as described in Chap. 2.2.2 except for the etching, where sample 1146-91 was rf etched for 40 minutes at an Ar pressure of 1.5 Pa and sample 1147-94 was RIE etched for 55 s, both processes yielding an etch depth of 60 nm. The samples were measured extensively, Tab. 3.1 shows a summary of their properties. Also included therein is the prototype sample 1147-6, which was prepared in a similar fashion but without gate and oxide, and at a time when the sputter system was impaired by a corroded cathode.

The RIE-etched HEMT JoFET 1147-94 displays the clearly developed subharmonic gap structure expected for a highly transparent SNS junction (Fig. 3.7). At least five peaks are visible, although peak 2 is not at an expected position for subharmonic gap structures and might be caused by a different process. The expected temperature de-

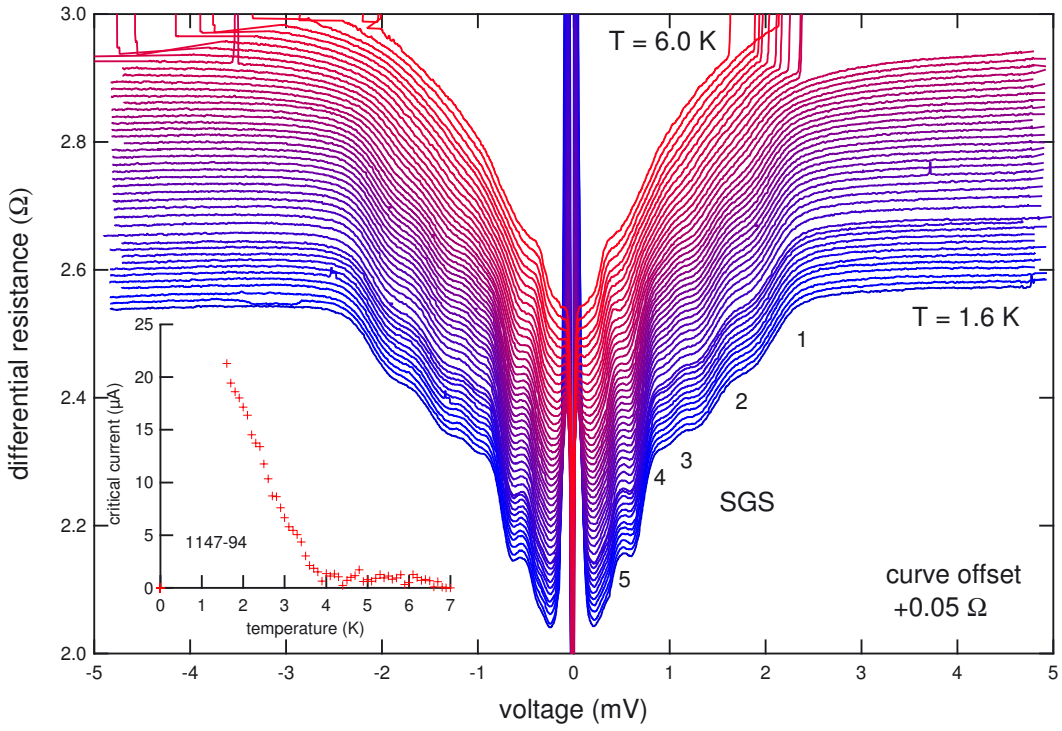


**Figure 3.7:** Differential resistances of the RIE etched HEMT JoFET 1147-94 in dependence of temperature. Curves were subsequently set off by 0.05 Ω for clarity. The positions of the subharmonic gap structure peaks marked $1, 3, 4, 5$ indicate an induced energy gap of $\Delta_N = 2.4$ meV. The inset shows the critical current determined by dc $I$-$V$-curves during the measurement. Note how the critical current seems to vanish above 4.0 K, while in the differential curve there is superconductivity evident even for $T = 6.0$ K.

pendence of subharmonic gap structures is exemplified in Fig. 3.3. At the highest temperatures, the distance between peaks has just begun to narrow, but still is nearer to the position for low temperatures than to zero. Clearly, there is superconductivity in the junction even at 6 K, though with much reduced $I_C$ that cannot be resolved properly in the dc measurement (included as inset in Fig. 3.7). Figures 3.8 and 3.9 depict the influence of applying a negative gate voltage, i.e. depopulating the 2DES, on the electrical properties of sample 1147-94. The resistance increases, while the subharmonic gap structure gets shallower and finally vanishes. At $V_{\text{gate}} = -20$ V, the junctions show tunnel behavior, as exemplified by the maximum of resistance at low voltages compared to the minimum in the weak link regime of low gate voltages. Positive voltages result in a slight increase of $I_C$ before saturating, but in no qualitative changes.

On sample 1147-94, additional measurements under microwave irradiation were performed by Baars (2004) to check for potential unusual behavior in the HEMT samples. The results comply with expectations of a highly transparent weak link with substantial

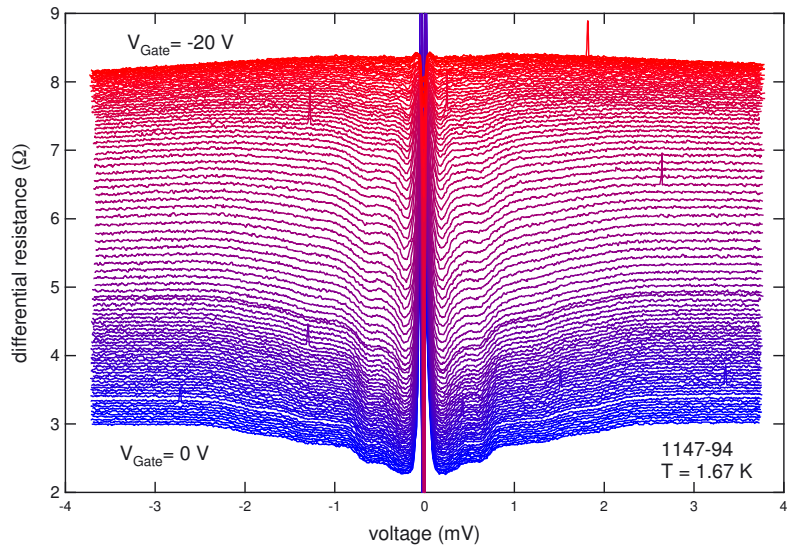


**Figure 3.8:** Differential resistances of the RIE etched HEMT JoFET 1147-94 in dependence of gate voltage from 0 to -20 V. Increasing negative gate voltages deplete the 2DES, resulting in increasing resistance and a change from weak link to tunnel junction behavior. This is exemplified by the change from decreased to increased resistances at low voltages, corresponding to a transition from concave to convex shape of the curves. Note that there is no shift in subharmonic gap structure positions in dependence of gate voltage. There is no offset added to the curves.

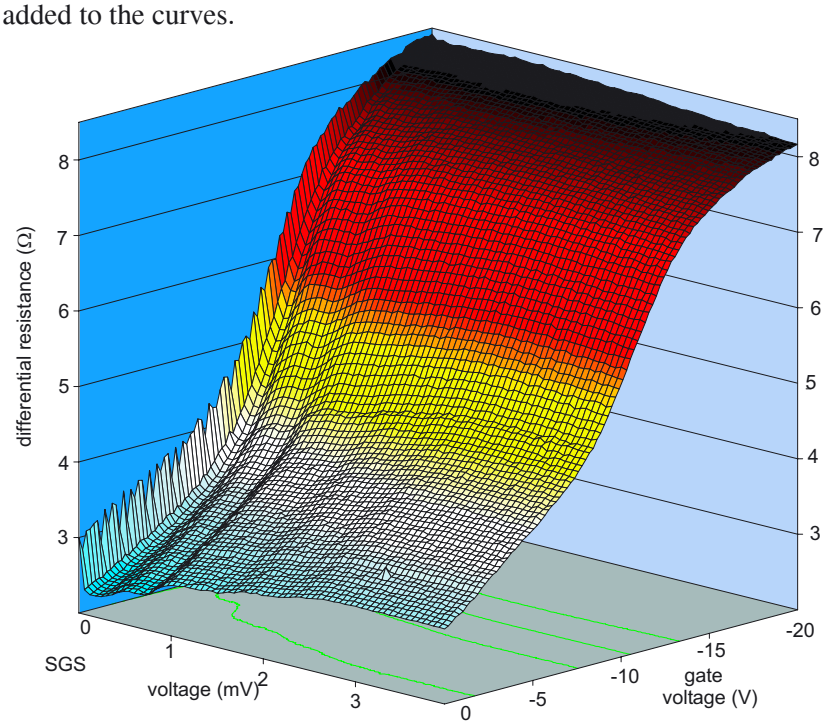


**Figure 3.9:** Right branch of the data shown in Fig. 3.8. Here the regions of carrier saturation and depletion are clearly visible as less steep regions. Note how the subharmonic gap structure, visible as parallel trenches, diminishes for voltages close to depletion.

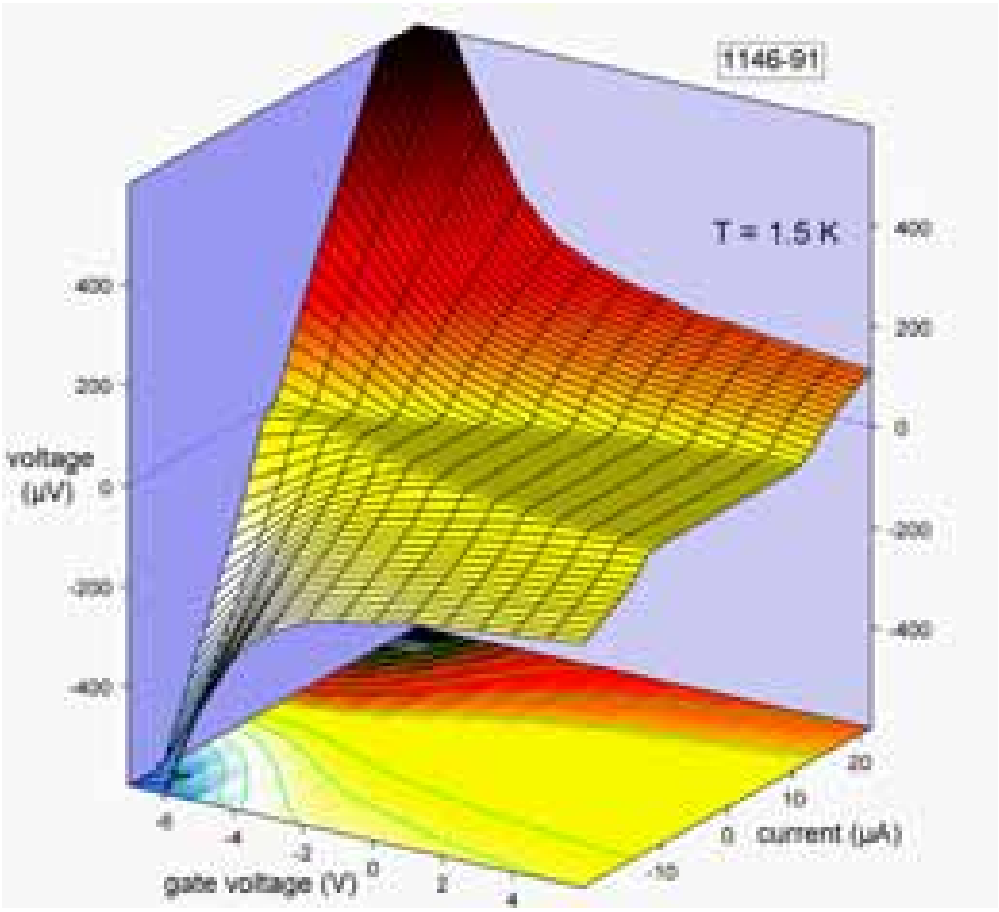


**Figure 3.10:** $I$-$V$-curves of rf etched HEMT JoFET 1146-91 in dependence on gate voltage $V_G$. The plateau represents the area of superconductivity. Outside the plateau, the gradient is proportional to the resistance of the sample. Note how negative gate voltages reduce the critical current while the resistance increases. At $V_G = -7$ V the supercurrent is suppressed completely. The supercurrent saturates for high positive gate voltages.

excess currents and could be fitted very well with the RCSJ+EX model presented in Baars et al. (2003).

The rf etched HEMT JoFET 1146-91 also shows superconductivity, with a rapid increase in critical current below 3 K (Fig. 3.11(b)). Figure 3.10 displays the gate voltage dependency of the direct $I$-$V$-curves. Similar to the RIE etched sample 1147-94, negative voltages decrease the critical current and increase resistance, while positive ones have small opposite effects that diminish as the 2DES nears saturation. The $I_C R_N$ product is nearly identical to the RIE etched sample. However, at somewhat higher currents than pictured in Fig. 3.10 drastic differences in behavior occur, visible in both the direct and the differential $I$-$V$-curves (Fig. 3.11). The unconventional structures in Fig. 3.11(c) are reproduced in following sweeps and show consistent shifting in depen-

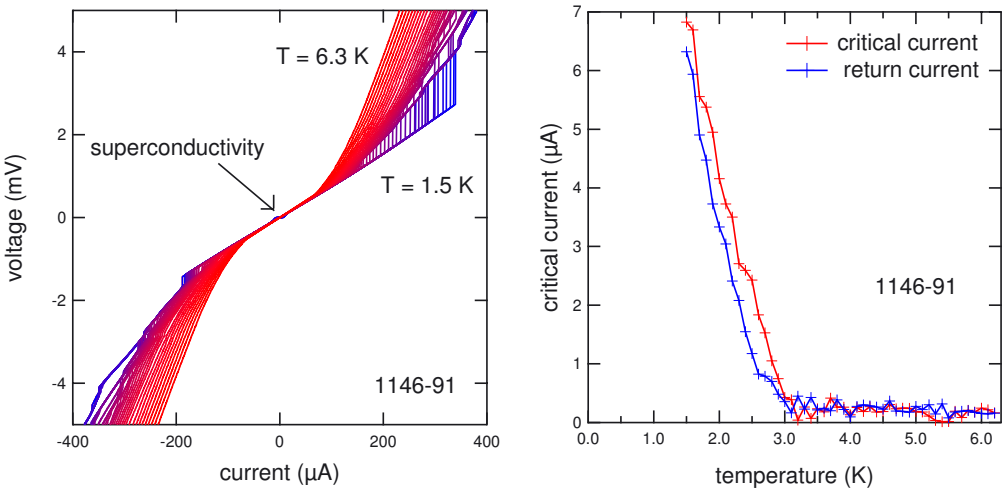


(a) (b)

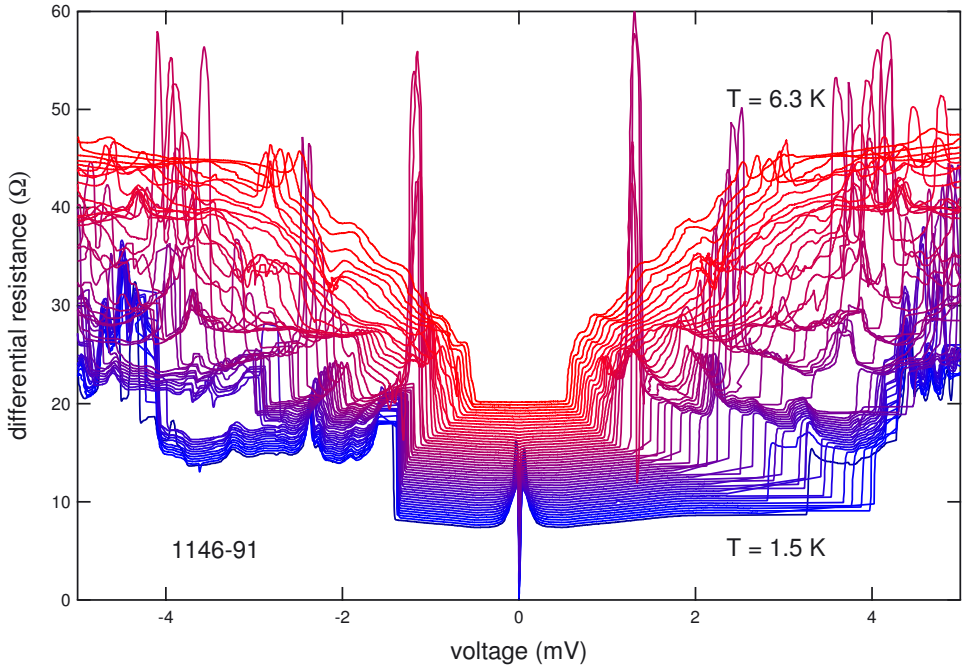


(c)

**Figure 3.11:** rf etched HEMT JoFET 1146-91 at temperatures between 1.5 and 6.3 K. **(a)** The direct $I$-$V$-curve shows only a small segment of proper superconductivity, but striking features at currents of some 100 µA. Such behavior would be expected if another junction was connected in series to the junction. **(b)** $I_C(T)$ extracted from (a). Note the steep decline and the low $T_C \approx 3$ K. There is little hysteresis. **(c)** The corresponding differential $I$-$V$-curve shows unconventional behavior, but is consistent with an interpretation of two superconductor connected in series. Curves were set off subsequently by 0.25 Ω for clarity.

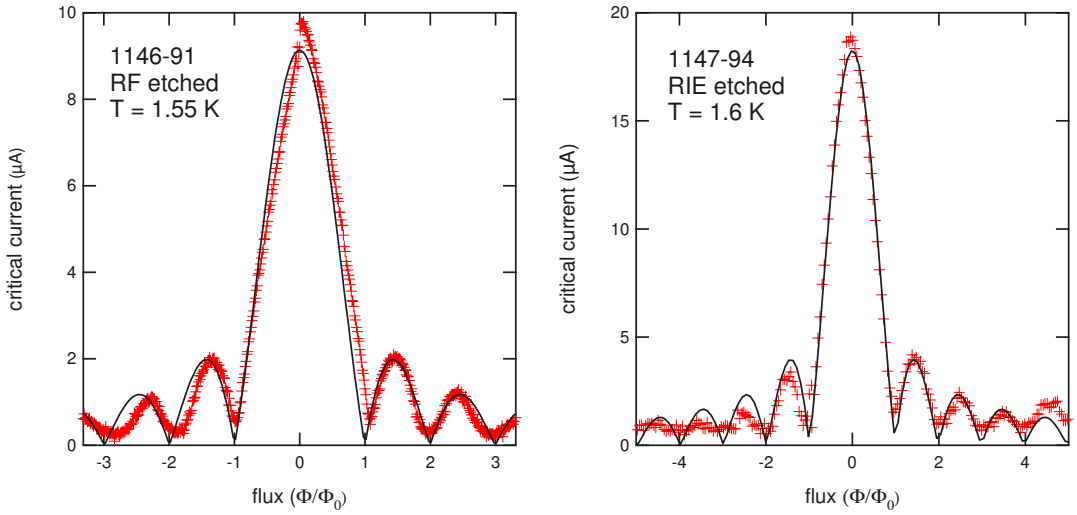


**Figure 3.12:** **(a)** Fraunhofer pattern of rf etched HEMT JoFET 1146-91. The crosses are experimental data, the line is a fit according to Eq. 3.2. **(b)** Corresponding Fraunhofer pattern of RIE etched HEMT JoFET 1147-94.

dence of temperature in a manner familiar from subharmonic gap structure peaks. This indicates a superconducting nature of the responsible processes. A possible explanation would be an additional junction with a critical current of some 100 µA and large hysteresis connected in series to the proper junction, e.g. caused by degraded interfaces or tunnel barriers between the Nb electrodes and the 2DES. This behavior was qualitatively replicated in the rf etched prototype sample 1147-6 without gate and oxide layer. This is evidence that the unusual behavior is caused by the etching process, as it occurred on the same wafer with the well-behaved 1147-94, and is not influenced by the presence or absence of an oxide layer. Possibly, a layer of sputter ejected substrate atoms constitutes a tunnel barrier between the 2DES and the Nb electrodes. Besides the nonexistent subharmonic gap structure, another indicator of poor interface transparency is the negligible excess current $I_{\mathrm{Ex}}$ in both rf etched samples, especially compared to the RIE sample, where $I_{\mathrm{Ex}} > 3I_C$. To check for spatial inhomogeneities in the junctions, the Fraunhofer patterns $I_C(B)$ of both samples were recorded (Fig. 3.12) and compared to the regular pattern according to equation 3.2. Both samples are in good agreement with the ideal pattern, indicating a homogeneous current distribution along the electrodes.

To summarize, both etching techniques could be employed successfully to build superconducting Josephson field-effect transistors on HEMT substrates, but the RIE etching method yields much better samples. Thus an additional RIE step is introduced into the preparation. The superior quality and the time saved in rf etching makes this effort worth while. But despite the nominally superior substrate material, the HEMT sam-

ples are not unambiguously better than junctions on bulk InAs. Their $I_C R_N$ product is one order of magnitude lower than the best samples prepared on bulk InAs. This may be a consequence of the much smaller contact area between Nb and 2DES in HEMT samples, or caused by possible contamination by the short rf etching still necessary even for RIE etched samples. This could be avoided if RIE and sputter deposition were performed in one system without breaking the vacuum. This remedy is possible in principle, but would require a major redesign of existing systems. Nevertheless, even with the mentioned problems the HEMT junctions are competitive with the best samples mentioned in literature (see Bagwell, 1999, for a recent review).

# 4. Current-Phase Relationship

For theoretical modeling of a Josephson junction, the dependency of the supercurrent $I_S$ flowing through it on the phase difference $\varphi$ across the junction is fundamental. Some general properties hold true regardless of the concrete realization. The relation is necessarily $2\pi$-periodic and odd, thus it can be expressed as the following Fourier series (with the critical current $I_C$):

$$I_S(\varphi) = I_C f(\varphi) = \sum_n I_n \sin(n\varphi) \tag{4.1}$$

$I_S(\varphi)$ is known as current-phase relationship (CPR), the dimensionless term $f(\varphi)$ as normalized CPR. The CPR is determined by the fundamental mechanisms of charge transport across the Josephson junction and in general is quite complex. However, in the important limiting case of vanishing transparency (as realized in a tunnel junction), only $I_1$ is relevant, reducing Eq. 4.1 to the well-known dc Josephson (1962) equation

$$I_S(\varphi) = I_1 \sin\varphi = I_C \sin\varphi. \tag{4.2}$$

For weak links with direct (i.e. non-tunnel) conductivity, such as our SNS junctions, more complex behavior and a non-sinusoidal CPR is expected. The CPR in SNS junctions can be interpreted as a consequence of the spectral distribution, phase dependency, and population of Andreev bound states in the weak link, additionally influenced by interface effects. This work is only concerned with the equilibrium CPR, and thus the spectral distribution of the Andreev bound states as caused by junction geometry and materials, but not with population changes by non-equilibrium effects, such as current injection or microwave irradiation.

We are interested in experimental access to the CPR as a way to test and to improve the theoretical models describing our junctions, as the conduction mechanisms in these devices are not fully understood, and indications of a significantly non-harmonic CPR in our junctions have been found in microwave measurements (Baars, 2000). The measurements deliver not only the dependency $f(\varphi)$, but also $I_C$, thus offering an independent comparison to transport measurements.

The investigation of the CPR is a collaboration between the University of Hamburg and Dr. Evgeni Il'ichev, Dr. Miroslav Grajcar, and their group at the Institute of Physical High Technology in Jena. Sample preparation and transport measurements were done in Hamburg, the CPR measurements were performed in Jena. Christian Busch prepared the overlap junctions as part of his diploma thesis (Busch, 2002).

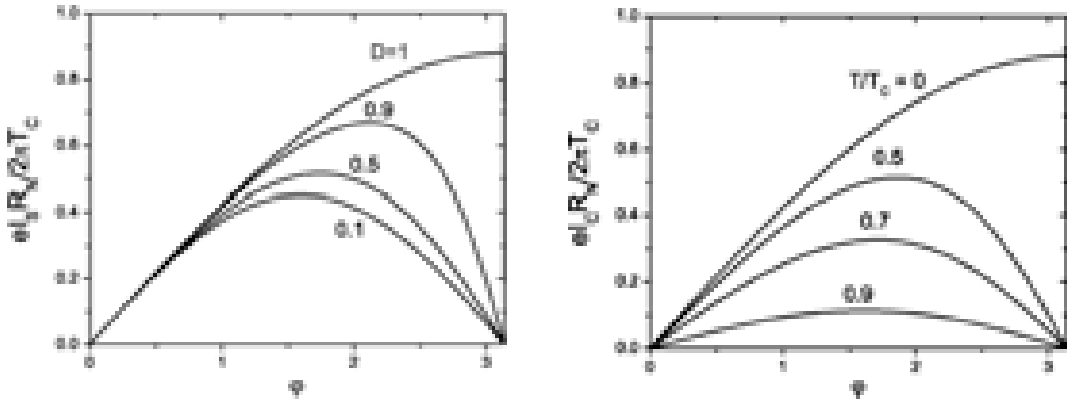


(a) (b)

**Figure 4.1:** Current-phase relationship as predicted by the generalized Kulik-Omel'yanchuk model for clean short junctions. Because of the inherent symmetry of the CPR, it is customary to depict the phase range between 0 and $\pi$ only. The current is expressed in relation to fundamental factors to show the amplitude as well as the shape change. **(a)** At zero temperature, increasing transparencies result in rising supercurrents and a shift of the position of the maximum from $\pi/2$ towards $\pi$. Finally, the CPR approaches a saw tooth shape. **(b)** For decreasing temperatures and ideal transparency $D = 1$, the supercurrent increases, the position of the maximum shifts from $\pi/2$ to $\pi$, and the CPR shape shifts towards a saw tooth. Taken from Golubov et al. (2004).

## 4.1. Theory of the Current-Phase Relationship

A detailed review of the many theories concerned with the CPR in Josephson junctions is beyond the scope of this work (see Golubov et al. (2004) for a recent review). We will introduce the earliest model to show the qualitative aspects of the CPR encountered in our experiments, developed by Kulik and Omel'yanchuk (1977). We then present the model developed by Grajcar et al. (2002), which we used to fit our data. The Kulik-Omel'yanchuk result is reproduced by the Grajcar model in the limit of an ideal point contact.

Kulik and Omel'yanchuk investigated theoretically the CPR for the ideal weak link system of a quasiclassical point contact. Their first model (Kulik and Omel'yanchuk, 1975) is concerned with the diffusive ($l \ll a$) and dirty limit ($l \ll \xi_0$), with mean free path $l$ and coherence length $\xi_0$. Relevant for our purposes is their model for a weak link in the fully ballistic ($l \gg a$) and clean limit ($l \gg \xi_0$). By solving the Eilenberger equations, they obtained (Kulik and Omel'yanchuk, 1977):

$$I_S(\varphi) = \frac{\pi\Delta}{eR_{\mathrm{Sh}}} \sin(\varphi/2) \tanh \frac{\Delta \cos(\varphi/2)}{2T}. \tag{4.3}$$

Note that no properties of the junction except its Sharvin resistance (dependent on geometry and carrier density) enter the model, all other parameters are determined by

the superconductor. This equation predicts a CPR $f(\varphi)$ changing from a sinusoidal curve to a saw tooth shape for decreasing temperatures. Haberkorn et al. (1978) generalized Eq. 4.3 to arbitrary transparencies $D$, thus taking a crucial junction characteristic into account. The resulting CPRs are plotted in Fig. 4.1. For low transparencies, the deviations from a sinusoidal CPR vanish.

The Kulik-Omel'yanchuk model is quite simple and can be solved analytically, in contrast to the more advanced models such as the Grajcar model presented later. Their model is very useful to show the basic qualitative changes in the CPR. However, due to its restrictive assumptions, its applicability to real samples is limited. One system approximating the Kulik-Omel'yanchuk ideal is the point contact known as mechanically controlled break-junction (Muller et al., 1992; Scheer et al., 1997). In this superconductor-constriction-superconductor (ScS) weak link the constriction area can be controlled mechanically down to atomic size and even beyond, to the tunnel regime. This is also one of the few systems where CPR measurements were published, performed by Koops et al. (1996) using a flux-detecting method. Their results agreed qualitatively with the changes in the position of the maximum and curve shape predicted by the Kulik-Omel'yanchuk model.

In addition to the fundamental mechanisms determining the CPR in the ideal model systems analyzed by Kulik and Omel'yanchuk and in the break junctions, our SNS junctions exhibit a finite length, some scattering of electrons in the 2DES, and an area of induced superconductivity around the electrodes caused by the proximity effect (de Gennes, 1964; Chrestin et al., 1997). To describe the non-sinusoidal CPR in our experiments, Grajcar et al. (2002) combined the scattering matrix formalism of Brouwer and Beenakker (1997) and the SNcNS constriction model of Aminov, Golubov, and Kupriyanov (1996). In the Grajcar model, the phase-dependent Josephson current through a double-barrier structure is calculated numerically according to

$$I(\varphi) = \frac{16\pi k_B T}{eR_0} \sum_{n=0}^{N-1} \sum_{m=0}^{\infty} \frac{-A^2 |S_{12}|^2 \sin(\varphi)}{1 - 2A^2(|S_{12}|^2 \cos(\varphi) + |S_{11}|^2) + A^4 |S_{11}^2 + S_{12}^2|^2}, \qquad (4.4)$$

where $R_0 = h/e^2$ is the resistance quantum, $N = 2w/\lambda_F$ is the number of transmission channels, $\lambda_F = \sqrt{2\pi/n_S}$ is the Fermi wavelength, $A$ is the coefficient of the Andreev reflection, and $S_{ij}$ are scattering amplitudes in a symmetric double barrier junction (Belogolovskii et al., 1999)

$$S_{11} = |r| + |r||t|^2 p_n^2/(1 + |r|^2 p_n^2), \quad S_{12} = |t|^2 p_n/(1 + |r|^2 p_n^2). \qquad (4.5)$$

Here $|r|^2, |t|^2$ are the reflection and transmission probabilities of the left and right-hand barriers, $p_n = \exp(ik_{Fn}a - \omega_m a/\hbar v_{Fn})$, where $\omega_m = (2m+1)\pi k_B T$ are Matsubara frequencies, $k_{Fn}$ and $v_{Fn}$ are components normal to the barriers of the wave vector and Fermi velocity of the $n$-th mode transverse to the barriers and $a$ is the distance between

the barriers. The reflection and transmission coefficients are determined following the BTK approach (Blonder et al., 1982) in the form

$$|t|^2 = 1 - |r|^2 = \frac{1-(n/N)^2}{(1-(n/N)^2)(\eta+1)^2/4\eta + Z^2} \tag{4.6}$$

where $Z$ is the dimensionless potential barrier strength and $\eta = v_{Fs}/v_{Fn}$ is the Fermi velocity mismatch.

In order to calculate the Josephson current from Eq. 4.4, one must determine the Andreev reflection coefficient $A$. Since superconductivity is induced in InAs by the proximity effect, the coefficient $A$ may be written as $A = iF/(1+G)$ (Aminov et al., 1996), where $F$ and $G$ are Green functions in the inversion layer of InAs. Due to the low electron density of the two-dimensional inversion layer compared to the bulk superconductor, the suppression of the pair potential in the Nb electrodes can be neglected and $F, G$ can be expressed by the McMillan equations (Golubov et al., 1995)

$$G = \omega/\sqrt{\omega^2+\Phi^2},\ \ F = \Phi/\sqrt{\omega^2+\Phi^2},\ \text{and}\ \ \Phi = \tilde{\Delta}/(1+\gamma_B\sqrt{\tilde{\omega}^2+\tilde{\Delta}^2}), \tag{4.7}$$

where $\gamma_B$ is a dimensionless parameter characterizing the transparency of the NS interface between Nb and InAs (introduced by Aminov et al. (1996), low $\gamma_B$ means high transparency), $\tilde{\Delta} = \Delta/\pi k_B T_C$, $\tilde{\omega} = \omega/\pi k_B T_C$, $\Delta$ is the superconducting energy gap of bulk Nb, and $T_C$ its critical temperature. Both the critical temperature and the energy gap of the Nb can be suppressed near the interface because of disorder (Belitz and Kirkpatrick, 1994) but $\tilde{\Delta} \approx 0.6$ remains constant (Smith et al., 1995). The critical temperature $T_C$ can be determined from temperature-dependent measurements. $Z = 0$ is assumed, i.e. no real barrier is supposed to exist between the 2DES and the superconducting electrodes. Thus, there are only two free fitting parameters in the model, the carrier density $n_S$ and the interface parameter $\gamma_B$. The Fermi velocity $v_F$ and Fermi wave vector $k_F$ are calculated for a given value of $n_S$. Since the normal resistance $R_N$ of a transparent junction depends on $n_S$ as well, the $n_S$ obtained from the fit can be verified comparing the theoretical and experimental value of $R_N$.

## 4.2. Current-Phase Relationship Measurement Technique

The CPR of the Josephson junction is determined by an inductive rf frequency method requiring no galvanic contacts to the sample, thus reducing noise. This technique was introduced by Rifkin and Deaver (1976) and improved by Il'ichev. Alternative methods to evaluate the CPR are based on measurements of critical currents and Shapiro steps as a function of the amplitude of external monochromatic electromagnetic radiation (Gubankov et al., 1976) or direct flux measurement (Jackel et al., 1974). However, these methods are not as sensitive, flexible, and noise-tolerant as the inductive method. A short description follows, for a detailed account see Il'ichev et al. (2001).

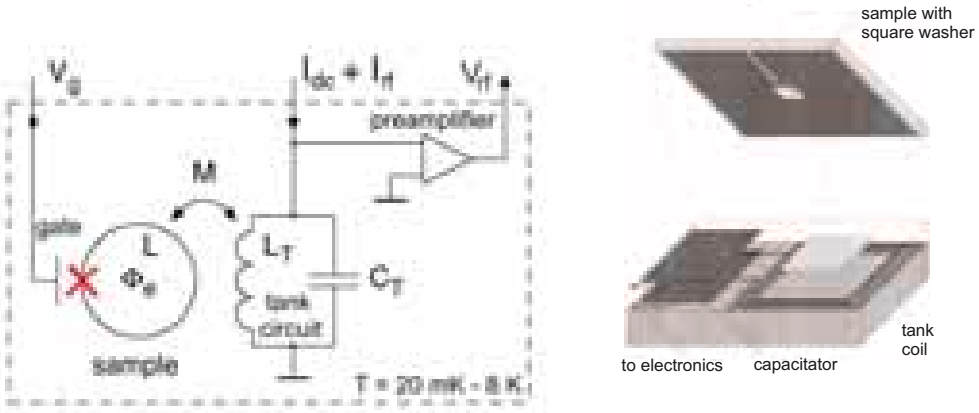


(a) (b)

**Figure 4.2:** **(a)** Equivalent circuit of the CPR measurement setup. The sample is coupled via the mutual inductance $M$ to the tank circuit, which is connected to the electronics. The dashed box symbolizes the cooled area. The gate electrode is optional. **(b)** Schematic of the sample and a micro-fabricated tank circuit in flip-chip arrangement. Adapted from Götz et al. (2000).

### 4.2.1. Principle

The junction to be investigated is incorporated into a bulk superconducting loop to form a single junction interferometer, also known as rf SQUID, of inductance $L$. The dynamics of such loops were intensely investigated because of the technical importance of SQUIDs, see e.g. the detailed analysis by Silver and Zimmerman (1967). If an external magnetic flux $\Phi_e$ is applied to the interferometer, circulating supercurrents $I_S$ are induced and a certain flux $\Phi_i$ is admitted to the loop. As a consequence of fluxoid quantization, the phase difference $\varphi$ across the junction in this case is

$$\varphi = 2\pi\frac{\Phi_i}{\Phi_0} \text{ modulo } 2\pi, \tag{4.8}$$

where $\Phi_0$ is the flux quantum. Thus, the phase can be set stably to any value $0 < \varphi < 2\pi$, and we need to measure the current to determine the CPR. The difference between external and admitted flux gives the current through the loop $I_S = (\Phi_i - \Phi_e)/L$.

If we neglect thermal fluctuations and assume that all relevant current across the junction is superconducting (this is justified for the limits $\omega L/R_N \ll 1$ and $LC\omega^2 \ll 1$ with $\omega$ as rf frequency, which are satisfied by our samples), we can merge the last two equations into

$$\varphi = \varphi_e - \beta f(\varphi) \text{ modulo } 2\pi, \tag{4.9}$$

using $\varphi_e = 2\pi\Phi_e/\Phi_0$ and $\beta = 2\pi LI_C/\Phi_0$ as normalized external flux and normalized critical current. In principle, the CPR can now be measured by monitoring $\varphi$ via $\Phi_i$ in dependence of $\Phi_e$ with a flux detector. This method was introduced by Jackel et al.

(1974) and has been employed by Koops et al. (1996) in his investigation of break-junctions, but it is hard to measure the admitted flux $\Phi_i$ with the required precision.

For the rf method used in this project, we couple the interferometer inductively to a high-quality oscillator known as tank circuit (characterized by inductance $L_T$, capacitance $C_T$, and quality factor $Q$) through a mutual inductance $M = k\sqrt{LL_T}$, with $k$ describing the strength of the coupling. Figure 4.2(a) shows a sketch of the principle. To create the external magnetic flux $\Phi_e$, a slowly ramped quasi-dc current $I_{\mathrm{dc}}$ is driven through an inductivity. In principle, this could be done in a separate coil, but it is easier to use the tank coil. To bring the tank circuit into oscillation, a very small rf current $I_{\mathrm{rf}}$ with a frequency $\omega$ close to the resonance of the circuit $\omega_0 = 1/\sqrt{L_T C_T}$ is applied to the oscillator. This also creates a component $\Phi_{\mathrm{rf}}$ of the external flux, but it can be neglected if $\Phi_{\mathrm{rf}} \ll \Phi_0$, which is assured by a sufficiently small amplitude of $I_{\mathrm{rf}}$.

The electrical properties of the tank circuit change if the sample is coupled to it. The effective resistance $R_{\mathrm{eff}}$ and inductance $L_{\mathrm{eff}}$ of the oscillator depend on changes of the current in the interferometer loop:

$$L_{\mathrm{eff}} = L_T \cdot \left(1 - \frac{k^2 \cdot \beta f'(\varphi)}{1 + \beta f'(\varphi)}\right), \tag{4.10}$$

$$R_{\mathrm{eff}} = R_T \cdot \left(1 + \frac{k^2 Q \cdot \omega\tau}{(1 + \beta f'(\varphi))^2} \cdot \frac{\omega}{\omega_0}\right). \tag{4.11}$$

$R_T$ symbolizes losses in the uncoupled tank circuit and is determined from $Q$. For vanishing coupling $k$ these equations reduce to the pure tank circuit values. A changing supercurrent in the coupled interferometer alters the electrical properties of the oscillator and thus its resonance frequency $\omega_0 = 1/\sqrt{L_{\mathrm{eff}} C_T}$. This detuning influences the phase shift $\alpha$ between the driving current $I_{\mathrm{rf}}$ and the rf component $V_{\mathrm{rf}}$ of the voltage $V_T$ across the oscillator according to

$$\tan\alpha = \frac{1}{R_{\mathrm{eff}}(\varphi_e)} \cdot \left(\frac{1}{\omega C_T} - \omega L_{\mathrm{eff}}(\varphi_e)\right). \tag{4.12}$$

The dependency of this shift on the external flux through the sample $\alpha(\varphi_{\mathrm{dc}})$ is measured, an example is given in Fig. 4.7(a). This signal is periodic, each period corresponding to one flux quantum $\Phi_0$ admitted to the loop. From the periodicity the coupling coefficient $k$ between sample and tank circuit is determined, as the current needed to create a flux quantum is $\Delta I_{\mathrm{dc}} = \Phi_0/M$ and $M = k\sqrt{LL_T}$. Thus fluxoid quantization provides an easy method to calibrate $\varphi_{\mathrm{dc}}$, which is physically relevant for the CPR reconstruction, to the current $I_{\mathrm{dc}}$ which we control. In combination with the quality factor $Q$ (determined by measuring the width of the resonance peak), the derivative of the CPR $f'(\varphi)$ can be calculated by combining Eq. 4.10, 4.11 and 4.12 to

$$\tan\alpha = \frac{k^2 Q \cdot \beta f'(\varphi)}{1 + \beta f'(\varphi)}. \tag{4.13}$$

Together with the expression

$$d\varphi = \frac{d\varphi_{\mathrm{dc}}}{1+\beta f'(\varphi)}, \tag{4.14}$$

derived from Eq. 4.9, we can calculate the CPR by numerically integrating the following equation:

$$I_S(\varphi) = \frac{I_C}{k^2 Q\beta} \int_0^{\varphi_{\mathrm{dc}}} \tan\alpha(\varphi_{\mathrm{dc}}) d\varphi_{\mathrm{dc}}. \tag{4.15}$$

Note that there are no fitting parameters necessary to reconstruct the CPR. All necessary values for the numerical factor can be measured independently using conventional techniques.

### 4.2.2. Limitations

In the description above assumptions and simplifications were made, limiting the range of applicability of the technique. The SQUID enters the hysteretic regime if $\beta f'(\varphi)$ approaches unity, where $\beta = 2\pi L I_C/\Phi_0$ is the normalized critical current and $f'(\varphi) = df(\varphi)/d\varphi$. Remember that $f(\varphi)$ as normalized CPR has a maximal gradient $f'(\varphi)_{\max} = 1$ for a sinusoidal CPR, but non-sinusoidal CPRs have greater maximal gradients. Thus the hysteretic regime is reached for strongly non-sinusoidal CPR for $\beta < 1$. A hysteretic SQUID can jump between different meta-stable states (Kurkijärvi, 1972, analyzed this regime in detail). This corresponds to a multi-valued CPR, which we cannot reconstruct, as there is no longer a unambiguous correspondence between phase and current. We avoid this regime by reducing $\beta$ with low critical currents of the junction and low inductances $L$ of the SQUID loop. Successful measurements have been made with $0.005 \lesssim \beta \lesssim 1$, but $0.1 < \beta < 0.8$ is desired. As the critical current $I_C$ is proportional to $\beta$ and varies by more than an order of magnitude depending on the temperature, matching can only be good in a certain temperature range. The devices are optimized for low temperatures, because deviations from harmonic behavior are predicted to be most significant in this range.

Thermal fluctuations were neglected in the discussion. Their effects were analyzed in detail by Jackel et al. (1974). Thermally activated transitions between meta-stable states in the loop, carrying different currents, influence the flux $\Phi_i$ inside. This effect depends on temperature, which creates the fluctuations, and on the interferometer inductance, which determines how strongly the fluctuations influence the enclosed flux. Thermal fluctuations can prevent measurements if the threshold inductance

$$L_f = \frac{(\Phi_0/2\pi)^2}{k_B T} \tag{4.16}$$

is comparable to the loop inductance $L$. Note that $L_f$ depends only on temperature. However, as $L_f = 1.7\,\mathrm{nH}$ at 4.2 K, we are two orders of magnitude below this limit, so only a small effect is expected. As shown by Il'ichev et al. (1998), thermal fluctuations

at lower temperatures result in a shift of the position of maximum current $\varphi_{max}$ towards zero. Also, any fluctuations in external flux, as caused e.g. by the rf current or noise introduced through a gate electrode, result in qualitatively similar effects[1]. Thus, we have noise effects shifting $\varphi_{max}$ towards zero, i.e. in the opposite direction of the fundamental effects. Note that these effects depend not on the junction itself, but on the loop and the environment. Therefore they occur as well in a conventional $Nb/Al_2O_3/Nb$ tunnel junction (with purely sinusoidal CPR) in a comparable loop, which is used to calibrate the system and to evaluate the influence of noise. Measurements with the calibration sample (an example in included in Fig. 4.9) show that only very small shifts occur, so neglecting these influences is justified.

In contrast to these universal effects, the depairing effect in the electrodes is junction specific. It was investigated by Ivanov (1981). Depairing, i.e. the suppression of the superconducting pair potential and thus of the Cooper pair density, is caused by two effects. The superconductivity in the electrodes can be suppressed by the proximity effect; this effect is quite weak in our junctions because of the relatively low number of states in the 2DES compared to the three-dimensional metal of the electrodes and thus can be neglected. Depairing also impairs the superconductivity in very short junctions ($a \ll \xi$) for high current densities. In both cases, depairing causes a shift of $\varphi_{max}$ towards zero and a decrease of critical current, similar to the other noise effects.

### 4.2.3. Experimental Realization

The measuring hardware is realized at the IPHT Jena as a compact module, consisting only of the tank circuit with micro-fabricated Nb pancake coils, a cooled GaAs HEMT preamplifier (Oukhanski et al., 2003), and some filters. This module can be fitted into standard gas flow cryostats, e.g. an Oxford Instruments "Heliox 2" 300 mK system with magnetic shielding. Several different modules are available, with varying resonance frequencies and coil materials (Cu coils instead of Nb are used for experiments around 77 K). Typically, inductances between $L_T = 10$ and 1000 nH and resonant frequencies $\omega = 5$ to 40 MHz are used. The cryostat is connected to standard laboratory electronics such as lock-in amplifiers and digital oscilloscopes.

## 4.3. Design and Preparation of Samples for Current-Phase Measurements

This chapter describes the preparation of samples optimized for CPR measurements. These samples must fulfil several conflicting requirements. Table 4.1 aims to give an overview of their interrelations. To show maximum deviations from a sinusoidal

[1] Note that because we measure the phase shift of a resonant oscillator, only noise with a frequency in the small resonance band is harmful.

| | **increasing factors** | **decreasing factors** | **goal/limit** |
|---|---|---|---|
| **non-harmonic CPR** | transparency $D$ | temperature $T$ | large deviations from $\sin\varphi$ |
| **critical current** $I_C$ | width $w$<br>transparency $D$<br>carrier density $n_S$ | temperature $T$<br>channel length $a$ | large $I_C R_N$<br>$\beta = 2\pi L I_C/\Phi_0 < 0.8$ |
| **normal resistance** $R_N$ | channel length $a$ | width $w$<br>transparency $D$<br>carrier density $n_S$<br>bypass currents | large $I_C R_N$ |
| **interferometer inductance** $L$ | interferometer size | parallel inductances | $\beta = 2\pi L I_C/\Phi_0 < 1$<br>$L \ll (\Phi_0/2\pi)^2/k_B T$ |
| **coupling mutual inductance**<br>$M = k\sqrt{L L_T}$ | interferometer inductance $L$<br>tank circuit inductance $L_T$<br>flux transformer | distance sample–tank<br>misalignment | $k \approx 0.01$ |

**Table 4.1:** Overview of the parameters relevant in the design of samples for CPR measurements and their main dependencies. We aim to observe non-harmonic deviations from a sinusoidal CPR, therefore we need Josephson junctions with high transparency $D$ and low temperatures $T$. These parameters also increase the critical current $I_C$ of the junction, conflicting with $\beta = 2\pi L I_C/\Phi_0 < 0.8$. To lower $I_C$ without decreasing the transparency or the $I_C R_N$ products, we decrease the junction width. To further lower $\beta$, the interferometer inductance $L$ is decreased as well by shrinking the interferometer. Decreasing $L$ has the added benefit of reducing interferences of thermic fluctuations $L \ll (\Phi_0/2\pi)^2/k_B T$. However, if $L$ decreases, the coupling strength $k$ should be increased to maintain sufficient mutual inductance $M$ between sample and tank circuit. The critical current $I_C$ and the normal resistance $R_N$ are determined during the preparation of the Josephson junction. The interferometer inductance $L$ depends on the interferometer size and geometry. The coupling strength $k$ depends chiefly on the relative alignment and distance of the sample and the tank circuit.

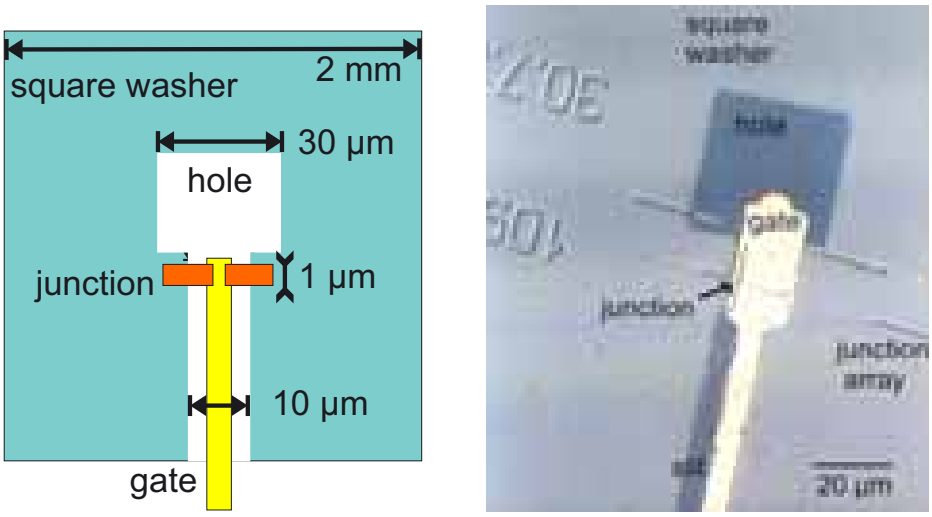


(a) (b)

**Figure 4.3:** **(a)** Schematic of a square washer as used for the JoFET measurements. The interferometer inductivity L is determined by the size of the hole, the washer area serves as a flux concentrator. **(b)** JoFET 1093-J9 in a $30 \times 30\,\mu m^2$ square washer with a gate electrode. The connected junction is covered by the gate. Several potential junctions are prepared as an array, the most promising is selected for further processing.

CPR, the Josephson junctions should have excellent interface transparency and large $I_C R_N$ products. This can be achieved by the standard fabrication processes described in Chap. 2. To simultaneously get low critical currents, the junctions are built with reduced geometrical width $w$. For the preliminary transport measurements, corresponding to the ones presented in Chap. 3.2, the junctions are contacted for conventional four-point-probe measurements. The transport measurements yield the normal resistance of the junction, which is not accessible with the inductive method, and allow us to compare the critical currents determined by both methods. The electrodes needed for transport measurements disturb the CPR measurements. Thus transport measurements either are performed on identically prepared samples from the same wafer or, preferably, the leads are removed by dry etching after completing the transport measurements on the sample.

### 4.3.1. Interferometer Loops

The junction is enclosed into a superconducting Nb loop to prepare it for the CPR measurement. The result is a single-junction interferometer, better known as rf SQUID, of an inductivity $L$ determined by size and geometry of the loop. This inductivity must be adapted to the critical current of the junction $I_C$ to satisfy $\beta = 2\pi L I_C/\Phi_0 < 1$. Note that "loop" is used in a topological sense, and in general is not a simple ring. The most common SQUID loop design is the so-called square washer as pictured in Fig. 4.3(a). This

| **interferometer type** | square washer | multiloop with flux transformer | mini-loop with on-chip coil |
|---|---|---|---|
| **preparation** | easy | challenging | challenging |
| **inductivity** | high | low | very low |
| **gate possible** | yes | no | yes |
| **depicted in** | Fig. 4.3(a) | Fig. 4.4 | Fig. 4.5 |
| **used for** | all JoFETs | overlap 1095-21 | |

**Table 4.2:** Overview of the interferometer types used in this work.

washer design was used for all the JoFET samples presented in this chapter. The large area of the washer serves to focus the flux into the hole. The inductivity of the interferometer can be calculated for simple geometries, using e.g. the Ketchen et al. (1985) formula for square washers. In all cases, the inductivity can be measured independently using standard techniques.

For the CPR measurement, the interferometer structure must have low inductivity to avoid the SQUID entering hysteretic regime, but it has to maintain sufficient coupling via the mutual inductance $M = k\sqrt{LL_T}$ to the tank circuit and must not decrease the junction quality. As the inductivity is chiefly determined by the size of the area enclosed by the loop, reducing $L$ is a straightforward process of shrinking the interferometer. Loops from $50 \times 50$ down to $6 \times 6\,\mu\text{m}^2$, corresponding to inductivities of 80 to 11 pH, have been fabricated for this project. Due to the flux focusing effect of the extended washer area, precise alignment of loop and coil centers on neighboring chips (as shown in Fig. 4.2(b)) is sufficient to couple square washers with relatively high inductivity to the tank circuit. To simultaneously achieve low inductivities and sufficient coupling, we employ two advanced designs in addition to the simple square washer: a flux transformer mediating between tank circuit and interferometer, and a coil acting as part of the tank circuit. An overview of interferometer properties is given in Tab. 4.2.

#### Integrated Flux Transformer

A flux transformer intermediates between the tank coil and the small inductivity of the interferometer loop. It is composed of a large pick-up loop with only one turn and a secondary coil of many turns precisely aligned with the interferometer loop. In this way, it collects the flux from the tank coil and concentrates it inside the interferometer loop. The transformer is integrated on the sample, requiring no additional leads. Thus, the tank circuit is not affected by this design, which is advantageous for changing samples or cryostats. We combined this flux transformer with six square washers connected in parallel to reduce the inductance while retaining a large flux focussing area. Figure 4.4(a) shows the wiring scheme, Figs. 4.4(b)–(d) depict the overlapping sample 1095-21 with this structure. Its inductance was measured as $L = 19\,\text{pH}$. To

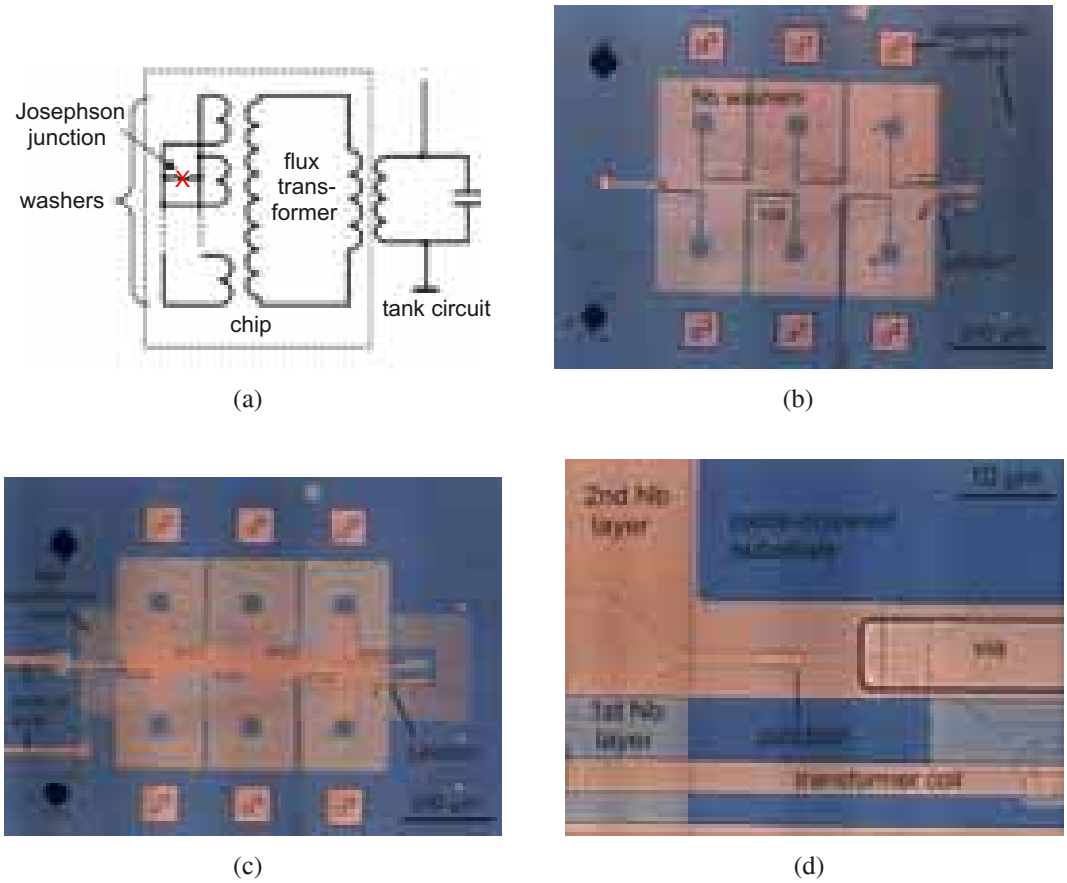


**Figure 4.4:** **(a)** Equivalent circuit of the advanced multiloop design with integrated flux transformer. The primary coil of the transformer couples to the tank circuit, the secondary to the washer structure. The design for the overlap junction 1095-21 uses six washers, a primary coil of only one turn (also called pick-up loop) and a secondary coil of nine turns. **(b)** Sample 1095-21 during preparation. The first Nb layer consists of six square washers connected in parallel to the junction. The structure is covered by an insulating layer, in which vias have been etched to connect to the second Nb layer. **(c)** The flux transformer in the second Nb layer completes the sample 1095-21. The Nb leads leading out of the picture are part of the pick-up loop, which encloses 1 $mm^2$. **(d)** Close-up of the junctions area. The overlap junction is only $1 \times 1\,\mu m^2$ square.

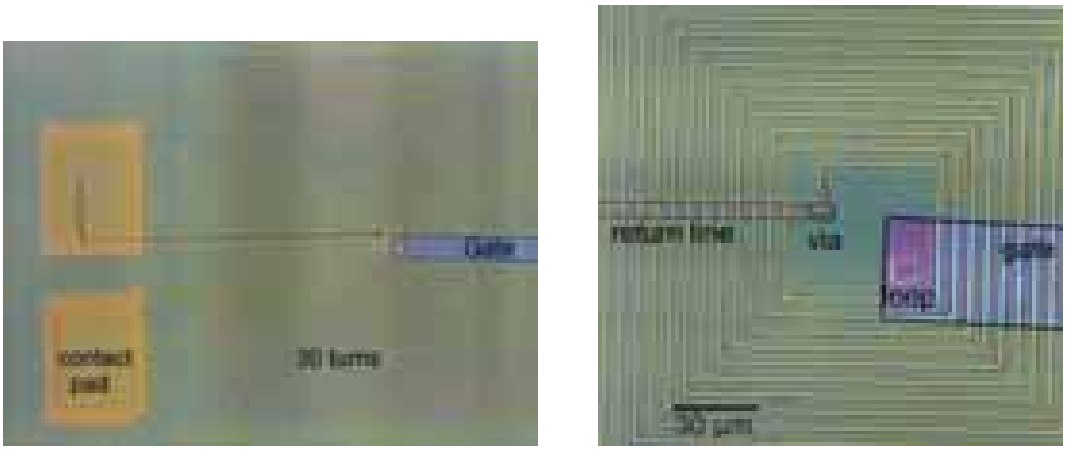


(a) (b)

**Figure 4.5:** **(a)** 30-turn on-chip coil prototype. The area of the gate is exposed, but not yet metalized. **(b)** Close-up of the inner area. Note the $10 \times 10\,\mu m^2$ Josephson junction interferometer loop. The return line connects the innermost coil turn with a contact pad. For insulation, it is separated by $SiO_2$ from the coil, except for the via areas, where the oxide has been removed by wet etching.

minimize inductivity, the electrodes connecting the junction must not enclose an open space, complicating insulation. In our design, the electrodes lie on top of each other, separated by $SiO_2$. This is suitable for overlapping structures, but incompatible with gated structures, as the electrodes shield the junction from external fields, thus JoFETs cannot be measured with this multiloop washer design.

#### On-chip Tank Circuit Coil

The coil of the tank circuit can be prepared directly on the sample, thus allowing minimal distances and exact alignment with the interferometer. This design allows gated structures and thus is suited for JoFET measurements. High quality factors of the tank circuit ($Q > 100$) are required, which are challenging to achieve with on-chip coils, as we have to prepare a coil with technologies compatible to our InAs/Nb process and connect it by wires to a capacitance outside the sample. At the IPHT Jena, quality factors of $Q > 500$ (and $> 1000$ if the Al bonding wires are superconducting at $T < 1.3\,K$) were achieved by May et al. (2003) using Nb pancake coils on Si wafers with evaporated silicon monoxide $SiO_1$ as insulator. Preparation of a sufficient coil is also possible employing the material combination Nb and $SiO_2$ available in our institute. This requires some adjustments to our established fabrication process, developed for the low currents and low voltages encountered in SNS devices. First of all, high quality factors require an increased Nb thickness of 200 nm to accommodate higher current densities. Secondly, excellent insulation between the turns and layers of the coil, and the InAs

substrate is crucial. Parasitical capacitances should be avoided as well. During development, it proved impractical to prepare the complex Nb structures in the necessary precision using established lift-off processes. Imperfect lift-offs removed desired pieces of Nb and left stray bits of metal behind. Additionally, rough Nb tear-off edges interfered with the oxide layer. To improve the reliability of patterning, we switched to the inverse process of Nb dry etching. By simultaneously switching from positive to negative photo-lithography for the Nb patterning, we could continue to use existing designs and photo-masks with minimal adjustments. A reliable Nb patterning process combining dry etching and negative lithography was developed and implemented for this project, details are given in Appendix C. Unfortunately, the only available Nb etchant in our clean room, sulfur hexafluoride $SF_6$, is not sufficiently Nb/$SiO_2$ selective and etches the insulating oxide layer as well, with a comparable etching rate. This impairment is overcome by increasing the thickness of the insulator and carefully timing the etching. Prototype coils (Fig. 4.5) yielded encouraging results in rf measurements and showed the desired quality factors of $Q > 100$ at low voltages. Unfortunately, the quality factor rapidly decreases if the applied dc current exceeds 1.5 µA (Fig. 4.6), so the tank circuit is no longer in resonance and no measurements of the phase shift $\alpha(\varphi)$ are possible. A breakdown of insulation is presumed, as the known problem of irregular growth of PECVD-deposited $SiO_2$ on Nb edges (Chap. 2.2.1 and Kürsten (2002)) is aggravated by the non-selective etching process and multiplied by the high number of turns in the coils. While the PECVD-deposited $SiO_2$ is sufficient for gate insulation, a different insulator material is required for current-carrying applications. A possible workaround is to prepare the junction, interferometer loop and first layer of the coil with the proven InAs/Nb technology at the Institute of Applied Physics in Hamburg, but to fabricate the insulating layers and the rest of the coil with the alternative Nb/$SiO_1$ process available at the IPHT Jena. Alternatively, the on-chip coil could be used for $I_{\mathrm{rf}}$, which requires only low currents and proved possible with sufficient quality factors, while the major current component $I_{\mathrm{dc}}$ creating the external flux is fed to a separate, conventional coil. Unfortunately, these projects could not be carried through beyond the preliminary stages in the time frame of this thesis.

## 4.4. Results and Discussion

### 4.4.1. Current-Phase Relationship of Overlap Junctions

An overlap junction 1095-21 with optimized properties for CPR measurements (width $w = 1\,\mu\mathrm{m}$, electrode separation $a = 40\,\mathrm{nm}$) was prepared. Transport measurements at 1.8 K deliver $I_C = 3.8\,\mu\mathrm{A}$, $R_N = 58\,\Omega$, $I_C R_N = 220\,\mu\mathrm{V}$, and show subharmonic gap structures in the differential resistance of the junction. This indicates the high interface quality and transparency of the junctions even at electrode widths reduced to 1 µm. The junction is incorporated into a six-loop washer with an integrated flux transformer of

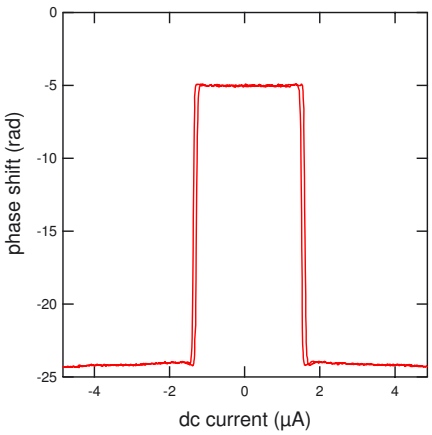


**Figure 4.6:** Recorded phase shift in the tank circuit when measuring the sample with the on-chip coil. At dc currents of $\approx 1.5\,\mu$A, the signal breaks down. This is probably the result of an insulation failure. The tank circuit then is no longer oscillating. Compare this graph to the regular measurement depicted in Fig. 4.7(a).

inductance $L = 17\,$pH as depicted in Fig. 4.4, and investigated at temperatures between 1.3 K and 6.0 K. The tank circuit's quality factor is $Q = 340$. Figure 4.7(a) shows the recorded phase shift $\alpha$ in the tank circuit as a function of the applied quasi-dc current $I_{\mathrm{dc}}$ creating the external flux $\Phi_e$. The period of this signal determines the coupling constant $k$. This signal is averaged for 20 periods to reduce noise before we use it to reconstruct the current-phase relationship pictured in Fig. 4.7(c). For decreasing temperatures, we observe a gradual deviation of the CPR from conventional sinusoidal behavior towards a saw-tooth curve. The position of maximum current shifts to $\varphi_{\max} = 0.626\pi$ at 1.3 K. At the same time, the critical current increases substantially, so that at some temperature the SQUID enters the hysteretic regime as $\beta f'(\varphi)$ approaches unity. In that case we are no longer able to reconstruct the CPR at lower temperatures. In this sample, the point was reached at 1.2 K, which is still well above our minimum temperature of 20 mK, so the values of inductance and critical current still leave room for improvement.

The temperature dependence of the critical current $I_C(T)$ was fitted by Tomáš Plecenik (Ebel et al., 2004) with the theoretical model described above, using the least squares method with the two fitting parameters electron density $n_s$ and interface parameter $\gamma_B$. The other parameters used in the calculation were determined independently as critical temperature $T_C = 6.5\,$K, width $w = 1.0\,\mu$m, electrode separation $a = 40\,$nm, barrier strength $Z = 0$, and Fermi velocity mismatch $\eta = 0.93$. The fitting procedure converges to the parameters $n_S = 3.75 \times 10^{12}\,\mathrm{cm}^{-2}$ and $\gamma_B = 2.4$. The calculated curve, included as solid line in Fig. 4.7(b), is in good agreement with the experimental data. The model also predicts a CPR (pictured as solid lines in Fig. 4.7(c)) in good agreement to the experimental data, when calculated with the same parameters determined from the $I_C(T)$ dependence. Only the curve measured at $T \approx 2.0\,$K

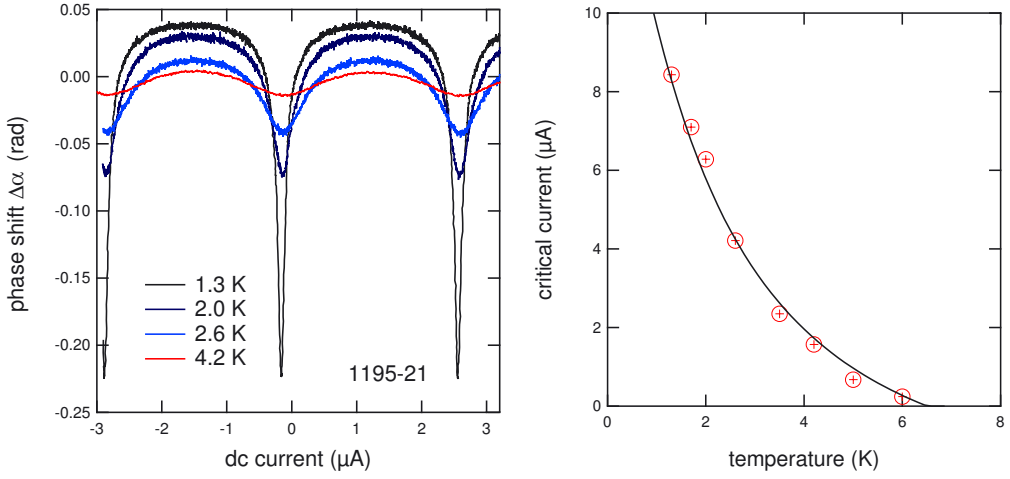


(a) (b)

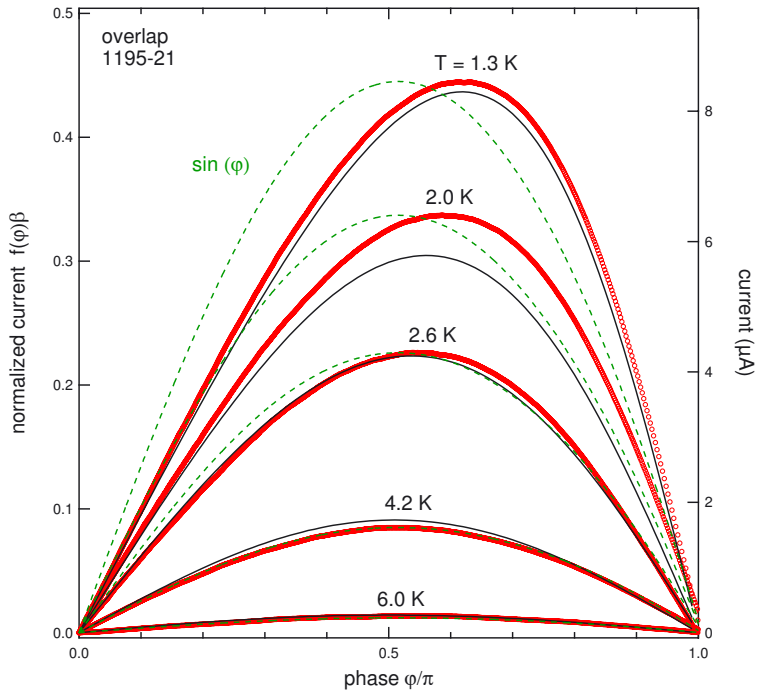


(c)

**Figure 4.7:** CPR measurements of overlap junction 1095-21. **(a)** Measured phase shifts at temperatures from 1.3 to 4.2 K. Increased signal amplitude and strong deviations from sinusoidal behavior are evident at low temperatures. This signal is averaged for 20 periods to reduce noise prior to evaluating. **(b)** Critical current in dependence of temperature. The solid line presents a fit using the Grajcar model. **(c)** CPR (circles) at temperatures between 1.3 K and 6.0 K, as reconstructed from the raw data as pictured in (a). The solid lines present a fit using the Grajcar model. For comparison, $\sin(\varphi)$ is drawn dashed.

deviates significantly from the calculated one. However, as the temperature dependence of $I_C(T)$ is rather steep at low temperatures, a small difference between the temperature of the thermometer and the sample could be responsible for this difference. With the parameters given above we calculate the junction resistance of $R_N = 83\,\Omega$. Transport measurements yielded a slightly lower $R_N = 58\,\Omega$, but as we measure a parallel connection between substrate and junction, a lower collective resistance is to be expected. A realistic substrate resistance of $\approx 180\,\Omega$ would fit the measured value $58\,\Omega$. The interface parameters indicate a highly transparent junction. The assumed carrier density is about three times as large as the result from Shubnikov-de Haas measurements $n_S = 1.2 \times 10^{12}\,\mathrm{cm}^{-2}$ on comparable samples (Milde, 2000). Nevertheless, the higher value of $n_S$ produced by the model is consistent with the small value of $R_{Nexp}$ from transport measurements. Note that $R_N$ lies below the Sharvin resistance $R_{\mathrm{Sh}} \approx 150\,\Omega$ calculated for an ideal junction of $w = 1.0\,\mu\mathrm{m}$ width and typical carrier density $n_S = 1.2 \times 10^{12}\,\mathrm{cm}^{-2}$ with Eq. 3.1, so that either $n_S$ is much higher, or the effective junction width $w$ is wider than the physical electrode width due to bypass currents.

### 4.4.2. Current-Phase Relationship of Josephson Field-Effect Transistors

The reconstructed current-phase relationship of the bulk JoFET 1091-53 (width $w = 20\,\mu\mathrm{m}$, electrode separation $a = 120\,\mathrm{nm}$, with a square washer of $L = 80\,\mathrm{pH}$) is shown in Fig. 4.8(a) at different temperatures between 2.75 K and 3.75 K. A gradual deviation from sinusoidal behavior with decreasing temperature is clearly seen along with increasing critical current, corresponding to theoretical expectations. The position of maximum current is shifted to $\varphi_{\max} = 0.557\pi$ at 2.75 K. We have also determined the influence of an external gate voltage on the CPR of bulk JoFET 1091-51[2], pictured in Fig. 4.8(c). In spite of sacrificing the advantage of a measurement technique without galvanic leads by introducing a gate electrode, we were able to obtain the SQUID signal with only a small deterioration. The critical current can be enhanced or reduced by gate voltage. However, no significant change in the CPR shape is visible. The small shift of the CPR maximum towards zero ($\varphi_{\max} = 0.481\pi$) is caused by external noise introduced by the gate leads, as predicted in Chap. 4.2.2. The samples used for this experiment had relatively low transparencies, so the expected deviations from a harmonic CPR at temperatures above 2 K are small. Measurements below 2.5 K were not possible as the SQUIDs entered the hysteretic regime. To make lower temperatures accessible, an additional sample 1093-J9 with reduced electrode width $w = 1.4\,\mu\mathrm{m}$,

[2] Unfortunately, the gate electrode on the sample 1091-53 (showing the deviations at low temperature) was defective, requiring us to use an alternative sample (from the same wafer and processed identically) for the gate-dependent measurements. This sample 1091-51 did not show any significant deviations even without a gate contact in the accessible temperature range ($T > 2.5$ K).

$a = 170\,\text{nm}$, and a $30 \times 30\,\mu\text{m}^2$ square washer of $L = 40\,\text{pH}$ was prepared. Its reduced critical current allowed measurements down to 20 mK (Fig. 4.9). $I_C$ increases for decreasing temperature even below 500 mK. This complies with the predictions of Kulik and Omel'yanchuk for highly transparent junctions, whereas the dirty-limit case or tunnel theory (Golubov et al., 2004) predict saturation for $T < 0.2T_C \approx 1.6\,\text{K}$. The position of the maximum shifts to $\varphi_{\max} = 0.543\pi$ at 20 mK, but is still at $\varphi_{\max} = \pi/2$ ($0.498\pi$) at 1.0 K. This late onset of CPR deformation compared to the other samples is surprising considering the high junction transparency suggested by the temperature dependence of $I_C$ or transport measurements on comparable junctions. This could point to a sample-specific impairment, which is also indicated by the low critical current compared to the related sample 1193-J5 described in Chap. 3.2. Also pictured in Fig. 4.9 is the CPR of a Nb/$Al_2O_3$/Nb tunnel junction used for comparison, as it should exhibit a purely sinusoidal CPR. It was measured at 20 mK in the same setup on the same day, the maximum was recorded at $\varphi_{\max} = 0.484\pi$. This small shift from $\pi/2$ indicates the magnitude of noise effects described in Chap. 4.2.2.

The results of the temperature-dependent CPR measurements can be fitted well with the Grajcar model. Fitting the temperature-dependence of the critical current (as pictured in Fig. 4.8(b)) yields parameters of $\gamma_B = 0.25$ and $n_S = 0.25 \times 10^{12}\,\text{cm}^{-2}$, calculated with $T_C = 5.5\,\text{K}$ and $w = 20\,\mu\text{m}$. The same parameters are then used to calculate the CPR as pictured by the solid lines in Fig. 4.8(a). The agreement between experimental and theoretical data is not quite as good as in the case of overlap junction 1095-21 presented in the previous section. The predicted carrier density $n_S$ is one order of magnitude lower, although all samples come from the same batch of nominally identical wafers. The best fit results from assuming a low number of conductance channels $N = 85$ with relatively high individual transparencies. Evaluation based on geometry and the transport results predict a much higher number of conductance channels, but with a reduced average transparency. If the results of transport measurements are fed into the model, a higher critical current is predicted. It is not fully understood why and how this discrepancy arises. It occurs in the JoFET samples with lower transparency and increased channel length compared to the highly transparent overlapping sample 1095-21, so it could be caused by impaired interfaces or by processes in the channel. In the fit $Z = 0$ is assumed. This is problematic for junctions of low transparency. It should be noted that a much lower critical current than predicted by theory has been found by most groups working on ballistic SNS junctions (see Heida et al. (1999) and references 12-20 therein), while the cause is under debate (Bastian, 2000).

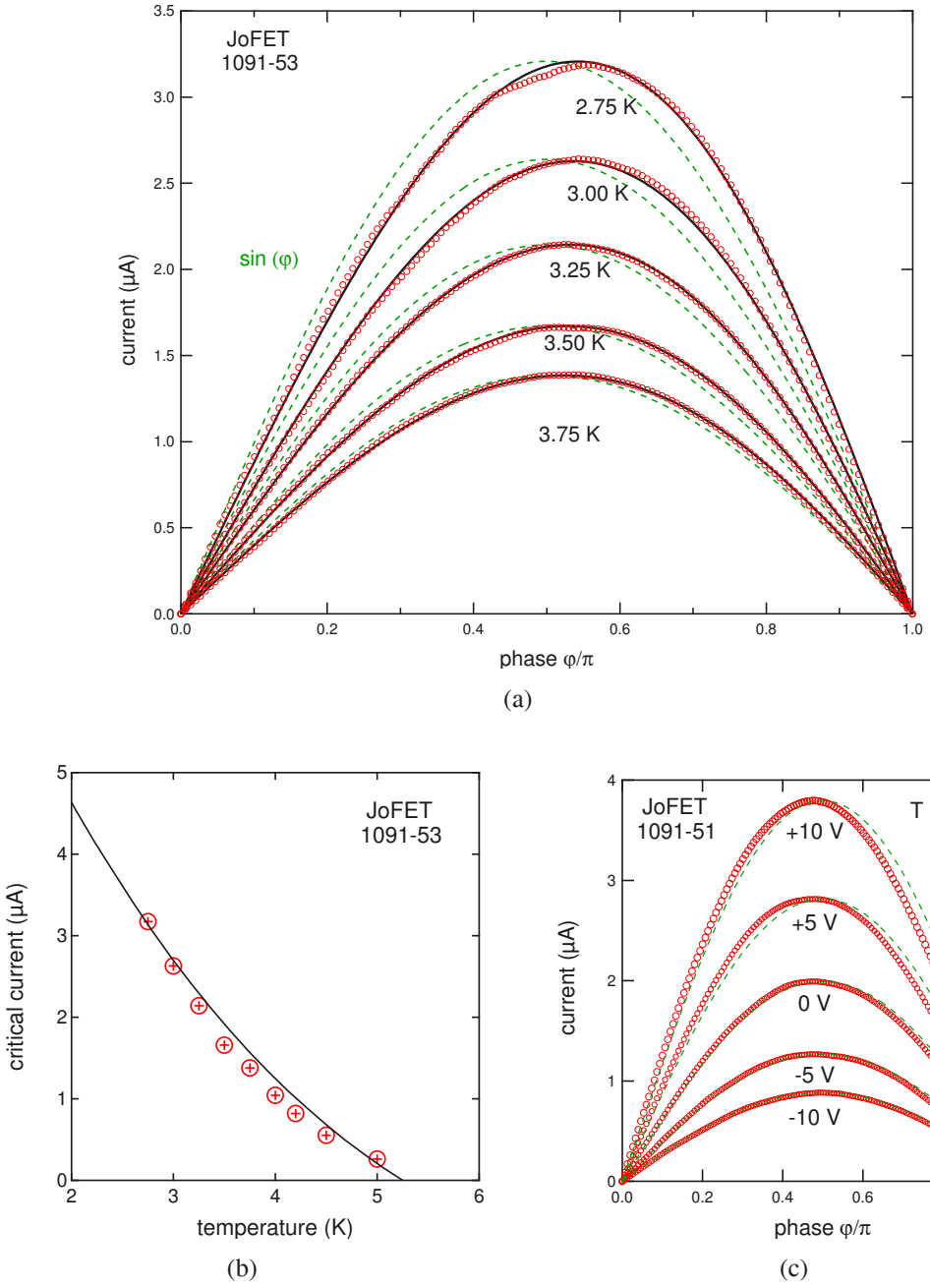


**Figure 4.8:** **(a)** CPR of bulk JoFET 1091-53 in dependence of temperature (circles). Solid lines depict the fit of the Grajcar model, $\sin(\varphi)$ of comparable amplitude is drawn dashed. **(b)** Corresponding critical currents in dependence of temperature, from the same measurement as depicted in (a), with the Grajcar fit included. **(c)** Gate-voltage dependence of CPR in JoFET 1091-51. The amplitude of the CPR can be controlled in a wide range by a gate electrode. The small shift of the maximum towards zero is caused by noise introduced by the gate electrode.

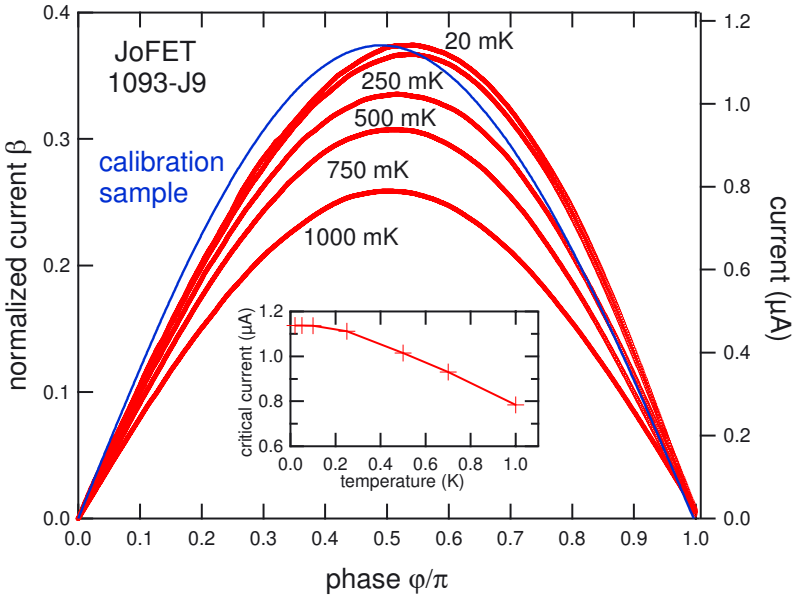


**Figure 4.9:** CPRs at low temperatures of bulk JoFET 1093-J9 (circles) and a $Nb/Al_2O_3/Nb$ tunnel junction (solid line) used for calibration. $\sin(\varphi)$ is indistinguishable from the calibration sample at this resolution. The inset shows the temperature dependence of the critical current. Saturation is visible only below 200 mK.

# 5. Summary and Conclusion

This work presents an experimental investigation of the current-phase relationship of Nb/InAs(2DES)/Nb Josephson junctions. A sputter deposition system had to be modified and optimized to yield Nb films with critical temperatures near the bulk limit and high quality Josephson junctions, both on bulk InAs and on InAs high electron-mobility transistor (HEMT) heterostructure substrates. Two distinct Nb/InAs(2DES)/Nb Josephson junction designs on bulk InAs were realized to measure the current-phase relationship, namely overlap junction and Josephson field-effect transistors (JoFET). Both types were miniaturized to junction widths of $w = 1\,\mu\text{m}$, yielding samples with highly transparent interfaces and critical currents suitable for mesoscopic applications. A significant influence of bypass currents was observed in these devices.

Josephson field-effect transistor fabrication technology was transferred to InAs HEMT substrates. In these devices, the critical current of JoFETs could be controlled in a wide range by tuning the electron density of the 2DES via gate voltage. Two etching techniques were employed to successfully build superconducting JoFETs on HEMTs, with the reactive-ion etching (RIE) method yielding superior results. An important advantage of HEMT over bulk substrates is the ability to avoid bypass currents by confining the 2DES. Therefore, further miniaturization to widths below 1 µm should be performed using HEMT substrates.

To investigate the current-phase relationship, samples with optimized designs were fabricated on bulk InAs. We explored experimentally the current-phase relationship of two Nb/InAs(2DES)/Nb Josephson junction types, namely overlap junctions and JoFETs, and supplemented these results with transport measurements. Overlap junctions, measured from 1.3 K to 6.0 K, showed substantial deviations from a conventional sinusoidal towards a saw-tooth form with decreasing temperatures. JoFETs were investigated in dependence of temperature from 20 mK to 5.0 K and gate voltage. In these devices we also observed significant deviations from a sinusoidal behavior towards a saw-tooth shape at low temperatures. The current-phase relationship of a JoFET junction was controlled by a gate electrode in a wide range without considerable deterioration of the rf signal in spite of additional noise. Transport measurements support the results gained by phase sensitive measurements.

Our results prove for the first time deviations from a sinusoidal current-phase relationship in Nb/InAs(2DES)/Nb Josephson junctions. The findings are in good qualitative agreement with predictions of theories for highly transparent superconductor/normal conductor/superconductor junctions.

The Josephson junctions investigated in this work present very promising systems for basic research on the mechanism of superconductivity. For technical applications, the properties of the JoFETs suggest integration in superconducting electronics, either conventional digital or quantum based. Their advantage of tunability could either open new possibilities or simplify preparation, e.g. compared with designs for tunable junctions proposed by Makhlin et al. (1999)[1]. But to compete with established $Nb/Al/Al_2O_3$ tunnel junction technology beyond a few niches, the problems of unreliable lift-off processes and insulation and the significant parameter spread of nominally identical samples must be overcome, as these problems impede the construction of devices of higher complexity with the currently available technology. As an added benefit, the radio-frequency measurement technique is a very promising candidate for the read-out of qubits (Il'ichev et al., 2004). Il'ichev et al. (2003) have used it to detect Rabi oscillations in a flux qubit comprised of three Josephson junctions.

[1] The Makhlin et al. (1999) approach replaces a non-tunable Josephson junction with two parallel junctions in a loop. This creates a dc SQUID, which can be tuned by applying magnetic flux.

# Appendices

# A. Niobium Sputter Deposition System

For the preparation of SNS junctions a Niobium (Nb) sputter deposition system is crucial. While most of the machines and techniques used in the preparation of our Nb/InAs(2DES)/Nb Josephson junctions are commercially available and are widely used in the semiconductor industry, the sputter deposition system, as pictured in Fig. A.1, is a custom-built machine and has been optimized and modified during the course of this project. A detailed account of its properties, setup and basic optimization is given in Ebel (2000), a related system was built and optimized by Pels (2003). More on the principles of sputter systems can be found in standard text books such as Rossnagel (1998). For a thorough evaluation of Nb deposition parameters, see May (1998).

## A.1. Basic Operation

A sputter system works by ionizing an inert gas such as Ar to a plasma and accelerating the ions towards a target surface via electrical fields. These projectiles eject target atoms on impact, but note that no chemical reactions occur in this mechanical process. The target surface is eroded, the ejected atoms resettle on other surfaces. Our system utilizes both of these aspects in a three-step process. At the start, the Nb target is etched to expose a fresh, uncontaminated surface. The ejected Nb atoms coat the surfaces of the sputter chamber and improve the process atmosphere by gettering unwanted reactive residual gases such as oxygen. The sample and other sensitive areas are protected by elaborate baffle systems during this process step. In the second step, the sample is uncovered and its surface etched to remove oxidized material and other possible contaminants and so to assure clean interfaces and good adhesion. It is also possible to prolong this step to achieve arbitrary etch depths, which is important in handling heterostructure substrates (see Chap. 2.2.2). Finally, the cleaned Nb target is sputtered again to coat the sample with a Nb film of desired thickness. These steps are performed in sequence without moving the sample or changing the process gas. For the sputtering of Nb moderate-power dc magnetron sputtering is used, whereas the sample is etched by a low-energy rf plasma.

(a)

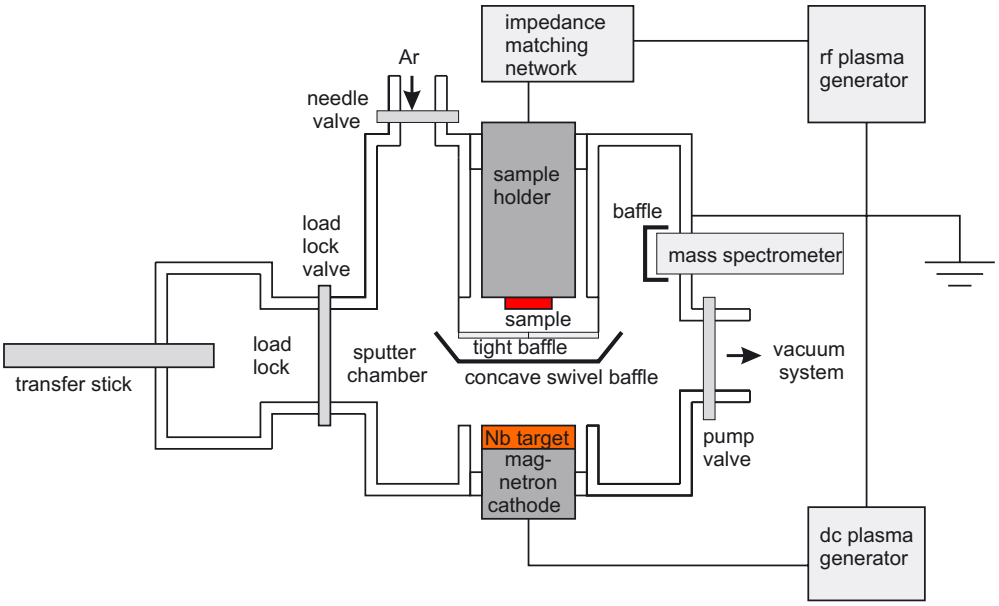


(b)

**Figure A.1:** **(a)** Photograph of the Nb sputter deposition system. **(b)** Schematic of the system.

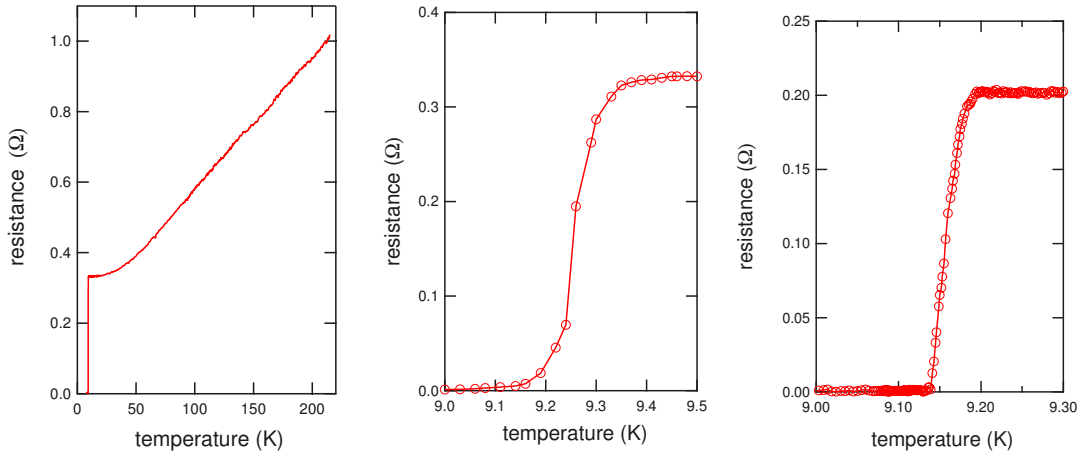


**Figure A.2:** **(a)** Resistance measurement $R(T)$ of a 100 nm thin Nb layer on a semi-insulating Si substrate. **(b)** Close-up of the transition area. A critical temperature comparable to the bulk limit of 9.2 K is visible. **(c)** Another sample was measured in a special set-up optimized for temperature stability and high resolution. The transition into the superconducting state occurs in less than 40 mK, which is comparable to the resolution of the standard set-up.

## A.2. Optimization of Niobium Films

To fabricate high-quality Josephson junctions, we aim at Nb in the form of polycrystalline thin films with excellent superconducting properties. The quality of the Nb films depends on deposition parameters and is evaluated by measuring the dependence of film resistance on the temperature $R(T)$ in a conventional four-point-probe setup (see Fig. A.2 for examples and Chap. 3.1 for details of the measurements). The test films are deposited on semi-insulating Si wafers with low doping instead of InAs to avoid bypass currents through the substrate. The main indicator of film quality is the critical temperature $T_C$, but there are two further established indicators of quality besides $T_C$: a high residual resistance ratio $R_{300K}/R_{10K}$ indicates few defects in the film. Whereas electrical resistance $R$ at 300 K is mainly caused by phonon scattering and drops linearly with temperature, the curve reaches a plateau at some residual level (see Fig. A.2(a)). This residual resistance, arbitrarily defined as $R(10\,\mathrm{K})$, is mainly caused by scattering of conduction electrons at grain boundaries, dirt or other defects; thus the ratio can be used as a measure of film quality. Secondly, the width of the jump $\Delta T_C$ is evaluated. A sharp transition into the superconducting state indicates a homogeneous film. Unfortunately, the transition is quite rapid compared to the resolution of our equipment. Figure A.2(b) depicts a measurement in the standard set-up, while the sample in Fig. A.2(c) was measured in a special set-up optimized for temperature stability and high resolu-

tion[1]. This set-up, combined with extremely slow temperature changes, helps to avoid temperature differences between sensor and sample or intra-sample differences. The transition into the superconducting state occurs in less than 40 mK. As the sample in Fig. A.2(b) exhibited a higher $T_C$, a sharper transition would be expected, but could not be resolved in the standard set-up. Because of these difficulties, the indicator $\Delta T_C$ is of secondary relevance only.

The typical thickness of 100 nm gives electronic properties of the films near the bulk limit. They are not dominated by surface effects. This corresponds to results published by Wolf et al. (1975), where no significant deviations from bulk properties were found for sputtered Nb film of more than 80 nm thickness. Nb films with a reduced thickness of 50 nm (comparable to the coherence length) were also prepared and still exhibit critical temperatures of $\approx 90$ % of the bulk value. Some slight variation in film thickness therefore is deemed uncritical.

As shown in Chap. 2.2.1, the lift-off process used to pattern Nb microstructures is a critical preparation step. To improve the success chances, tensions in the deposited film can be exploited. Films sputtered at 1.5 Pa show accelerated lift-off times compared to films sputtered at higher or lower pressures. According to Kuroda and Yoda (1987), sputter deposition at 1.0 Pa yields unstressed films, whereas maximum tensile stress is expected for about 1.6 Pa (see Fig. A.3(a)). Tensile stress can facilitate lift-off, if the device characteristics do not suffer. The critical temperature of Nb films does not decrease at deposition pressures below 2 Pa, in accordance with the results of Kuroda and Yoda (1987). Elevated process pressures of 1.5 Pa are used chiefly for Nb structures without semiconductor interfaces, e.g. to prepare the complex flux transformers shown in Fig. 4.4 on page 39, where a clean lift-off proved problematic at standard parameters. Clear separation and smooth tear-off edges were achieved at 1.5 Pa. Smooth edges are relevant if further layers are to be added on top, e.g. oxides and gate electrodes. Often, protruding tear-off edges are encountered after lift-off processing, leading to weak spots in the oxide layers deposited on top and thus to potential short cuts. Recommended Nb deposition parameters are 120 s dc plasma at 150 W power and either 1.0 Pa Ar pressure for optimal InAs interfaces or 1.5 Pa for enhanced lift-off, both giving Nb films of about 100 nm thickness.

Note that we are constrained in the range of deposition parameters by the substrate material. It is well known that substrate temperature has significant influence on grain size in sputtered films, and epitactic films require recrystallization at temperatures comparable to the melting point of the sputtered material. However, InAs will decompose at temperatures of more than 200°C, forcing us to deposit at temperatures far below the melting point of Nb (2500°C). Sürgers et al. (1994) reported on the substrate temperature dependence of Nb film growth and predict for our conditions film growth by ballistic aggregation. The resulting small grain sizes are the main cause for the relatively low resistance ratio $R_{300K}/R_{10K} \approx 5$ of our samples. However, these conditions

[1] The main difference is the use of a closed sample stick instead of a gas-flow cryostat.

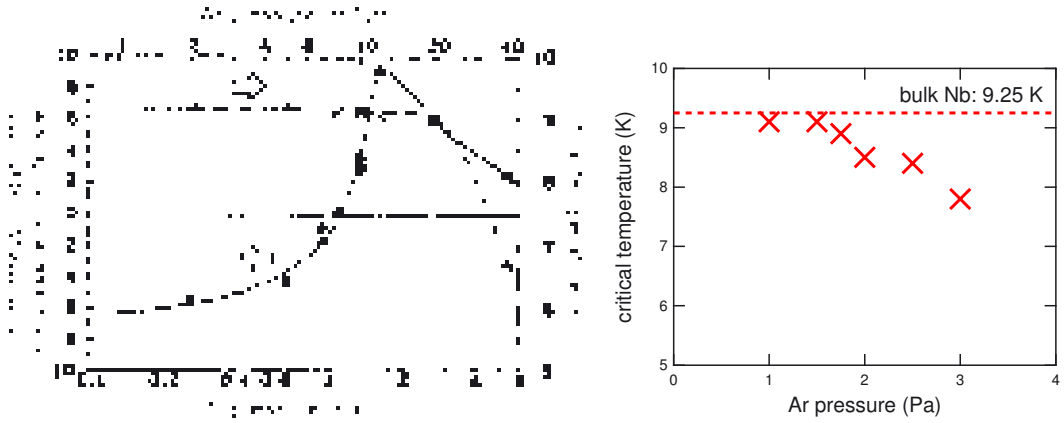


(a) (b)

**Figure A.3: (a)** Pressure dependence of stress (dots) and critical temperatures (crosses) for 100 nm sputter deposited Nb films. Taken from Kuroda and Yoda (1987). **(b)** Dependence of the critical temperatures of 100 nm thin Nb layers sputtered in our system on Ar pressure. The values are in good agreement with Kuroda's results.

do not handicap the superconducting properties of our Nb films significantly, as our critical temperatures are exceeded by Sürgers' samples only for deposition temperatures of $> 600°$ C.

## A.3. Modifications for Optimized Josephson Junctions

The Nb sputter deposition system used in this work was designed as successor to another custom-built system at our institute, described by Matsuyama (1994). After the optimization detailed in Ebel (2000), the quality of Nb films from the new system was better than from the old system, but the SNS interface transparency in bulk InAs samples was not quite as good despite the better vacuum characteristics. The transparency is determined chiefly by the rf etching of the sample before the Nb deposition. The main difference between the systems was the location of the rf plasma. Whereas in the old system the rf plasma was confined to a small volume between the sample and a concave baffle, in the new system there was no such baffle and the rf plasma spread through the sputter chamber. Presumably, the interface thus was contaminated by unintended sputtering. Therefore a swiveling concave baffle was retrofitted to the new system, as sketched in Fig. A.1(b). After this modification, sample quality is superior to the old system, while the Nb quality is not affected. Sputter parameters are unchanged: 8 min of rf plasma at 4 W power and 1.0 Pa Ar pressure are recommended as process parameters for the bulk InAs etch process, giving an etch depth of 30 nm. Further modifications

improved the vacuum system and the usability of the device, but had no direct influence on sample preparation.

## A.4. Cathode Corrosion

By keeping a detailed log of the sputter processes, a creeping drift in plasma parameters during Nb deposition was noted. The dc plasma currents decreased, requiring higher voltages to keep the sputtering power constant, but not resulting in decreased Nb quality for some months. A weakening of the magnetic field confining the plasma was suspected as cause. The plasma generator has a voltage limit of 800 V, which was reached eventually. To provide continued operations during the process of troubleshooting and consultating with the electrode manufacturer regarding this strange behavior (Angstrom Sciences, 2003), voltage was lowered by increasing the Ar process pressure. It is also possible to reduce voltage by reducing the plasma power, but this is unfavorable as it extends sputter time and so the duration of possible contamination of the deposited Nb film by residual gases. Figure A.3(b) shows measurements of layers prepared during this period. Nb layers of reasonable quality with $T_C > 8\,\mathrm{K}$ could be deposited even under these impaired conditions at pressures of up to 3 Pa, until a suspected vacuum leak drastically worsened sputter performance and required immediate action. Residual gas analysis via a mass spectrometer showed high water concentration in the sputter chamber, while nitrogen was elevated, but not as high as expected for a leak. Helium leak testing showed no leak between the sputter chamber and the outer surface of the system, but an influence between residual pressure and cathode cooling water pressure was noticed.

Disassembly of the sputter magnetron cathode (Model Onyx-3UHV, manufactured by Angstrom Sciences) confirmed our suspicions. In spite of following the manufacturer's recommendations for operation, the cooling water had eroded the NdFeB permanent magnets (Fig. A.4(a)) and corroded the casing at a copper-steel interface, resulting in a leaking vacuum seal. We managed to clean the cathode assembly and to seal the leak by hard soldering. As the magnets were replaced, we noticed that the manufacturer has switched to a different capsule material. To avoid problems in the future, the magnets were sealed with additional anti-corrosion varnish. Additionally, the operating instructions for the sputter system were changed to ensure cooling water is no longer running continuously, but only during sputtering and bake-out. This modified system has worked flawlessly and with constant plasma parameters for a year now.

(a) (b)

**Figure A.4: (a)** Corroded magnetron cathode after opening. Residues of the circular inner NdFeB permanent magnet and its capsule material are visible at the center. The outer ring magnet has disintegrated and could not be removed in one piece. **(b)** Same magnet assembly after cleaning and fitting with new magnets. The magnets are encapsulated with additional anti-corrosion varnish.

# B. List of Publications

Parts of this work have been published previously. The papers A, B and C are included in this section.

## B.1. Conference Contributions

- Talk, *Gate-voltage and temperature dependence of the current-phase relation in Nb/2DES/Nb Josephson junctions on p-type InAs*, Tagung Kryoelektronische Bauelemente KRYO 2000, Pommersfelden/Germany
- Talk TT 4.9, *Gate-voltage and temperature-dependence of the current-phase relation in Nb/2DES/Nb Josephson junctions on p-Type InAs*, DPG Frühjahrstagung 2001, Hamburg/Germany
- Talk, *Gate-voltage and temperature-dependence of the current-phase relation in Nb/2DES/Nb Josephson junctions on p-Type InAs*, Tagung Kryoelektronische Bauelemente KRYO 2001, Kerkrade/Netherlands
- Poster TT 7.13, *Nb/InAs(2DEG)/Nb Josephson Kontakte*, DPG Frühjahrstagung 2002, Regensburg/Germany
- Poster TT 14.19, *Strom-Phasen-Beziehung in Nb/InAs(2DEG)/Nb Josephson-Kontakten*, DPG Frühjahrstagung 2003, Dresden/Germany
- Invited talk, *Supercurrent-phase Relationship of the Nb/InAs(2DEG)/Nb Josephson Junction*, ESF PiShift Workshop 2003, June 16-19, Jena/Germany
- Poster, *Supercurrent-phase Relationship of the Nb/InAs(2DES)/Nb Josephson Junction*, European Conference on Applied Superconductivity EUCAS 2003, September 14-18, Sorrento/Italy

## B.2. Paper A

M. Grajcar, M. Ebel, E. Il'ichev, T. Matsuyama, and U. Merkt,
*Supercurrent-phase Relationship of a Nb/InAs(2DEG)/Nb Josephson Junction. Temperature and Gate-voltage Dependence*,
Physica C, **372** (2002), 27-30.

Physica C 372–376 (2002) 27–30

PHYSICA

www.elsevier.com/locate/physc

# Supercurrent–phase relation of a Nb/InAs(2DEG)/Nb Josephson junction

M. Grajcar [a,c,*], M. Ebel [b], E. Il'ichev [a], R. Kürsten [b], T. Matsuyama [b], U. Merkt [b]

[a] *Department of Cryoelectronics, Institute for Physical High Technology, P.O. Box 100239, D-07702 Jena, Germany*
[b] *Universität Hamburg, Institut für Angewandte Physik und Zentrum für Mikrostrukturforschung, Jungiusstraße 11, D-20355 Hamburg, Germany*
[c] *Department of Solid State Physics, Comenius University, Mlynská Dolina F2, 842 48 Bratislava, Slovakia*

**Abstract**

Using an RF-SQUID configuration we have measured the temperature dependence of the current–phase relation (CPR) of Nb/InAs(2DEG)/Nb (two-dimensional electron gas, 2DEG) Josephson junctions with high interface transparency. At low temperatures, significant deviations from a sinusoidal CPR are observed. The experimental results are fitted by the scattering matrix theory of Brouwer and Beenakker, additionally taking into account the proximity effect between the Nb and the 2DEG in the inversion layer on p-type bulk InAs. We have studied also the influence of an external gate voltage applied to the InAs(2DEG) channel. It is shown that the amplitude of RF-SQUID oscillations can be controlled by gate voltage with only modest deterioration of the SQUID signal.


*PACS:* 74.50.+r; 74.80.Fp; 74.72.–h
*Keywords:* Josephson junction; Proximity effect; 2DEG

Highly transparent Josephson weak links are of considerable academic and practical interest [1]. For charge transfer through small-size junctions higher order processes lead to the presence of higher order harmonics in the current–phase relation (CPR) [2]. The precise knowledge of the dependence of the CPR on temperature and junction properties helps to improve our understanding of the mechanisms of charge transfer in weak links. For our present investigations we use a Josephson field-effect transistor [3]. It allows us to control the critical current and transparency of the junction, changing its behavior from quasi-ballistic to tunnel-like. This should result in significant changes in the CPR.

In our samples two Nb electrodes are coupled by the two-dimensional electron gas (2DEG) that forms in the native inversion layer at the surface of p-type bulk InAs [1]. The electron density and

* Corresponding author. Address: Department of Solid State Physics, Comenius University, Mlynská Dolina F2, 842 48 Bratislava, Slovakia. Tel.: +421-2-6029-5528; fax: +421-2-6541-2305.
*E-mail address:* grajcar@fmph.uniba.sk (M. Grajcar).

0921-4534/02/$ - see front matter 
PII: S0921-4534(02)00695-0

Fermi velocity of the 2DEG in the channel can be adjusted via field effect using a gate electrode. At a typical electron density of $n_s = 1.2 \times 10^{12}$ cm$^{-2}$ and mobility of $\mu \approx 10^4$ cm$^2$/V s, the mean free path of 240 nm is longer than the channel length. From the dependence of the critical current on the channel length, we estimate the coherence length $\xi_N \approx 145$ nm at 1.8 K. Thus we have a quasi-ballistic superconducting weak link with the Josephson junction being in between the short and the long limit.

Our electrodes are defined by electron-beam lithography. The InAs surface is cleaned in situ using low-energy Ar etching prior to the deposition of a 100 nm thick Nb film by magnetron sputtering, yielding highly transparent interfaces. The channel is $L = 120$ nm long, the electrodes are $w = 20$ μm wide. They are connected by a SQUID washer of 80 pH inductance. A thermally evaporated Al gate electrode is deposited on top of a 340 nm thick $SiO_2$ insulating layer (Fig. 1).

The CPR is determined by a modified Rifkin–Deaver method [8]. The junction to be investigated is incorporated into an RF-SQUID, which is coupled inductively to a high quality tank circuit in resonance. The phase of the junction can be biased by external flux. Changes in the impedance of the coupled system are measured and can be used to reconstruct the CPR. Further details are given elsewhere [9].

To fit the experimental data we use the scattering matrix formalism for Josephson currents [4,5] which can be written as a sum over the transverse modes $n$

$$\frac{eIR_0}{\pi k_B T_c} = \frac{16T}{T_c} \sum_{n=0}^{N-1} \sum_{m=0}^{\infty} \frac{-a^2 |S_{12}|^2 \sin(\varphi)}{1 - 2a^2(|S_{12}|^2 \cos(\varphi) + |S_{11}|^2) + a^4 |S_{11}^2 + S_{12}^2|^2}, \quad (1)$$

where $R_0 = h/e^2$ is the resistance quantum; $a$, the coefficient of the Andreev reflection at the InAs-(2DEG)/InAs interface and $S_{ij}$, the elements of the scattering matrix for normal reflection in a symmetric double barrier junction $S_{11} = |r| + |r||t|^2 p_n^2/(1 + |r|^2 p_n^2)$, $S_{12} = |t|^2 p_n/(1 + |r|^2 p_n^2)$. Here $|r|^2$, $|t|^2$ are the reflection and transmission probabilities of the left- and right-hand barrier, $p_n = \exp(ik_{Fn}L - \omega_m L/\hbar v_{Fn})$, where $\omega_m = (2m + 1)\pi k_B T$ are Matsubara frequencies, $k_{Fn}$ and $v_{Fn}$ are components normal to the barriers of the wave vector and Fermi velocity, respectively, of the $n$th transverse mode to the barriers and $L$ is distance between them. Following the BTK approach [6,7], the reflection and transmission coefficients can be written in the form

$$|t|^2 = 1 - |r|^2 = \frac{(1 - (n/N)^2)}{(1 - (n/N^2))(\eta + 1)^2/4\eta + Z^2} \quad (2)$$

where $Z$ is dimensionless potential barrier strength and $\eta = v_{Fs}/v_{Fn}$ is the Fermi velocity mismatch.

In order to calculate the Josephson current from Eq. (1), one must determine the Andreev reflection coefficient $a$ for the InAs(2DEG)/InAs interface. Since superconductivity is induced in InAs by the proximity effect coefficient, it may be written as [10] $a = iF/(1 + G)$, where $F$ and $G$ are Green's functions in the inversion layer of InAs. Due to low electron density of the inversion layer the suppression of the pair potential in Nb can be neglected [1] and $F$, $G$ can be expressed by McMillan equations [11] $G = \omega/(\omega^2 + \Phi^2)^{1/2}$, $F = \Phi/(\omega^2 + \Phi^2)^{1/2}$, and $\Phi = \Delta/(1 + \gamma_B(\omega^2 + \Delta^2)^{1/2}/\pi k_B T_c)$, where $\gamma_B$ is a dimensionless parameter characterizing the transparency between Nb and InAs, $\Delta$ is the superconducting energy gap of bulk Nb, and $T_c$ its critical temperature.

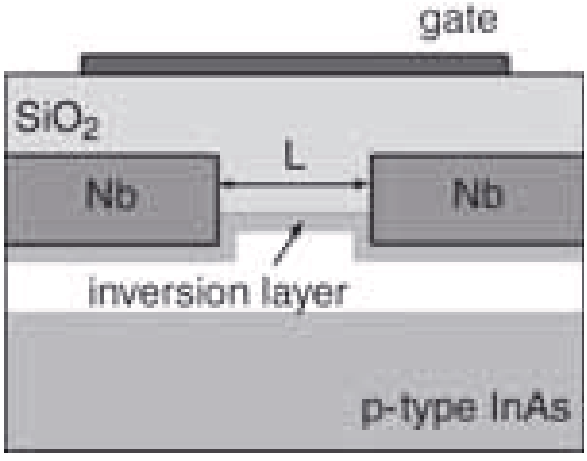


Fig. 1. Schematic cross-section of the Josephson junction.

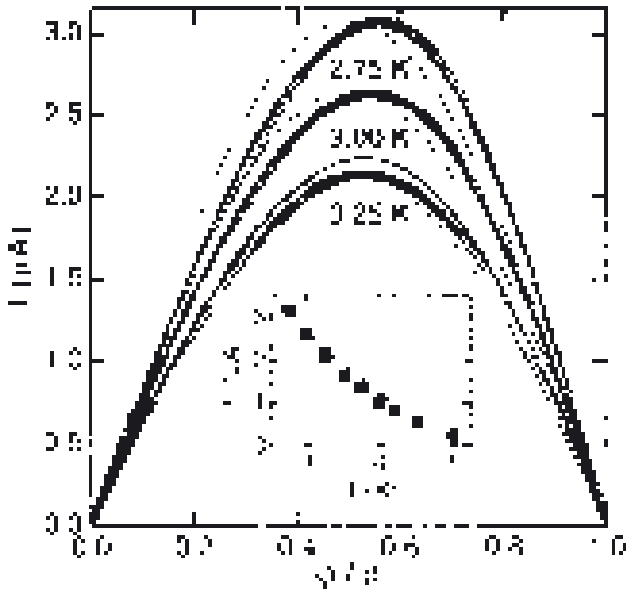

Fig. 2. Comparison of the experimental and theoretical CPR $I(\varphi)$ for various temperatures. Open circles are experimental data. Solid lines are calculated according to the model described in the text, dashed lines show appropriate sinusoidal CPR. Inset: temperature dependence of the critical current.

Experimental CPR and corresponding results of the fitting procedure are shown in Fig. 2. A gradual deviation from sinusoidal behavior with decreasing temperature is clearly seen. Both the CPR and the temperature dependence of Josephson critical current were calculated as stated above. Parameters $v_{Fn}$, $k_{Fn}$, $\eta$ were derived from electron density $n_s$ in the $N$ channel where $n_s$ is taken as fitting parameter. Good agreement between experimental and theoretical data is obtained for fitting parameters $\gamma_B = 0.6$, $n_s = 0.8 \times 10^{12}$ cm$^{-2}$ and $T_c = 5.25$ K, $N = 82$. However, the number of modes $N$ calculated from the width of the junction is more than one order of magnitude higher. Additionally, subharmonic gap structures are still visible above this value of $T_c$.

Hence, the presented model captures the essential qualitative aspects of the CPR, quantitatively further improvements clearly are needed.

We should point out that in order to evaluate $I(\varphi)$, the RF-SQUID is required to be in non-hysteretic mode, i.e. for a SQUID washer of an inductance 80 pH the current has to be smaller than 4 μA. Usually the critical current of the Nb/InAs(2DEG)/Nb Josephson junctions exceeds this value considerably. Thus we have measured Josephson junctions with reduced critical current and lower interface transparency. Nevertheless we have observed a deviation of the maximum of the CPR towards $\pi$. The investigation of the CPR of junctions with higher critical current requires more sophisticated technology. Corresponding work is in progress.

We have also determined the influence of an external gate voltage. After electronic filtering at low temperature we were able to obtain the SQUID signal without a considerable deterioration. The results are shown in Fig. 3. The small shift of the CPR maximum form $\pi/2$ towards zero is caused by external noise introduced by the gate leads [12].

To conclude, the properties of Nb/InAs-(2DEG)/Nb Josephson junctions studied by phase sensitive measurements are in qualitative agreement with theoretical results obtained by the scattering matrix method, taking into account a proximity effect between Nb and the inversion layer on InAs. By controlling the electron density of the 2DEG via gate voltage it is possible to change the critical current of the Josephson junction in a wide range without considerable deterioration of the RF-SQUID signal. This presents an

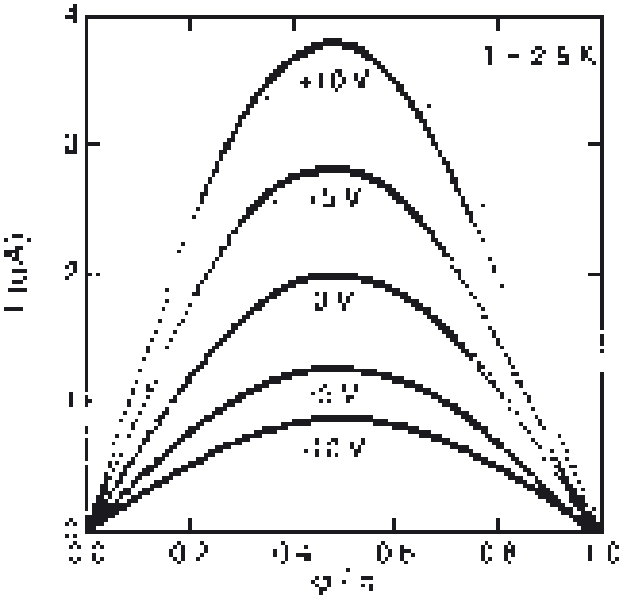

Fig. 3. CPRs for various gate voltages at $T = 2.5$ K. Dashed lines show sinusoidal CPR.

opportunity to use Nb/InAs(2DEG)/Nb Josephson junctions in very sensitive magnetometers.

## Acknowledgements

We thank the Deutsche Forschungsgemeinschaft for financial support via the SFB 508 "Quantenmaterialien".

## References

[1] A. Chrestin, T. Matsuyama, U. Merkt, Phys. Rev. B 55 (1997) 8457.
[2] K.K. Likharev, Rev. Mod. Phys. 51 (1979) 101.
[3] H. Takayanagi, T. Kawakami, Phys. Rev. Lett. 54 (1985) 2449.
[4] P.W. Brouwer, C.W.J. Beenakker, preprint cond-mat/9611162.
[5] P. Samuelson et al., in press;
A. Richter, Dissertation Thesis Universität Hamburg 2000 (ISBN 3-8265-9226-3).
[6] G.E. Blonder, M. Tinkham, T.M. Klapwijk, Phys. Rev. B 25 (1982) 4515.
[7] G.E. Blonder, M. Tinkham, Phys. Rev. B 27 (1983) 112.
[8] R. Rifkin, B.S. Deaver, Phys. Rev. B 13 (1976) 3894.
[9] E. Il'ichev et al., Rev. Sci. Instr. 72 (2001) 1882.
[10] A.A. Golubov, M.Yu. Kupriyanov, Physica C 259 (1996) 27.
[11] A.A. Golubov et al., Phys. Rev. B 51 (1995) 1073.
[12] E. Il'ichev et al., Appl. Phys. Lett. 76 (2000) 100.

## B.3. Paper B

M. Ebel, E. Il'ichev, M. Grajcar, C. Busch, and U. Merkt,
*Supercurrent-phase Relationship of the Nb/InAs(2DES)/Nb Josephson Junction*,
European Conference on Applied Superconductivity 2003 Proceedings,
Editors V. Ruggero and A. Barone,
IOP Conference series 181 (2004),
ISBN 0750309814

# Supercurrent-phase relationship of the Nb/InAs(2DES)/Nb Josephson junction

**M. Ebel†, E. Il'ichev‡, M. Grajcar‡, C. Busch†, and U. Merkt†**

† Universität Hamburg, Institut für Angewandte Physik und Zentrum für Mikrostrukturforschung, Jungiusstraße 11, D-20355 Hamburg, Germany
‡ Department of Cryoelectronics, Institute for Physical High Technology, P.O. Box 100239, D-07702 Jena, Germany

E-mail: ebel@physnet.uni-hamburg.de

**Abstract.**

Superconductor/normal conductor/superconductor (SNS) junctions with highly transparent interfaces are predicted to show significant deviations from harmonic supercurrent-phase relationships (CPR) at low temperatures. We investigate experimentally the CPR of two different Nb/InAs(2DES)/Nb Josephson junctions types in dependence of temperature from 20 mK to 9 K and gate voltage. The junctions are measured using a modified Rifkin-Deaver method by incorporating them into a superconducting loop, forming a single-junction interferometer that is coupled to a high quality tank circuit. The CPR is obtained from the measurement of the impedance of the phase-biased junction. Transport measurements complement the investigation. At low temperatures, substantial deviation of the CPR from conventional tunnel-junction behavior has been observed in accordance with Kulik-Omelyanchouk theory.

## 1. Introduction

The general expression for the supercurrent $I_S(\varphi)$ can be written as a Fourier series [1]:

$$I_S(\varphi) = I_C f(\varphi) = \sum_n I_n \sin(n\varphi)$$

For vanishing quasiparticle transmission probability through the junction (denoted in the following as transparency $D$), e.g. in the case of a tunnel junction, only $I_1$ is relevant, reducing this expression to the well-known Josephson equation $I_S(\varphi) = I_1 \sin\varphi = I_C \sin\varphi$ with the critical current $I_C$. In junctions with direct conductivity (weak links), higher order processes of charge transport lead to more complex behavior and a non-sinusoidal supercurrent-phase relationship (CPR) $f(\varphi)$. Kulik and Omelyanchouk have calculated the extreme case of a short ballistic junction, resulting in a CPR $f(\varphi)$ similar to a saw tooth. A review article can be found in [1].

Highly transparent weak links offer many exciting possibilities for basic research and applications. One example of this class is a tunable superconductor/normal conductor/superconductor (SNS) Josephson junction in the Nb/InAs(2DES)/Nb system, where the properties of the coupling two-dimensional electron system (2DES) can be influenced via a gate electrode. The exact conduction mechanism in this devices is still not fully understood.

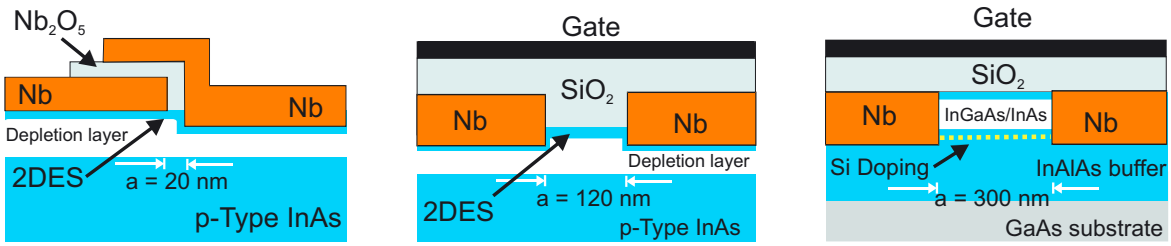


**Figure 1.** Cross sections of SNS Josephson junction types: overlapping junction on p-type InAs (a), JoFET on p-type InAs (b), and JoFET on InAs heterostructure (c).

However, as SNS junctions with highly transparent interfaces are predicted to show significant deviations from harmonic supercurrent-phase relationships at low temperatures and the CPR is fundamental in the theoretical description of Josephson junctions, direct experimental access to it could lead to further insights into their conduction mechanisms. Precise knowledge of deviations in the CPR is also important if one wants to use these junctions as sensors.

## 2. Sample Preparation

The superconductor used in building our SNS junctions is a Nb thin film, the normal conductor is the two-dimensional electron system (2DES) that forms in the naturally occurring inversion layer at the surface of p-type InAs. The InAs surface is cleaned in situ using low-energy Ar etching prior to the deposition of a Nb film by magnetron sputtering, yielding the highly transparent interfaces crucial for the junctions. The structures are patterned using standard optical and electron-beam lithography. We are using two sample geometries: in overlapping junction (figure 1(a)), we can set the electrode separation $a$ between 10 and 100 nm with nm accuracy by using anodic oxidation. Thus we can achieve short channel lengths, giving high transparency and large $I_C R_N$ products. The other geometry is known as Josephson field effect transistor (JoFET, figure 1(b)). In this case, the electrode separation is determined by lithography. Typical values are $a = 100 - 500$ nm.

The gate electrode of a JoFET gives us the opportunity to influence the electron density and Fermi velocity of the 2DES via field-effect. At a typical electron density of $n_s = 1.2 \cdot 10^{12}$ cm$^{-2}$ and mobility of $\mu \approx 10^4$ cm$^2$/Vs, the mean free path of 240 nm is longer than the channel length. From the dependence of the critical current on the channel length, we estimate the coherence length $\xi_N \approx 145$ nm at 1.8 K. Thus we have a quasi-ballistic superconducting weak link with the Josephson junction being in between the short and the long limit, where we can tune the junction from tunnel-like to quasi-ballistic behavior.

The use of the 2DES on p-type InAs is not without difficulties, as it forms on every surface of the crystal offering parallel conduction paths, resulting in significant bypass currents around the junction. In the future, we want to focus on a heterostructure substrate, where unwanted areas of the 2DES can be precisely removed by dry etching. First prototype JoFETs have been built on an InAs heterostructure (figure 1(c)), also known as high electron mobility transistor (HEMT). This alternative substrate promises additional advantages such as a 2DES of higher mobility besides the precise boundaries.

For preliminary transport measurements of the differential resistance and $I$-$V$-curves

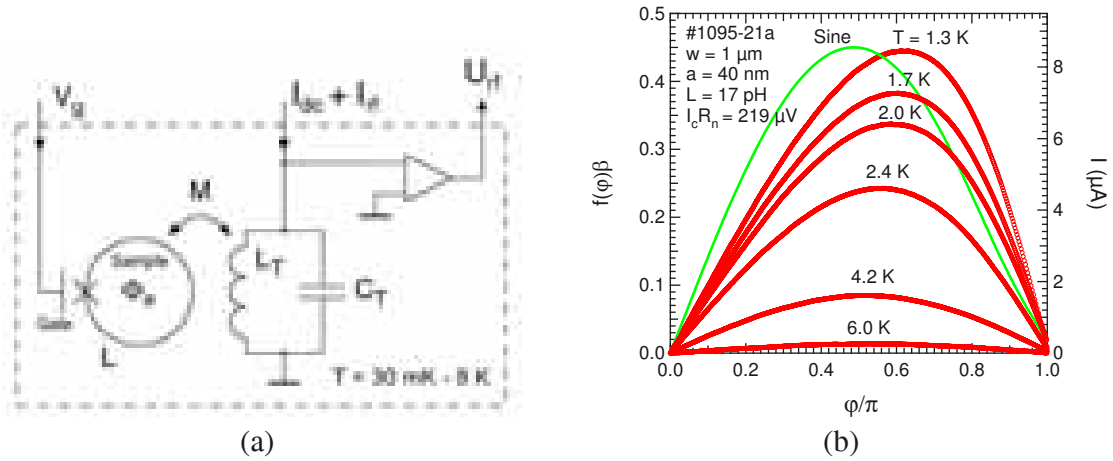


(a) (b)

**Figure 2.** (a) CPR measurement principle, (b) CPR (red) of a overlapping junction at temperatures between 1.3 K and 6.0 K. As a guide to the eye, a sine of comparable amplitude is drawn in green.

in dependence of temperature and magnetic field, the junction is fitted with electrodes for conventional four-point measurements. These experiments give us an independent method of determining the critical current and allow us to quantify the junction transparency. Afterwards, the now unnecessary leads are removed by dry etching and the junction is prepared for CPR measurement by shorting it with a superconducting loop, resulting in an RF-SQUID.

## 3. CPR Measurement Technique

The CPR of the Josephson junction is determined by an inductive method requiring no galvanic contacts to the sample, thus reducing noise. This technique is based on the work of Rifkin and Deaver [2]. The junction to be investigated is incorporated into a superconducting loop, and so is in equilibrium at all times. This loop forms an RF-SQUID, which is coupled inductively to a high quality tank circuit in resonance. The phase of the junction can be biased by external flux via a quasi-dc current $I_{dc}$. Changes in the impedance of the coupled system are measured and can be used to reconstruct the CPR. Figure 2(a) shows a sketch of the principle, further details are given in [3]. This method requires low critical currents of the junction and low inductances $L$ of the SQUID washer, as the SQUID gets hysteretic when $\beta = \frac{2\pi L I_C}{\Phi_0} > 1$, which prevents us from reconstructing the CPR. The challenge is to reduce these quantities while maintaining high interface transparencies and sufficient coupling to the tank circuit. We achieve this by reducing the geometric dimensions of the junction and the loop and by using complex washer designs, e.g. one with six SQUID washers connected in parallel and an integrated flux transformer, giving optimized inductance and coupling to the tank circuit.

## 4. Results

Optimized junctions for CPR measurements should have low critical current while maintaining excellent interface transparency and large $I_C R_N$ products. We achieve this by reducing the geometrical width $w$ of the junction. The results of transport measurements show

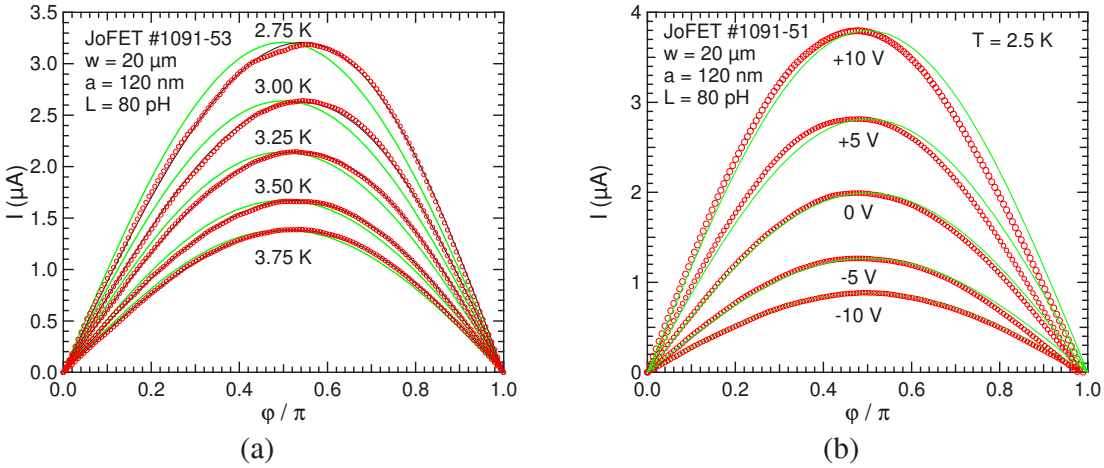


**Figure 3.** CPR of a JoFET in dependence of temperature (a) and gate voltage (b). A sine is drawn in green.

clearly developed subharmonic gap structures (SGS) in both junction types even at electrode widths reduced from $w = 50\,\mu\text{m}$ up to $1\,\mu\text{m}$. This indicates the high interface quality and transparency of the junctions.

Figure 2(b) shows the reconstructed current-phase relationship of a overlapping junction (width $w = 1\,\mu\text{m}$, electrode separation $a = 40\,\text{nm}$, transparency $D = 0.8$) at temperatures between 1.3 K and 6.0 K. For decreasing temperatures, gradual deviation of the CPR from conventional tunnel junction behavior towards Kulik-Omelyanchouk behavior is observed. At the same time, the critical current increases substantially, so that at some temperature the SQUID enters the hysteretic regime as $\beta = \frac{2\pi L I_C}{\Phi_0}$ approaches unity. In that case we are no longer able to reconstruct the CPR at lower temperatures. In this sample, the point was reached at 1.2 K, which is still well above our minimum temperature of 30 mK, so the values of inductance and critical current are still not optimal.

The reconstructed current-phase relationship of a JoFET (width $w = 20\,\mu\text{m}$, electrode separation $a = 120\,\text{nm}$, transparency $D = 0.35$) is shown in figure 3(a) at different temperatures between 2.75 K and 3.75 K. A gradual deviation from sinusoidal behavior with decreasing temperature is clearly seen along with the increasing critical current, corresponding to theoretical expectations. We have also determined the influence of an external gate voltage, pictured in figure 3(b). In spite of sacrificing the advantage of a measurement technique without galvanic leads by introducing a gate electrode, we were able to obtain the SQUID signal without a considerable deterioration. The critical current can be enhanced or reduced by gate voltage. However, no significant change of the CPR is visible. The small shift of the CPR maximum towards zero is caused by external noise introduced by the gate leads. Unfortunately, the gate electrode on the sample showing the deviations at low temperature was defective, so we had to use a different sample from the same wafer and processed in the same way. This sample did not show any significant deviations even without a gate contact.

The samples used for this experiment had relatively low transparencies of $D = 0.35$, so the deviations from a harmonic CPR are small. Measurements below 2.7 K were not possible as the SQUIDs switched into hysteretic regime. Further details are given in [4]. New samples with higher transparencies and optimized properties are in preparation.

## 5. Conclusion

We have successfully measured the current-phase relationship of two kinds of Nb/InAs(2DES)/Nb Josephson junctions in dependence of temperature and gate voltage. By controlling the electron density of the 2DES via gate voltage it is possible to change the critical current of the Josephson junction in a wide range without considerable deterioration of the RF-SQUID signal. At low temperatures, substantial deviation of the CPR from a conventional sinusoidal behavior towards a saw tooth form is observed. This is in qualitative agreement with predictions of Kulik-Omelyanchouk theory for highly transparent SNS junction. Transport measurements support the results gained by by phase sensitive measurements.

## Acknowledgments

We gratefully acknowledge financial support by the European Science Foundation via the PiShift program and by the Deutsche Forschungsgemeinschaft via the SFB 508 "Quantenmaterialien".

## References

[1] Likharev K K 1979 *Rev. Mod. Phys.* **51** 101
[2] Rifkin R and Deaver B S 1976 *Phys. Rev. B* **13** 3894
[3] Il'ichev E *et al.* 2001 *Rev. Sci. Instrum.* **72** 1882
[4] Grajcar M et al. 2002 *Physica C* **372-376** 27

## B.4. Paper C

M. Ebel, E. Il'ichev, M. Grajcar, T. Plecenik, C. Busch, and U. Merkt,
*Supercurrent-phase Relation of a Nb/InAs(2DEG)/Nb Josephson Junction in Overlapping Geometry*,
submitted to Phys. Rev. B, available at cond-mat/0407206

# Supercurrent-phase relationship of a Nb/InAs(2DES)/Nb Josephson junction in overlapping geometry

Mark Ebel,* Christian Busch,† and Ulrich Merkt
*Institut für Angewandte Physik und Zentrum für Mikrostrukturforschung, Universität Hamburg, Jungiusstr. 11, D-20355 Hamburg, Germany*

Miroslav Grajcar,‡ Tomáš Plecenik,‡ and Evgeni Il'ichev
*Department of Cryoelectronics, Institute for Physical High Technology, P.O. Box 100239, D-07702 Jena, Germany*

(Dated: August 27, 2004)

Superconductor/normal conductor/superconductor (SNS) Josephson junctions with highly transparent interfaces are predicted to show significant deviations from sinusoidal supercurrent-phase relationships (CPR) at low temperatures. We investigate experimentally the CPR of a ballistic Nb/InAs(2DES)/Nb junction in the temperature range from 1.3 K to 9 K using a modified Rifkin-Deaver method. The CPR is obtained from the inductance of the phase-biased junction. Transport measurements complement the investigation. At low temperatures, substantial deviations of the CPR from conventional tunnel-junction behavior have been observed. A theoretical model yielding good agreement to the data is presented.

PACS numbers: 74.45.+c, 74.50.+r

## I. INTRODUCTION

A fundamental item in the theoretical modeling of a Josephson junction is the dependency of the supercurrent $I_S$ flowing through it on the phase difference $\varphi$ across the junction. Golubov, Kupriyanov and Il'ichev published a recent review on the subject.[1] As this relation is necessarily $2\pi$-periodic and odd,[2] it can be expressed as the following Fourier series (with the critical current $I_C$):

$$I_S(\varphi) = I_C f(\varphi) = \sum_n I_n \sin(n\varphi). \tag{1}$$

$I_S(\varphi)$ is known as (super-)current-phase relationship or CPR, the dimensionless term $f(\varphi)$ as normalized CPR. For vanishing transparency (e.g. a tunnel junction), only $I_1$ is relevant, reducing Eq. 1 to the well-known dc Josephson[3] equation

$$I_S(\varphi) = I_1 \sin\varphi = I_C \sin\varphi. \tag{2}$$

Junctions with direct (i.e. non-tunnel) conductivity, such as the Nb/InAs(2DES)/Nb weak links used in this work, are predicted to show more complex behavior and a non-sinusoidal CPR due to higher order processes of charge transport such as multiple Andreev reflections.[1,2,4] Indications of a significant non-harmonic term in our junctions have been found in microwave measurements.[5,6] We are interested in experimental access to the CPR as a way to test and improve the theoretical models describing our junctions, since the conduction mechanisms in these devices are still not fully understood. The measurements deliver not only the dependency $f(\varphi)$, but also $I_C$, thus offering an independent comparison to transport measurements.

## II. THEORY

The first extensive theoretical works concerning high transparency superconducting weak links were published by Kulik and Omel'yanchuk for a short quasiclassical point contact in the dirty limit[7] $l \ll \xi_0$ (with mean free path $l$ and coherence length $\xi_0$) and for the clean limit[4] $l \gg \xi_0$, predicting a CPR $f(\varphi)$ changing from a sinusoidal curve to a saw tooth shape for high transparencies and low temperatures. These idealized model systems serve to understand the basic mechanisms leading to a deviation of the CPR from the well-known Josephson relation (Eq. 2), which we encounter also in complex real-world junctions, though mixed with secondary processes. Mechanically controlled break-junctions[8] come closest to the assumptions of the theory of Kulik and Omel'yanchuk. CPR measurements by a flux-detecting method in this system[9] agreed with the predicted changes in the position of the maximum and curve shape. In contrast to these systems, our SNS junctions exhibit a finite length, some scattering of electrons in the 2DES, and an area of induced superconductivity around the electrodes caused by the proximity effect. To take these properties into account and to describe the non-sinusoidal CPR in our experiments, we used the scattering matrix formalism[10] to derive a formula for the Josephson current through a double-barrier structure:[11]

$$\frac{eIR_0}{\pi k_B T_C} = \frac{16T}{T_C}\sum_{n=0}^{N-1}\sum_{m=0}^{\infty}\frac{-A^2|S_{12}|^2\sin(\varphi)}{1-2A^2(|S_{12}|^2\cos(\varphi)+|S_{11}|^2)+A^4|S_{11}^2+S_{12}^2|^2}, \tag{3}$$

where $R_0 = h/e^2$ is the resistance quantum, $A$ is the coefficient of the Andreev reflection at the InAs(2DEG)/InAs interface and $S_{ij}$ are the elements of the scattering matrix for normal reflection in a symmetric double barrier junction[12] $S_{11} = |r| + |r||t|^2p_n^2/(1+|r|^2p_n^2)$, $S_{12} = |t|^2p_n/(1+|r|^2p_n^2)$. Here $|r|^2, |t|^2$ are the reflection and transmission probabilities of the left and right-hand barrier, $p_n = \exp(ik_{Fn}a - \omega_m a/\hbar v_{Fn})$, where $\omega_m = (2m+1)\pi k_B T$ are Matsubara frequencies, $k_{Fn}$ and $v_{Fn}$ are components normal to the barriers of the wave vector and Fermi velocity, respectively, of the $n$-th transverse mode to the barriers and $a$ is the distance between them. Following the BTK approach,[13] the reflection and transmission coefficients can be written in the form

$$|t|^2 = 1 - |r|^2 = \frac{1-(n/N)^2}{(1-(n/N)^2)(\eta+1)^2/4\eta + Z^2} \tag{4}$$

where $Z$ is the dimensionless potential barrier strength and $\eta = v_{Fs}/v_{Fn}$ is the Fermi velocity mismatch.

In order to calculate the Josephson current from Eq. 3, one must determine the Andreev reflection coefficient $A$ for the InAs(2DEG)/InAs interface. Since superconductivity is induced in InAs by the proximity effect, the coefficient $A$ may be written as[14] $A = iF/(1+G)$, where $F$ and $G$ are Green functions in the inversion layer of InAs. Due to the low electron density of the inversion layer the suppression of the pair potential in Nb can be neglected and $F, G$ can be expressed by the McMillan equations[15] $G = \omega/\sqrt{\omega^2+\Phi^2}$, $F = \Phi/\sqrt{\omega^2+\Phi^2}$, and $\Phi = \tilde{\Delta}/(1+\gamma_B\sqrt{\tilde{\omega}^2+\tilde{\Delta}^2})$, where $\gamma_B$ is a dimensionless parameter characterizing the transparency between Nb and InAs, $\tilde{\Delta} = \Delta/\pi k_B T_C$, $\tilde{\omega} = \omega/\pi k_B T_C$, $\Delta$ is the superconducting energy gap of bulk Nb, and $T_C$ its critical temperature. Both the critical temperature and the energy gap of the Nb can be suppressed near the interface because of disorder[16] but $\tilde{\Delta} \approx 0.6$ remains constant.[17] Since $T_C$ can be determined from temperature measurement, there are only two free fitting parameters in the model, the carrier density $n_s$ and $\gamma_B$ (we assume $Z = 0$, i.e. no real barrier). The Fermi velocity $v_F$ and Fermi wave vector $k_F$ are calculated for a given value of $n_s$. Since the normal resistance depends on $n_s$ as well, the $n_s$ obtained from the fit can be verified comparing the theoretical and experimental value of the resistance.

## III. SAMPLE PREPARATION

The superconductor used in our SNS junctions is a Nb thin film, the normal conductor is the two-dimensional electron system (2DES) that forms as naturally occurring inversion layer at the surface of bulk p-type InAs. The InAs surface is cleaned in situ using low-energy Ar etching prior to the deposition of a 100 nm thick Nb film by magnetron sputtering, yielding the highly transparent interfaces required to observe deviations from sinusoidal CPR. The structures are patterned using standard optical and electron-beam lithography. We are using an overlapping sample geometry (see inset of Fig. 1), where we can set the electrode separation $a$ with nm accuracy using anodic oxidation to grow the insulating $Nb_2O_5$ interlayer. At a typical electron density of $n_s = 1.2\times10^{12}$ cm$^{-2}$ and mobility of $\mu \approx 10^4$ cm$^2$/Vs, the mean free path of $l = 240$ nm is much longer than the electrode separation $a = 40$ nm. From the dependence of the critical current on the channel length, we estimate the coherence length $\xi_N \approx 145$ nm at 1.8 K. Thus we have a ballistic ($a \ll l$) superconducting weak link in the short limit ($a \ll \xi_N$). More details have been published by Chrestin et al.[18]

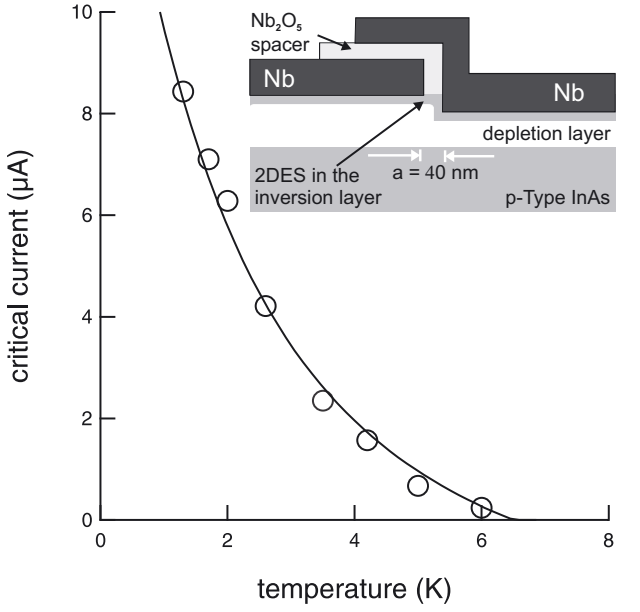


FIG. 1: Temperature dependence of the critical current. Circles are experimental data, the solid line presents a fit using the model described in the text. The inset shows a schematic cross section of the Josephson junction.

The use of the native 2DES on p-type InAs is not without difficulties, as it forms on every surface of the crystal. Thus it offers parallel conduction paths, resulting in significant bypass currents around the junction, which reduce the normal resistance $R_N$.

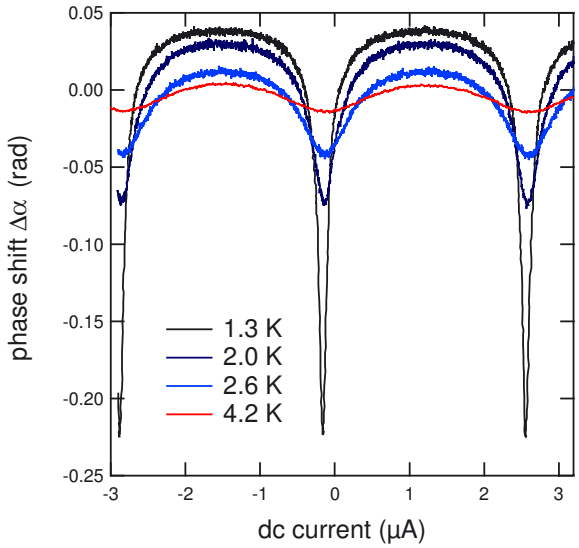


FIG. 2: Measured phase shift at various temperatures.

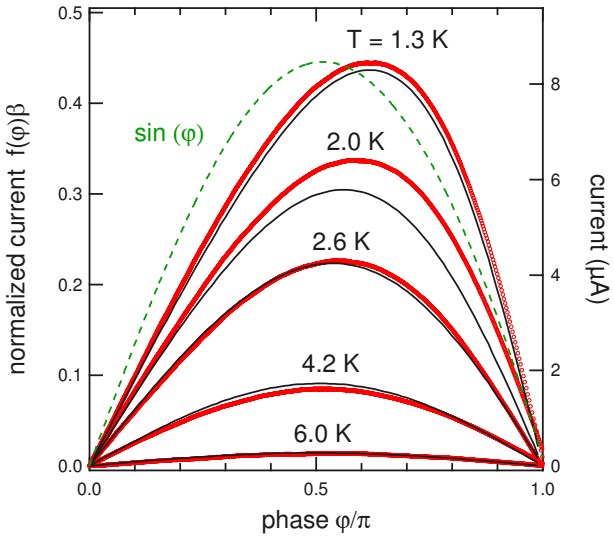


FIG. 3: CPR at temperatures between 1.3 K and 6.0 K, reconstructed from the data in Fig. 2. The solid lines are fits according to the model described in the text. For comparison, a pure sine curve is included.

## IV. CPR MEASUREMENT TECHNIQUE

The CPR of the Josephson junction is determined by an inductive rf frequency method requiring no galvanic contacts to the sample, thus reducing noise. This technique is based on the work of Rifkin and Deaver.[19] The junction to be investigated is incorporated into a superconducting loop. This loop forms an rf SQUID of inductance $L$, which is coupled inductively to a high quality tank circuit in resonance. The phase difference $\varphi$ across the junction can be biased by an external magnetic flux $\Phi_e$ via a dc current $I_{\rm dc}$. Changes in the impedance of the coupled system are measured and can be used to reconstruct the CPR. Further details are given in Ref. 1. This method requires low critical currents $I_C$ of the junction and low inductances $L$ of the SQUID washer, as the SQUID enters the hysteretic regime when $\beta f'(\varphi) > 1$, where $\beta = 2\pi L I_C/\Phi_0$ is the normalized critical current and $f'(\varphi) = df(\varphi)/d\varphi$. In the hysteretic mode the internal magnetic flux as a function of the external one becomes multivalued, preventing us to reconstruct the CPR in the complete phase range $(0, 2\pi)$. The challenge is to reduce $I_C$ and $L$ while maintaining excellent interface transparency, large $I_C R_N$ products, and sufficient coupling to the tank circuit. We achieve this by reducing the geometric dimensions of the junction and the loop and by complex washer designs. The presented junction is connected to six SQUID washers in parallel with an integrated flux transformer, for an inductance of $L = 17$ pH and optimized coupling to the tank circuit. A similar transformer is described and depicted in Ref. 1.

## V. RESULTS

The experiments are performed on an overlapping Josephson junction of width $w = 1$ $\mu$m and electrode separation $a = 40$ nm. Transport measurements at 1.8 K result in $I_C = 3.8$ $\mu$A, $R_N = 58$ $\Omega$, $I_C R_N = 220$ $\mu$V, and show clearly developed subharmonic gap structures (SGS) in the differential resistance of the junction. This indicates high interface quality and transparency of the junctions.

Figure 2 shows the recorded phase shift $\alpha$ in the tank circuit as a function of the applied quasi-dc current $I_{\rm dc}$ ramping the external flux $\Phi_e$ through the SQUID loop. This signal was averaged for 20 periods to reduce noise and then used to reconstruct the CPR depicted in Fig. 3. For decreasing temperatures, gradual deviation of the CPR from conventional sinusoidal behavior towards a sawtooth-shaped curve is observed. The position of maximum current is shifted to $0.63\pi$ at 1.3 K. At the same time, the critical current increases substantially, so that at some temperature the SQUID enters the hysteretic regime as $\beta f'(\varphi)$ approaches unity. In that case we are no longer able to reconstruct the CPR at lower temperatures.

The $I_C$-$T$ dependence was fitted by the model described above using the least squares method with two fitting parameters $n_s$ and $\gamma_B$. The other parameters used in the calculation were determined independently as critical temperature $T_C = 6.5$ K, width $w = 1.0$ $\mu$m, electrode separation $a = 40$ nm, interface parameter $Z = 0$, and Fermi velocity mismatch $\eta = 0.93$. The fitting procedure yields the parameters $n_s = 3.75 \times 10^{12}$ cm$^{-2}$ and $\gamma_B = 2.4$ and good agreement between theoretical and

experimental data (see Figs. 1 and 3). Note that the model fits the current-phase characteristic quite well for the parameters determined from the temperature dependence of the critical current. Only the curve taken at $T \approx 2.0$ K exhibits some deviation from the theoretical one. However, the temperature dependence of $I_C(T)$ is rather steep at low temperatures and a small difference between the temperature of the thermometer and the sample could be responsible. From the above parameters we calculate the junction resistance of $R_N = 83\ \Omega$. Transport measurements yield a slightly lower value of 58 Ω, but as we measure a parallel connection between substrate and junction, a higher junction resistance is to be expected. A realistic substrate resistance of 180 Ω produces the measured value of 58 Ω. The interface parameters indicate a highly transparent junction. The assumed carrier density is about three times the result $n_s = 1.2 \times 10^{12}$ cm$^{-2}$ from Shubnikov-de Haas measurements on comparable samples. Nevertheless, $n_s$ as determined from our model is consistent with the smaller experimental value of the junction resistance. A possible explanation for both effects is an effective widening of the contact due to the proximity effect in the surrounding 2DES.

## VI. CONCLUSION

We have successfully measured the current-phase relationship (CPR) of a Nb/InAs(2DES)/Nb Josephson junction in dependence of temperature. At low temperatures, substantial deviations of the CPR from a sinusoidal behavior towards a saw tooth shape are observed. This is in qualitative agreement with predictions of the Kulik-Omel'yanchuk theory for highly transparent SNS junctions and the measurements on Josephson field effect transistors presented in Ref. 11. A model yielding good quantitative agreement to the results is presented. Transport measurements support the results gained by phase sensitive measurements.


### Acknowledgments

We thank V. Zakosarenko for help with the washer design and gratefully acknowledge financial support by the European Science Foundation via the PiShift program and by the Deutsche Forschungsgemeinschaft via the SFB 508 Quantenmaterialien. M.G. wants to acknowledge partial support by Grant Nos. VEGA 1/9177/02 and APVT-20-021602.



* Electronic address: ebel@physik.uni-hamburg.de

† Now at Forschungszentrum Jülich, Institut für Plasmaphysik, D-52425 Jülich, Germany

‡ Also at Department of Solid State Physics, Comenius University, Mlynská Dolina F2, 842 48 Bratislava, Slovakia



[1] A.A. Golubov, M.Yu. Kupriyanov, and E. Il'ichev, Rev. Mod. Phys. **76**, 411 (2004).

[2] K. Likharev, Rev. Mod. Phys. **51**, 101 (1979).

[3] B. Josephson, Phys. Lett. **1**, 251 (1962).

[4] I. Kulik and A. Omel'yanchuk, Fizh. Nizk. Temp. **3**, 945 (1977), [Sov. J. Low Temp. Phys. 3, 459-461 (1977)].

[5] P. Baars, A. Richter, and U. Merkt, Phys. Rev. B **67**, 224501 (2003).

[6] P. Baars, A. Richter, and U. Merkt, Supercond. Sci. Technol. **16**, 1470 (2003).

[7] I. Kulik and A. Omel'yanchuk, Pis'ma Zh. Eksp. Teor. Fiz. **21**, 216 (1975), [JETP Lett. 21, 96-97 (1975)].

[8] C. Muller, J. van Ruitenbeek, and L. de Jongh, Physica C **191**, 485 (1992).

[9] M.C. Koops, G.V. van Duyneveldt, and R. de Bruyn Ouboter, Phys. Rev. Lett. **77**, 2542 (1996).

[10] P. Brouwer and C. Beenakker, Chaos, Solitons and Fractals **8**, 1249 (1997), cond-mat/9611162.

[11] M. Grajcar, M. Ebel, E. Il'ichev, R. Kürsten, T. Matsuyama, and U. Merkt, Physica C **372-376**, 27 (2002).

[12] M. Belogolovskii, M. Grajcar, P. Kúš, A. Plecenik, Š. Beňačka, and P. Seidel, Phys. Rev. B **59**, 9617 (1999).

[13] G.E. Blonder, M. Tinkham, and T.M. Klapwijk, Phys. Rev. B **25**, 4515 (1982).

[14] B.A. Aminov, A.A. Golubov, and M.Yu. Kupriyanov, Phys. Rev. B **53**, 365 (1996).

[15] A.A. Golubov, E.P. Houwman, J.G. Gijsbertsen, V.M. Krasnov, J. Flokstra, H. Rogalla, and M.Yu. Kupriyanov, Phys. Rev. B **51**, 1073 (1995).

[16] D. Belitz and T. Kirkpatrick, Rev. Mod. Phys. **66**, 261 (1994).

[17] R.A. Smith, M.Y. Reizer, and J.W. Wilkins, Phys. Rev. B **51**, 6470 (1995).

[18] A. Chrestin, T. Matsuyama, and U. Merkt, Phys. Rev. B **55**, 8457 (1997).

[19] R. Rifkin and B. Deaver, Phys. Rev. B **13**, 3894 (1976).

# C. Preparation Parameters

Standard preparation of Nb/InAs(2DES)/Nb junctions on bulk InAs:

| step | device/product | parameter | time |
|---|---|---|---|
| **wafer polishing** | | | |
| mechanical | Multipol 2 | 1 µm Alumina | 25 min |
| | cleaning | Tetrahydrofuran | 10 min |
| | cleaning | Isopropanol | 10 min |
| chemical | custom-built assembly | 0.0025% Bromine | 25 min |
| | | in Methanol | 25 min |
| | cleaning | Tetrahydrofuran | 10 min |
| | cleaning | Isopropanol | 10 min |
| **e-beam lithography** | | | |
| resist spin-coating | PMMA | spin-coating, 4000 rpm | 60 s |
| resist bake-out | oven | 160°C | 60 min |
| e-beam lithography | Zeiss DSM 962 | (see table below) | |
| development | Allresist AR 600-56 | | 105 s |
| stopping | Allresist AR 600-60 | | 30 s |
| barreling | Technics plasma 100-E | 180 W, $p_{O_2} = 1$ Torr | 60 s |
| **Nb sputtering** | | | |
| target cleaning | custom-built machine | 150 W, 280 V at 1 Pa | 5 min |
| sample cleaning | | 4 W, 180 V at 1 Pa | 8 min |
| Nb deposition | | 150 W, 280 V at 1 Pa | 120 s |
| lift-off | Allresist AR 300-70 | | >20 h |
| | ultrasonic bath | | 10 s |
| **photo-lithography** | | | |
| resist spin-coating | Shipley S1813 | spin-coating, 4000 rpm | 60 s |
| resist bake-out | hotplate | 100°C | 4 min |
| exposure | Suss mask aligner MJB3 | CI2, 50 mW/cm$^2$ | 6 s |
| development | Microposit MF319 | | 45 s |
| stopping | deionized water | | 15 s |
| barreling | Technics plasma 100-E | 180 W, $p_{O_2} = 1$ Torr | 60 s |

Electron-beam lithography parameters:

| parameter | value |
|---|---|
| **e-beam lithography** | |
| lens aperture | 4 |
| heating current | 3.74 A |
| voltage | 30 kV |
| emission current | 10-15 µA |
| sample current | 10-15 pA |
| spot size | M13 |
| working distance | 6 mm |
| write field | $100^2$ µm$^2$ |
| magnification | 725 |
| step size | 1 pixel |
| resist sensitivity | 130 µC/cm$^2$ |

Gate preparation for JoFETs:

| step | device/product | parameter | time |
|---|---|---|---|
| **insulation layer** | | | |
| oxide PECVD | Oxford Plasmalab 80+ | 150°C, 1 Torr, 20 W, 450 sccm $SiH_4/N_2$ + 710 sccm $N_2O$, | |
| via patterning | photo-lithography | standard parameters | |
| oxide removal in vias | hydroflouric acid HF | | 15 s |
| **gate preparation** | | | |
| gate structuring | photo-lithography | standard parameters | |
| thermal evaporation | Balzers-Pfeiffer PLS500 | 10 nm Al, 40 nm Au | |
| lift-off | Allresist AR 300-70 | | >20 h |
| | ultrasonic bath | | 10 s |

HEMT RIE etching:

| step | device/product | parameter | time |
|---|---|---|---|
| patterning | standard lithography | standard parameters | |
| RIE etching | Oxford Plasmalab 80+ | 100 W, 4 mTorr 10 sccm $SiCl_4$ + 10 sccm Ar | 100 s |

Anodic oxidation for overlapping contacts:

| step | device/product/parameter |
|---|---|
| **anodic oxidation** | |
| patterning | standard lithography |
| electrolyte | 26 g ammonium pentaborate, 187 ml ethylene glycol, 127 ml $H_2O$ |
| anodic oxidation | $I_{\text{oxidation}} = 0.5$ mA, $V_{\text{oxidation}} = 20.5$ V (for 40 nm) |
| InAs oxide removal | $H_2SO_4$ (50%) for 2 min |

Negative photo-lithography for Nb dry etching:

| step | device/product | parameter | time |
|---|---|---|---|
| **negative lithography** | | | |
| resist spin-coating | Microresist ma-N 1410 | 5000 rpm, ramp 255 | 30 s |
| resist bake-out | oven | 95°C | 90 s |
| exposure | Suss mask aligner MJB3 | CI1, 40 mW/cm$^2$ | 12 s |
| development | Microresist ma-D 533s | | 45 s |
| Nb etching | Oxford Plasmalab 80+ | 25 W, 0.1 mTorr, 20 sccm $SF_6$ | 5 min |

# D. Glossary

| Abbreviation | Explanation |
|---|---|
| 2DES | two-dimensional electron system |
| ac | alternating current |
| AFM | atomic force microscope |
| Al | aluminum |
| Ar | argon |
| Au | gold |
| BCS | theory of Bardeen, Cooper, and Schrieffer (1957) |
| BTK | theory of Blonder, Tinkham, and Klapwijk (1982) |
| CPR | current-phase relationship |
| dc | direct current |
| He | helium |
| HEMT | high electron mobility transistor |
| hf | high frequency |
| In | indium |
| InAs | indium arsenide |
| IPHT | institute of physical high technology in Jena |
| JoFET | Josephson field-effect transistor |
| N | normal conductor |
| Nb | niobium |
| OTBK | theory of Octavio, Tinkham, Blonder, and Klapwijk (1983) |
| PECVD | plasma-enhanced chemical-vapor deposition |
| PMMA | polymethylmethacrylate |
| rf | radio frequency |
| RIE | reactive ion etching |
| S | superconductor |
| SEM | scanning electron microscope |
| SNS | superconductor/normal conductor/superconductor |

| Variable | Explanation |
|---|---|
| $a$ | electrode separation |
| $B$ | applied magnetic field |
| $\Delta$ | energy gap, for Nb $2\Delta(0\,\mathrm{K}) = 3.05\,\mathrm{eV}$ |
| $\Delta_N$ | induced energy gap |
| $D$ | junction transparency |
| $e$ | elementary charge, $e = 1.602 \times 10^{-19}\,\mathrm{C}$ |
| $h$ | Planck's constant, $h = 6.626 \times 10^{-34}\,\mathrm{Js}$ |
| $I$ | current |
| $I_C$ | critical current |
| $I_{\mathrm{Ex}}$ | excess current |
| $I_C R_N$ | characteristic voltage |
| $I_{\mathrm{mod}}$ | modulation current |
| $l$ | mean free path |
| $\Phi$ | magnetic flux |
| $\Phi_0$ | magnetic flux quantum, $\Phi_0 = \frac{h}{2e} = 2.068 \times 10^{-15}\,\mathrm{Wb}$ |
| $R$ | resistance |
| $R_N$ | normal resistance |
| $R(T)$ | temperature dependent resistance |
| $T$ | temperature |
| $T_C$ | critical (or transition) temperature |
| $V$ | voltage |
| $V_G$ | gate voltage |
| $w$ | electrode width |

# Bibliography


S. Adolph. *Hochfrequenzcharakterisierung von Nb/InAs(2DEG)/Nb Kontakten*. Diploma thesis, Universität Hamburg (1998).

S. Albrecht. *Präparation von supraleitenden Quantenpunktkontakten auf InAs-Heterostrukturen*. Diploma thesis, Universität Hamburg (2003).

B. A. Aminov, A. A. Golubov, and M. Y. Kupriyanov. *Quasiparticle current in ballistic constrictions with finite transparencies of interfaces*. Phys. Rev. B, **53**(1), 365–373 (1996).

P. W. Anderson and J. M. Rowell. *Probable Observation of the Josephson Superconducting Tunneling Effect*. Phys. Rev. Lett., **10**, 230–232 (1963).

A. F. Andreev. *The Thermal Conductivity of the Intermediate State in Superconductors*. Sov. Phys. JETP, **19**(5), 1228–1231 (1964).

Angstrom Sciences. *Personal communication with Rob M. Belan* (2003).

P. Baars. *Josephson Effekte in Nb/InAs(2DEG)/Nb Kontakten auf p-Typ InAs*. Diploma thesis, Universität Hamburg (2000).

P. Baars. *Transport and Microwave Properties of Nanostructured InAs/Nb Hybrid Devices*. Dissertation, Universität Hamburg, Cuvillier Verlag, Göttingen (2004).

P. Baars, A. Richter, and U. Merkt. *Temperature and power dependence of Shapiro and Fiske step widths in Nb/InAs/Nb Josephson junctions*. Phys. Rev. B, **67**, 224501 (2003).

P. F. Bagwell. *Special Issue: Mesocopic Superconductivity*. Superl. and Microstr., **25**(5/6), 627–1288 (1999).

J. Bardeen, L. N. Cooper, and J. R. Schrieffer. *Theory of Superconductivity*. Phys. Rev., **108**, 1175ff (1957).

G. Bastian. *Comment on "Critical currents in ballistic two-dimensional InAs-based superconducting weak links"*. Phys. Rev. B, **62**(14), 9840–9841 (2000).

G. Bastian, E. O. Göbel, A. B. Zorin, H. Schulze, J. Niemeyer, T. Weimann, M. R. Bennett, and K. E. Singer. *Quasiparticle Interference Effects in a Ballistic Superconductor-Semiconductor-Superconductor Josephson Junction*. Phys. Rev. Lett., **81**(8), 1686–1689 (1998).

D. Belitz and T. R. Kirkpatrick. *The Anderson-Mott transition*. Rev. Mod. Phys., **66**, 261–380 (1994).

M. Belogolovskii, M. Grajcar, P. Kúš, A. Plecenik, Š. Beňačka, and P. Seidel. *Phase-coherent charge transport in superconducting heterocontacts*. Phys. Rev. B, **59**, 9617–9626 (1999).

G. E. Blonder, M. Tinkham, and T. M. Klapwijk. *Transition from metallic to tunneling regimes in superconducting microconstrictions: Excess current, charge imbalance, and supercurrent conversion*. Phys. Rev. B, **25**(7), 4515–4532 (1982).

E. N. Bratus, V. S. Shumeiko, and G. Wendin. *Theory of Subharmonic Gap Structure in Superconducting Mesoscopic Tunnel Contacts*. Phys. Rev. Lett., **74**(11), 2110–2113 (1995).

P. W. Brouwer and C. W. J. Beenakker. *Anomalous temperature dependence of the supercurrent through a chaotic Josephson junction*. Chaos, Solitons and Fractals, **8**, 1249 (1997). Cond-mat/9611162.

C. Busch. *Entwicklung von Nb/InAs(2DEG)/Nb Josephson-Kontakten in Überlapp-Geometrie zur Messung der Strom-Phasen-Beziehung*. Diploma thesis, Universität Hamburg (2002).

A. Chrestin. *Transport properties of mesoscopic Nb/p-type InAs/Nb weak links*. Dissertation, Universität Hamburg, Shaker-Verlag, Aachen (1996).

A. Chrestin, T. Matsuyama, and U. Merkt. *Evidence for a proximity-induced energy gap in Nb/InAs/Nb junctions*. Phys. Rev. B, **55**, 8457–8465 (1997).

A. Chrestin and U. Merkt. *High $I_cR_n$ products in Nb/p-type InAs/Nb Josephson junctions*. Appl. Phys. Lett., **70**, 3149ff. (1997).

P. G. de Gennes. *Boundary Effects in Superconductors*. Rev. Mod. Phys., **36**, 225–237 (1964).

M. Ebel. *Optimierung von Niob-Schichten für Supraleiter/Normalleiter/Supraleiter (SNS)-Kontakte*. Diploma thesis, Universität Hamburg (2000).

M. Ebel, E. Il'ichev, M. Grajcar, T. Plecenik, C. Busch, and U. Merkt. *Supercurrent-phase Relation of a Nb/InAs(2DEG)/Nb Josephson Junction in Overlapping Geometry*. cond-mat/0407206 (2004). Submitted to Phys. Rev. B.

T. Economist. *Quantum Dreams*. The Economist, **358**(8212), 83–84 (2001). Mar 10th.

M. D. Fiske. *Temperature and Magnetic Field Dependences of the Josephson Tunneling Current*. Rev. Mod. Phys., **36**, 221–222 (1964).

K. Flensberg, J. B. Hansen, and M. Octavio. *Subharmonic energy-gap structure in superconducting weak links*. Phys. Rev. B, **38**(13), 8707–8711 (1988).

Gmelin. *Handbuch der Anorganischen Chemie, Niob Teil A*. Verlag Chemie, Weinheim (1969).

A. A. Golubov, E. P. Houwman, J. G. Gijsbertsen, V. M. Krasnov, J. Flokstra, H. Rogalla, and M. Y. Kupriyanov. *Proximity effect in superconductor-insulator-superconductor Josephson tunnel junctions: Theory and experiment*. Phys. Rev. B, **51**, 1073–1089 (1995).

A. A. Golubov, M. Y. Kupriyanov, and E. Il'ichev. *The current-phase relation in Josephson junctions*. Rev. Mod. Phys., **76**, 411–469 (2004).

M. Götz, V. V. Khanin, H. Schulze, A. B. Zorin, J. Niemeyer, E. Il'ichev, A. Chwala, H. E. Hoenig, and H.-G. Meyer. *Harmonic current-phase relation in Nb–Al-based superconductor/insulator/normal conductor/insulator/superconductor-type Josephson junctions between 4.2 K and the critical temperature*. Appl. Phys. Lett., **77**(9), 1354–1356 (2000).

M. Grajcar, M. Ebel, E. Il'ichev, R. Kürsten, T. Matsuyama, and U. Merkt. *Supercurrent-phase relation of a Nb/InAs(2DEG)/Nb Josephson junction*. Physica C, **372-376**, 27–30 (2002).

V. N. Gubankov, V. P. Koshelets, and G. A. Ovsyannikov. *Coherent effects in superconducting bridges of variable thickness*. Sov. Phys. JETP, **44**, 181–186 (1976).

W. Haberkorn, H. Knauer, and J. Richter. Phys. stat. sol., **A 47**, K161 (1978).

J. P. Heida, B. J. van Wees, T. M. Klapwijk, and G. Borghs. *Critical currents in ballistic two-dimensional InAs-based superconducting weak links*. Phys. Rev. B, **60**(18), 13135–13138 (1999).

E. Il'ichev, N. Oukhanski, A. Izmalkov, T. Wagner, M. Grajcar, H.-G. Meyer, A. Y. Smirnov, A. M. van den Brink, M. H. S. Amin, and A. M. Zagoskin. *Continuous Monitoring of Rabi Oscillations in a Josephson Flux Qubit*. Phys. Rev. Lett., **91**, 097906 (2003).

E. Il'ichev, A. Y. Smirnov, M. Grajcar, A. Izmalkov, D. Born, N. Oukhanski, T. Wagner, W. Krech, H.-G. Meyer, and A. M. Zagoskin. *Radio-Frequency Method for Investigation of Quantum Properties of Superconducting Structures*. cond-mat/0402559 (2004). Submitted to Fizika Nizkikh Temperatur (Low Temperature Physics).

E. Il'ichev, V. Zakosarenko, L. Fritzsch, R. Stolz, H. E. Hoenig, H.-G. Meyer, M. Götz, A. B. Zorin, V. V. Khanin, A. B. Pavolotsky, and J. Niemeyer. *Radio-frequency based monitoring of small supercurrents*. Rev. Sci. Instrum., **72**(3), 1882–1887 (2001).

E. Il'ichev, V. Zakosarenko, V. Schultze, H. E. Hoenig, H.-G. Meyer, V. N. Glyatsev, and A. Golubov. *Temperature dependence of the current-phase relation for* $YBa_2Cu_3O_{7-x}$ *step-edge Josephson junctions*. Appl. Phys. Lett., **72**(6), 731–733 (1998).

Z. Ivanov. Fizh. Nizk. Temp., **7**, 560 (1981). [Sov. J. Low Temp. Phys. 7, 275 (1981)].

L. D. Jackel, R. A. Buhrman, and W. W. Webb. *Direct measurement of current-phase relations in superconducting weak links*. Phys. Rev. B, **10**(7), 2782–2785 (1974).

B. D. Josephson. *Possible New Effects in Superconducting Tunneling*. Phys. Lett., **1**(7), 251 (1962).

M. B. Ketchen, W. J. Gallagher, A. W. Kleinsasser, S. Murphy, and J. R. Clem. In H. Hahlbohm and H. Lubbig (editors), *SQUID'85 Superconducting Quantum Interference Devices and their Applications*, page 865. de Gruyter, Berlin (1985).

R. W. Keyes. *Quantum computing with solids*. Physics World (2002).

M. C. Koops, G. V. van Duyneveldt, and R. de Bruyn Ouboter. *Direct Observation of the Current-Phase Relation of an Adjustable Superconducting Point Contact*. Phys. Rev. Lett., **77**(12), 2542–2545 (1996).

I. O. Kulik and A. N. Omel'yanchuk. *Contribution to the microscopic theory of the Josephson effect in superconducting bridges*. Pis'ma Zh. Eksp. Teor. Fiz., **21**(4), 216–219 (1975). [JETP Lett. 21, 96-97 (1975)].

I. O. Kulik and A. N. Omel'yanchuk. *Properties of superconducting microbridges in the pure limit*. Fizh. Nizk. Temp., **3**, 945–948 (1977). [Sov. J. Low Temp. Phys. 3, 459-461 (1977)].

J. Kurkijärvi. *Intrinsic Fluctuations in a Superconducting Ring Closed with a Josephson Junction*. Phys. Rev. B, **6**(3), 832–835 (1972).

K. Kuroda and M. Yoda. *Niobium-stress influence on Nb/Al-oxide/Nb Josephson junctions*. J. Appl. Phys., **63**(7), 2352–2357 (1987).

R. Kürsten. *Josephson-Feldeffektransistoren auf p-Typ InAs*. Dissertation, Universität Hamburg, Cuvillier Verlag, Göttingen (2002).

Y. Makhlin, G. Schön, and A. Shnirman. *Josephson-junction qubits with controlled couplings*. Nature, **398**, 305–307 (1999).

Y. Makhlin, G. Schön, and A. Shnirman. *Quantum state engineering with Josephson-junction devices*. Rev. Mod. Phys., **73**, 357–400 (2001).

T. Matsuyama. *Präparation und Charakterisierung von Nb/InAs(2DEG)/Nb Kontakten*. Dissertation, Universität Hamburg, Shaker-Verlag, Aachen (1994).

T. May. *Optimierung sekundärer Temperaturnormale mit statistischer Versuchsplanung*. Diploma thesis, Friedrich-Schiller-Universität Jena (1998).

T. May, E. Il'ichev, H.-G. Meyer, and M. Grajcar. *Microfabricated oscillator for radio-frequency microscopy with integrated magnetic field concentrator*. Rev. Sci. Instrum., **74**(3), 1282–1284 (2003).

C. A. Mead and W. G. Spitzer. *Fermi Level Position at Metal-Semiconductor Interfaces*. Phys. Rev., **134**(3A), A713–A716 (1964).

C. Meißner. *Einfluß von Gateoxiden auf den elektrischen Transport und der Rashba-Effekt in 2DEG InAs*. Diploma thesis, Universität Hamburg (1998).

J. Milde. *Spinpolarisierter Transport in quasi-zweidimensionalen Elektronensystemen in InAs*. Diploma thesis, Universität Hamburg (2000).

C. J. Muller, J. M. van Ruitenbeek, and L. J. de Jongh. *Experimental observation of the transition from weak link to tunnel junction*. Physica C, **191**, 485–504 (1992).

M. Octavio, M. Tinkham, G. E. Blonder, and T. M. Klapwijk. *Subharmonic energy-gap structure in superconducting constrictions*. Phys. Rev. B, **27**(11), 6739–6746 (1983).

H. K. Onnes. Commun. Phys. Lab., **12**, 120 (1911).

N. Oukhanski, M. Grajcar, E. Il'ichev, and H.-G. Meyer. *Low noise, low power consumption high electron mobility transistors amplifier, for temperatures below 1K*. Rev. Sci. Instrum., **74**(2), 1145–1146 (2003).

C. Pels. *Ferromagnetic electrodes for spin-polarized transport*. Dissertation, Universität Hamburg, Cuvillier Verlag, Göttingen (2003).

A. Richter. *Electronic Transport in Nb/InAs-HEMT Superconductor/Semiconductor Hybrid Devices*. Dissertation, Universität Hamburg, Shaker-Verlag, Aachen (2001).

A. Richter, P. Baars, and U. Merkt. *Supercurrents in two-dimensional electron systems*. Physica E, **12**, 911–917 (2002).

R. Rifkin and B. S. Deaver. *Current-phase relation and phase-dependent conductance of superconducting point contacts from rf impedance measurements*. Phys. Rev. B, **13**(9), 3894–3896 (1976).

S. M. Rossnagel. *Handbook of Vacuum Science and Technology*, chapter Sputtering, page 609. Academic Press (1998). ISBN 0-12-352065-7.

P. Samuelsson, A. Ingerman, G. Johansson, E. V. Bezuglyi, V. S. Shumeiko, G. Wendin, R. Kürsten, A. Richter, T. Matsuyama, and U. Merkt. *Coherent current transport in wide ballistic Josephson junctions*. cond-mat/0311344 (2003). Submitted to Phys. Rev. B.

T. Schäpers, A. Kaluza, K. Neurohr, J. Malindretos, G. Crecelius, A. van der Hart, H. Hardtdegen, and H. Lüth. *Josephson effect in Nb/two-dimensional electron gas structures using a pseudomorphic InGaAs/InP heterostructure*. Appl. Phys. Lett., **71**, 3575–3577 (1997).

R. Scharnweber. *Metall-Oxid-Halbleiter (MOS)-Strukturen auf InAs mit anodischem Oxid*. Diploma thesis, Universität Hamburg (1993).

E. Scheer, P. Joyez, D. Esteve, C. Urbina, and M. H. Devoret. *Conduction Channel Transmissions of Atomic-Size Aluminum Contacts*. Phys. Rev. Lett., **78**, 3535–3538 (1997).

Y. V. Sharvin. *A Possible Method for Studying Fermi Surfaces*. Sov. Phys. JETP, **48**, 984–985 (1963).

A. H. Silver and J. E. Zimmerman. *Quantum States and Transitions in Weakly Connected Superconducting Rings*. Phys. Rev., **157**(2), 317–341 (1967).

R. A. Smith, M. Y. Reizer, and J. W. Wilkins. *Suppression of the order parameter in homogeneous disordered superconductors*. Phys. Rev. B, **51**, 6470–6492 (1995).

W. C. Stewart. *Current-Voltage Characteristics of Josephson Junctions*. Appl. Phys. Lett., **12**(8), 277–280 (1968).

M. J. Storcz and F. K. Wilhelm. *Design of realistic switches for coupling superconducting solid-state qubits*. Appl. Phys. Lett., **83**, 2389 (2003).

C. Sürgers, C. Strunk, and H. von Löhneysen. *Effect of substrate temperature on the microstructure of thin niobium fims*. Thin Solid Films, **239**, 51–56 (1994).

H. Takayanagi, T. Akazaki, and J. Nitta. *Interference effect on the critical current in a clean-limit superconductor-normal metal-superconductor junction*. Phys. Rev. B, **51**(2), 1374–1377 (1995).

H. Takayanagi and T. Kawakami. *Superconducting Proximity Effect in the Native Inversion Layer on InAs*. Phys. Rev. Lett., **54**(22), 2449–2452 (1985).

S. A. Wolf, J. J. Kennedy, and M. Nisenoff. *Properties of superconducting rf sputtered ultrathin films of Nb*. J. Vac. Sci. Technol., **13**(1), 145–147 (1975).

# E. Acknowledgments

This work would not have been possible without the assistance and support of many people. I wish to thank

- Prof. Dr. Ulrich Merkt, who gave me the opportunity to do this work and supported me in all critical areas
- Dr. Evgeni Il'ichev and Dr. Miroslav Grajcar for the successful and very pleasant collaboration and their hospitality in Jena, as well as Torsten May and all the other people in Jena who supported this project
- the European Science Foundation ESF and the Deutsche Forschungsgemeinschaft DFG for financial support

I thank the people of the Group N for the excellent atmosphere and lots of helpful discussions and practical assistance, especially:

- Peter Baars for a great time in our office and on conferences, help with computer issues and all other matters
- Marcus Steiner for diligent proof reading
- Christian Pels for help and discussions of all sputter-related troubles
- Toru Matsuyama for helping when no one else can
- Reinhard Kürsten and Andreas Richter for teaching me a lot
- Christian Busch for good cooperation during his diploma thesis
- Alexander van Staa for assistance in MFM measurements
- Sebastian von Oehsen for managing the EM game
- Jurik Gancarz for his magic hands and fantastic mechanical constructions
- Malte Kurfiß for help in vacuum emergencies
- Thomas Finger, Klaus Ahrens, and the people of the electronic and mechanical workshops for keeping the critical equipment running most of the time

- Petra Roth, Heidrun Dold, and Barbara Truppe for effective handling of administrative matters

Last but not least, I wish to thank my family for the most important support of all!